



# A comprehensive approach for fatigue analysis of shape memory alloys

Claire Morin

## ► To cite this version:

Claire Morin. A comprehensive approach for fatigue analysis of shape memory alloys. Materials and structures in mechanics [physics.class-ph]. Ecole Polytechnique X, 2011. English. NNT : . pastel-00608205

**HAL Id: pastel-00608205**

**<https://pastel.hal.science/pastel-00608205>**

Submitted on 12 Jul 2011

**HAL** is a multi-disciplinary open access archive for the deposit and dissemination of scientific research documents, whether they are published or not. The documents may come from teaching and research institutions in France or abroad, or from public or private research centers.

L'archive ouverte pluridisciplinaire **HAL**, est destinée au dépôt et à la diffusion de documents scientifiques de niveau recherche, publiés ou non, émanant des établissements d'enseignement et de recherche français ou étrangers, des laboratoires publics ou privés.



THÈSE

présentée pour l'obtention du titre de

DOCTEUR DE L'ÉCOLE POLYTECHNIQUE

Spécialité : Mécanique

par

Claire Morin

Sujet de thèse :

# A COMPREHENSIVE APPROACH FOR FATIGUE ANALYSIS OF SHAPE MEMORY ALLOYS

Soutenue le 23 mai 2011 devant le jury composé de

Président :	M. Jean-Baptiste LEBLOND
Rapporteurs :	M. André CHRYSOCHOOS M. Qing-Ping SUN
Examineurs :	M. Günay ANLAS M. Habibou MAITOURNAM M. Etienne PATOOR
Co-directeur :	M. Wael ZAKI
Directeur :	M. Ziad MOUMNI



ENSTA-Paristech  
Unité de Mécanique  
Groupe Matériaux et Structures

Claire Morin: *A comprehensive approach for fatigue analysis of Shape Memory Alloys* , PhD thesis.

A mes parents,  
à Bénédicte, Mathilde et Jean-Philippe,  
et à ma filleule Bertille.

## RÉSUMÉ

Nous développons, en trois étapes, une approche globale de calcul à la fatigue des Alliages à Mémoire de Forme. La détermination de la loi de comportement permet le calcul de l'état thermomécanique stabilisé de la structure. Afin d'obtenir une meilleure prédiction de cette réponse, la dissymétrie entre traction et compression et le couplage fort thermomécanique sont ajoutés aux modèles ZM. Ensuite, le calcul numérique de l'état stabilisé est réalisé grâce à une généralisation de la Méthode Cyclique Directe, permettant un gain de temps de calcul considérable par rapport à la méthode incrémentale. Enfin, la durée de vie en fatigue est déterminée par un critère de fatigue énergétique qui tient compte de l'effet de la pression hydrostatique. La dépendance de la durée de vie vis-à-vis de la température et de la fréquence de chargement est discutée. Les perspectives concernent la validation des lois de comportement et du critère de fatigue pour des chargements non proportionnels.

**MOTS-CLÉS :** Matériaux à Mémoire de Forme, Dissymétrie, Couplage thermomécanique, Méthode Cyclique Directe, Dissipation, Fatigue.

## ABSTRACT

We develop a comprehensive approach for fatigue analysis of SMAs in three steps: first, the determination of the constitutive law allows the computation of the stabilized thermomechanical state of the structure. In order to better predict this state, tensile-compressive asymmetry and strong thermomechanical coupling are introduced into the ZM models. Second, the stabilized state is computed using an extension of the Direct Cyclic Method, which is shown to provide significant saving in computation time compared to the conventional incremental method. Third, the fatigue lifetime of the structure is determined with an energy-based criterion accounting for the influence of the hydrostatic pressure. The dependence of the fatigue lifetime on temperature and loading frequency is discussed. The prospects of this work include the validation of the constitutive laws and fatigue criterion for the case of non proportional loadings.

**KEYWORDS:** Shape Memory Alloys, Tensile-compressive asymmetry, Thermomechanical coupling, Direct Cyclic Method, Dissipation, Fatigue.

## PUBLICATIONS

The publications associated with this PhD work are:

- About tensile-compressive asymmetry, developed in chapter 3:

W. Zaki, Z. Moumni and **C. Morin**. Modeling tensile-compressive asymmetry for superelastic shape memory alloys. *Mechanics of Advanced Materials and Structures*. Accepted in 2010.

- About thermomechanical coupling, developed in chapter 4:

**C. Morin**, Z. Moumni, W. Zaki, 2011. A phenomenological model for shape memory alloys accounting for thermomechanical coupling. *International Journal of Plasticity*, 27 (5), 748-767. doi:10.1016/j.ijplas.2010.09.005

**C. Morin**, Z. Moumni, W. Zaki, 2011. Influence of heat transfer on the thermomechanical behavior of Shape Memory Alloys. *International Review of Mechanical Engineering*, 5 (2), 329-339.

**C. Morin**, Z. Moumni, W. Zaki. Thermomechanical coupling in Shape Memory Alloys under cyclic loadings: experimental analysis and constitutive modelling. *International Journal of Plasticity*. Accepted in 2011. doi:10.1016/j.ijplas.2011.05.005.

W. Zaki, **C. Morin**, Z. Moumni, 2011. A simple 1D model with thermomechanical coupling for shape memory alloys. *Materials Science and Engineering*. 10 012149.

W. Zaki, **C. Morin**, Z. Moumni, 2010. A model for shape memory alloys accounting for thermomechanical coupling. *Proceedings of WCCM/APCOM 2010*, Sydney, Australia.

**C. Morin**, Z. Moumni, W. Zaki, 2010. Thermo-mechanical coupling in shape Memory Alloys. *Proceedings of Euromech 505*, Paris, France.

- About Direct Cyclic Method, detailed in chapter 5:

**C. Morin**, Z. Moumni, W. Zaki, 2011. Direct numerical determination of the asymptotic cyclic behavior of pseudoelastic shape memory structures. *Journal of Engineering Mechanics*, 137 (7), 497-504. doi:10.1061/(ASCE)EM.1943-7889.0000249.

- About Fatigue analysis, topic of chapter 6:

**C. Morin**, Z. Moumni, W. Zaki, 2010. Cyclic behavior and fatigue design of shape memory alloy devices. *Proceedings of Plasticity 2010*, St. Kitts, St Kitts and Nevis.

# ACKNOWLEDGMENT

A Monsieur Ziad MOUMNI.

Il m'a proposé cette thèse et m'a soutenue dans sa mise en oeuvre tout au long de ces trois années. Il a toujours su me donner des orientations de recherche, tout en me laissant une grande autonomie au quotidien.

A Monsieur Wael ZAKI.

Il a activement participé à l'encadrement de ce travail, malgré la distance. Ses nombreux conseils et corrections m'ont été très précieux.

*Qu'ils veuillent bien croire à ma sincère gratitude.*

A Monsieur Antoine CHAIGNE.

Je garde un excellent souvenir de mon passage dans son laboratoire.

*Qu'il trouve ici toute la reconnaissance que je lui porte pour m'avoir accueillie.*

A Messieurs les professeurs André CHRYSOCHOOS et Qing-Ping SUN.

Ils ont accepté la tâche de rapporteurs au sein de la commission d'examen.

A Messieurs les professeurs Günay ANLAS, Jean-Baptiste LEBLOND, Habibou MAITOURNAM et Etienne PATOOR.

Ils ont activement participé au jury de soutenance.

Un merci particulier au Professeur Qing-Ping SUN qui a fait le voyage depuis Hong-Kong et au Professeur Günay ANLAS venu d'Istanbul.

*Qu'ils soient chaleureusement remerciés de leurs remarques et conseils.*

A Messieurs Ky DANG VAN et Quoc-Son NGUYEN.

Il m'ont toujours témoigné une grande bienveillance et ont suivi l'avancement du travail avec intérêt.

A Monsieur Andrei CONSTANTINESCU.

Ma participation à son enseignement comme monitrice et ses conseils bienveillants m'ont beaucoup appris.

A Messieurs Benoît DELATTRE, Claude STOLZ et Lev TRUSKINOVSKY.

*Que tous trouvent ici le témoignage de ma reconnaissance.*

A tous les enseignants-chercheurs de l'équipe, Anne-Lise, Corinne, Bertrand, Frédéric, Olivier, Yongjun.

Ils m'ont conseillé utilement.

A Patrice, Alain et Lahcène.

Ils ont participé avec beaucoup de gentillesse à mes expériences.

A Xue.

J'ai partagé avec elle le bureau dans une ambiance fraternelle.

A tous mes collègues thésards et stagiaires.

*A tous, mes sincères remerciements.*

A Victoire, Marie-Alix, Jean-Baptiste, Olivier et à tous les amis de Nanterre, de la CVX et de Roc.

A Jean-Philippe, Bénédicte et Mathilde.

A mon Grand-Père.

Il m'a toujours encouragée.

A mes parents.

Ils m'ont soutenue tout au long de mes études.

*Toute mon affection.*

# CONTENTS

1	Introduction	1
1.1	Introduction and motivation	1
1.2	Overview of Shape Memory Alloys	3
1.2.1	The martensitic transformation	3
1.2.2	Different behaviors	3
1.2.3	Applications of Shape Memory Alloys	7
1.3	Research objectives	7
1.4	Outline of dissertation	8
1.5	Notations used in the thesis	9
2	The ZM models	12
2.1	Constitutive models for Shape Memory Alloys	12
2.2	Review of the ZM models	14
2.2.1	Presentation of the model	14
2.2.2	Extension to cyclic loading	17
2.3	Analytical solution in torsion	20
2.3.1	Position of the problem and main hypotheses	20
2.3.2	Stress-strain response	21
2.3.3	Results	24
2.3.4	Evolution of the response in the section and torque-angle response	27
2.4	Numerical resolution: return mapping algorithm	27
2.4.1	Position of the problem	27
2.4.2	Presentation of the return mapping algorithm	29
2.4.3	Results	35
2.5	Conclusion and prospects	46
3	Modeling tensile-compressive asymmetry	47
3.1	Literature review on tensile-compressive asymmetry	47
3.1.1	Experimental observations	47
3.1.2	Different models for tensile-compressive asymmetry	49
3.2	Tensile compressive asymmetry in the ZM model	50
3.2.1	Mathematical framework of Raniecki and Mroz	50
3.2.2	Introducing the third invariant	51
3.2.3	Parameters identification procedure	54
3.3	Validation	55
3.3.1	Comparison with experimental results	55
3.3.2	Comparison with the phase change yield function of Orgeas and Favier [1998]	57
3.4	Conclusion	57
4	Thermomechanical coupling	60
4.1	Experimental evidence of thermomechanical coupling in SMA	61
4.1.1	Strain rate dependence	61
4.1.2	Influence of geometry and heat boundary conditions	62
4.1.3	Cyclic evolution	62

4.2	Literature review of the thermomechanical modelling	63
4.2.1	Main ideas of the macroscopic modeling	63
4.2.2	The different models	64
4.3	Introducing the thermomechanical coupling in the ZM model	65
4.3.1	Derivation of the heat equation	65
4.3.2	Position of the problem and getting the discrete equations	66
4.4	Results and interpretation	68
4.4.1	Experimental validation	70
4.4.2	Influence of the different heat sources	74
4.4.3	Influence of geometry and boundary conditions on hysteresis area	74
4.5	Extension to the cyclic behavior	76
4.5.1	Experimental investigation	76
4.5.2	Modelling	84
4.5.3	Validation of the coupled model	85
4.6	Conclusion	92
5	Numerical computation of the stabilized cycle	93
5.1	Literature review on the numerical methods	93
5.1.1	Shakedown	94
5.1.2	Direct methods	94
5.2	The Direct Cyclic Method for SMA behavior	95
5.2.1	Main ideas	95
5.2.2	Numerical algorithm	96
5.2.3	Results	99
5.3	Conclusion	103
6	Fatigue	104
6.1	Literature review on the fatigue of SMAs	104
6.1.1	Metallurgical aspects	105
6.1.2	Fatigue criteria	106
6.1.3	Influence of thermomechanical coupling on the fatigue behavior of SMAs	106
6.2	Modified energy-based criterion	108
6.2.1	Tensile-compressive fatigue results from Moumni et al. [2005]	108
6.2.2	Accounting for the role of the hydrostatic pressure in the fatigue criterion	108
6.2.3	Extension to torsion experiments	110
6.3	Prospects	113
6.3.1	Accounting for the influence of thermomechanical coupling	113
6.3.2	Detection of the crack initiation	114
6.4	Conclusion	118
7	Conclusion	119
A	Thermodynamics of irreversible processes	121
A.1	First law of thermodynamics: energy balance	121
A.2	Kinetic energy theorem	122
A.3	Second law of thermodynamics	122
A.4	Clausius-Duhem inequality	122
B	Generalized standard materials with internal constraints	124
B.1	Normal state variables	124

b.2	Method of two potentials	125
b.3	Case of dependent state variables	126
Bibliography		127

## LIST OF FIGURES

Figure 1	Schematic phase diagram of SMA. The different lines stand for the different properties: orientation of martensite (path $b \rightarrow c$ ), pseudoelasticity (path $f \leftrightarrow g$ ), superthermal effect (path $h \leftrightarrow i$ ). 5
Figure 2	Thermomechanical response for the shape memory effect in the stress-strain-temperature diagram. 5
Figure 3	Stress-strain curve for the pseudoelastic response of an SMA 6
Figure 4	Strain-temperature response for the assisted two-way shape memory effect. 6
Figure 5	Cyclic stress-strain response. 18
Figure 6	Position of the problem 21
Figure 7	Definition of the direct transformation radii 22
Figure 8	Evolution of the stress field in the cross section of the cylinder: (a) for different loading angles and (b) for different unloading angles. $\phi_{\max} = 17^\circ$ . In these figures, $E_A = E_M = 24000$ MPa. 25
Figure 9	Stress-strain response at different radii: $r=5$ mm (blue), 15 mm (red), 25 mm (magenta), 35 mm (black), 45 mm (green). In this figure, $E_A = E_M = 24000$ MPa. 25
Figure 10	Evolution of the stress field in the cross section of the cylinder: (a) for different loading angles, and (b) for different unloading angles. $\phi_{\max} = 17^\circ$ . In these figures, $E_A = 61500$ MPa and $E_M = 24000$ MPa. 26
Figure 11	Stress-strain response at different radii: $r=5$ mm (blue), 15 mm (red), 25 mm (magenta), 35 mm (black), 45 mm (green). In this figure, $E_A = 61500$ MPa and $E_M = 24000$ MPa. 28
Figure 12	Torque-angle curve. In this figure, $E_A = E_M = 24000$ MPa. 28
Figure 13	Stress-strain response to an imposed displacement of 8 mm in tension. 37
Figure 14	Stress-strain response at a point situated on the external radius of the cylinder and subjected to a $25^\circ$ torsion angle. 37
Figure 15	Comparison of analytical (red) and numerical (blue) stress-strain responses for points situated at different radii specified under each figure. In these simulations, the parameters come from Table 5, except $G=4.6556$ MPa. 37
Figure 16	Comparison of analytical (red) and numerical (blue) torque-angle responses for a maximum angle of $20^\circ$ . 38
Figure 17	Stress-strain responses for tension-torsion loading paths. The maximum imposed torsion angle is $30^\circ$ , and the maximum tensile displacement $\xi_{\max}$ is specified under each figure. In all figures, the blue line is related to the shear response, the red one to the tensile components and the black one to the equivalent stress-strain response. 38
Figure 18	Evolution of the orientation yield function for the different loading paths. The black dotted line corresponds to zero. The black (resp. blue, red) curve corresponds to a maximum tensile displacement of 2 mm (resp. 5 mm and 7 mm) 38
Figure 19	Martensite orientation stress-strain response in tension. 39

Figure 20	(a) Loading path: from a natural unloaded state, the material is loaded along the blue, red, black, and finally magenta paths. (b) Shear strain vs. tensile strain response corresponding to the loading path presented in (a). 40
Figure 21	Stress-strain responses for both components, corresponding to the loading path plotted in Fig. 20. 40
Figure 22	(a) Loading path: from a natural unloaded state, the material is loaded along the blue, red, black, and finally magenta paths. (b) Shear strain vs. tensile strain response corresponding to the loading path presented in (a). 41
Figure 23	Stress-strain responses for both components, corresponding to the loading path plotted in Fig. 22a. 41
Figure 24	Stress-strain responses for pure tension loading (a) or pure torsion loading (b). 42
Figure 25	Proportional shear-tension loading. (a) Evolution of the mechanical response. (b) Evolution of the orientation strain components. 43
Figure 26	(a) and (b) 3 % tension strain followed by 2 % shear strain and unloading. (c) and (d) 3 % shear strain followed by 2 % tensile strain and unloading. 43
Figure 27	(a) Geometry and boundary conditions of the simulated specimen. Zero displacements are imposed perpendicularly to the colored surfaces. (b) Evolution of the loading direction with respect to time. The normalized tensile force in the z-direction (resp. the normalized compressive force in the x-direction) is plotted in black (resp. in red). 44
Figure 28	(a) Stress strain response in the x-direction. (b) Stress-strain response in the z-direction. (c) Evolution of different components of the orientation tensor with respect to the kinematic time; the solid line stands for the y-direction, the dotted line – for the z-direction and the dotted line - . for the x-direction. 45
Figure 29	Evolution of the different yield functions with respect to the kinematic time. 45
Figure 30	Experimental stress-strain curves in tension and in compression for a pseudoelastic NiTi SMA. The figure is taken from Orgeas and Favier [1998]. 48
Figure 31	Experimental stress-strain curves in tension and in compression for a martensitic NiTi SMA. The figure is taken from Orgeas and Favier [1998]. 48
Figure 32	Geometry and boundary conditions of the problem 55
Figure 33	Simulated (solid lines) vs. experimental (circles) superelastic stress-strain curves in tension (pink) and in compression (blue). 56
Figure 34	Simulated (solid lines) vs. experimental (circles) stress-strain curves in tension (pink) and in compression (blue) for martensite orientation. 58
Figure 35	Comparison of the prediction of the direct phase change yield stresses in tension (green), compression (blue) and shear (pink) given by the criterion of Orgeas and Favier (dotted line) and by our criterion (solid line) with experimental data from Orgeas and Favier (markers). 58
Figure 36	Geometry and boundary conditions of the specimen. 70
Figure 37	Experimental vs. numerical stress-strain and temperature-strain curves for a strain rate of $4 \cdot 10^{-5} \text{ s}^{-1}$ . 71
Figure 38	Experimental vs. numerical stress-strain and temperature-strain curves for a strain rate of $4 \cdot 10^{-4} \text{ s}^{-1}$ . 71

Figure 39	Experimental vs. numerical stress-strain and temperature-strain curves for a strain rate of $4.10^{-3} \text{ s}^{-1}$ . 72
Figure 40	Experimental vs. numerical stress-strain and temperature-strain curves for a strain rate of $4.10^{-2} \text{ s}^{-1}$ . 72
Figure 41	(a) Experimental and simulated maximum amplitudes of temperature variation during a loading cycle. The bars indicate uncertainties on experimental measurements. (b) Deviation from experimental measurements of temperature variation amplitudes calculated using the coupled ZM model. 73
Figure 42	Evolution of the mechanical and thermal responses depending on whether only the latent heat or the intrinsic dissipation or both heat sources are considered in solving the heat equation. 74
Figure 43	Evolution of the hysteresis area with the strain rate. In this simulation, $h = 50 \text{ W.m}^{-2}.\text{K}^{-1}$ , $T_{\text{ext}} = 70 \text{ }^{\circ}\text{C}$ , $r = 1 \text{ mm}$ . 75
Figure 44	(a) Variation of the slopes of the phase change plateaus with respect to strain rate. (b) Evolution of the phase change yield stress with respect to the strain rate in the Clapeyron diagram. In both figures, the quasistatic curve is shown in blue, while the red curve corresponds to a strain rate of $2.10^{-3} \text{ s}^{-1}$ . 77
Figure 45	Evolution of the hysteresis area with the strain rate for (a) different convective heat transfer coefficients ( $r = 1 \text{ mm}$ ) and for (b) specimens with different radii ( $h = 50 \text{ W.m}^{-2}.\text{K}^{-1}$ ). In both simulations, $T_{\text{ext}} = 70 \text{ }^{\circ}\text{C}$ . 77
Figure 46	Reproducibility of the first stress-strain cycle at different strain rates. 78
Figure 47	Reproducibility of the 20th stress-strain cycle at different strain rates. 78
Figure 48	Reproducibility of the 40th stress-strain cycle at different strain rates. 79
Figure 49	Evolution of the average temperature for cycles 1, 20 and 40 at $\dot{\epsilon} = 1.10^{-4} \text{ s}^{-1}$ . 79
Figure 50	Evolution of the average temperature for cycles 1, 20 and 40 at $\dot{\epsilon} = 5.10^{-4} \text{ s}^{-1}$ . 79
Figure 51	Evolution of the average temperature for cycles 1, 20 and 40 at $\dot{\epsilon} = 5.10^{-3} \text{ s}^{-1}$ . 79
Figure 52	Stress-strain curves of the first cycles for all tested strain rates. 80
Figure 53	Evolution of the slopes of the direct phase change plateau with respect to the strain rate. 80
Figure 54	Evolution of the hysteresis area. 81
Figure 55	(a) Cyclic stress-strain response of an SMA wire subject to pseudoelastic cyclic loading. (b) Evolution of the hysteresis area with respect to the number of cycles. For both figures, $\dot{\epsilon} = 10^{-3} \text{ s}^{-1}$ . 81
Figure 56	(a) Evolution of the martensite start yield stress with respect to the strain rate. (b) Evolution of the temperature at the phase change yield stress. 82
Figure 57	Stabilization of the temperature evolution during cycling for three different strain rates. 82
Figure 58	(a) and (c): Evolution of the minimum (circles) and maximum (crosses) temperatures with respect to the strain rate. (b) and (d): Evolution of the temperature amplitudes with respect to the strain rate. 83
Figure 59	Geometry of the specimen used for the numerical simulations 87
Figure 60	Comparison of the first cycle obtained by the experiments (blue) and the simulation (red) for the different strain rates. 87

Figure 61	(a) Comparison of the evolution of the hysteresis areas obtained by the experiments (blue) and by the simulations (red). (b) Error on the numerical estimation of the area by comparison with the experimental area. 87
Figure 62	(a) Comparison of the minimum (circles) and maximum (crosses) temperatures over the first cycle obtained by the experiments (blue) and by the simulations (red). (b) Error on the numerical estimation of these temperatures by comparison with the experimental values. 89
Figure 63	Comparison of the 10th cycle obtained by the experiments (blue) and the simulation (red) for the different strain rates. 89
Figure 64	(a): Comparison of the hysteresis areas obtained from the experiments (blue) and from the simulations (red) for the 10th cycle (transient response). (b): Comparison of the maximum (crosses) and minimum (circles) temperature values over the 10th cycle obtained by the experiments (blue) or by the simulations (red). 90
Figure 65	Comparison of the stabilized cycle obtained by the experiments (blue) and the simulation (red) for the different strain rates. 90
Figure 66	(a) Comparison of the evolution of the hysteresis areas obtained by the experiments (blue) and by the simulations (red) for the stabilized cycle. (b) Error on the numerical estimation of the area by comparison with the experimental one. 91
Figure 67	(a) Comparison of the minimum (circles) and maximum (crosses) temperatures over the stabilized cycle obtained by the experiments (blue) and by the simulations (red). (b) Error on the numerical estimation of these temperatures by comparison with the experimental values. 91
Figure 68	Comparison of the stress-strain curves (a) and of the stabilized cycles (b) obtained using the incremental method (solid line) and the Direct Cyclic Method (dotted line) for a tensile cyclic loading. 101
Figure 69	Comparison of the stress-strain curves (a) and of the stabilized cycles (b) obtained using the incremental method (blue curves) and the Direct Cyclic Method (red curves) for a point situated on the external radius of the cylinder which is subject to a torsion loading. 101
Figure 70	Comparison of the stress-strain curves (a) and of the stabilized cycles (b) obtained using the incremental method (blue curves) and the Direct Cyclic Method (red curves) for a point situated on the upper face in tension, near the cantilevered section. The beam is subject to a bending loading. 102
Figure 71	Comparison of the stress-strain curves (a) and of the stabilized cycles (b) obtained using the incremental method (blue curves) and the Direct Cyclic Method (red curves) for a point situated on the lower face in compression, near the cantilevered section. The beam is subject to a bending loading. 102
Figure 72	Evolution of the hysteresis area vs. the number of cycles. 109
Figure 73	Evolution of the hysteresis area at the stabilized cycle with respect to the number of cycles to failure for the initial energy-based criterion. 109
Figure 74	Estimated vs. experimental lifetime for the experiments at different R ratios for the energy-based criterion. 111
Figure 75	Modified energy-based criterion 111
Figure 76	Estimated vs. experimental lifetime for the modified energy-based criterion. 112
Figure 77	Modified energy-based criterion for tension and torsion experiments. 112

Figure 78	Estimated vs. experimental lifetimes for the modified energy-based criterion for both tension and torsion tests. 115
Figure 79	Modified energy-based criterion for the rotating-bending experiments performed by Matsui et al. [2004]. 115
Figure 80	Estimated vs. experimental lifetime given by the modified energy-based criterion (squares) and by the Manson-Coffin criterion from Matsui et al. [2004] (diamonds). 116
Figure 81	Modified energy-based criterion for our rotating-bending experiments. Diamonds (resp. circles) stand for strain amplitude of 2.5 % (resp. 2 %). Red (resp. blue and magenta) points stand for experiments performed at 50 °C (resp. 70 °C and 35 °C). 116
Figure 82	Estimated vs. experimental lifetime for the modified energy-based criterion. Diamonds (resp. circles) stand for strain amplitude of 2.5 % (resp. 2 %). Red (resp. blue and magenta) points represent experiments performed at 50 °C (resp. 70 °C and 35 °C). The blue lines stand for two and half the experimental lifetime, while the external black lines represent three and third the experimental lifetime. 117

## LIST OF TABLES

Table 1	Notations used in the thesis. 11
Table 2	Model parameters 26
Table 3	Return mapping algorithm for proportional loadings. 31
Table 4	Return mapping algorithm for the cyclic model. 32
Table 5	Model parameters 35
Table 6	Model parameters 56
Table 7	Deviation of the different criteria with experimental data. 58
Table 8	Algorithm for the thermomechanical coupled ZM model. 69
Table 9	Model parameters 70
Table 10	Model parameters 86
Table 11	Algorithm for the Direct Cyclic Method. 98
Table 12	Model parameters 99

# 1

## INTRODUCTION

---

1.1	Introduction and motivation	1
1.2	Overview of Shape Memory Alloys	3
1.2.1	The martensitic transformation	3
1.2.2	Different behaviors	3
1.2.3	Applications of Shape Memory Alloys	7
1.3	Research objectives	7
1.4	Outline of dissertation	8
1.5	Notations used in the thesis	9

---

### 1.1 INTRODUCTION AND MOTIVATION

For more than thirty years, industries and scientists have shown a great interest in studying a specific class of materials, called "smart materials". These materials exhibit interesting properties and could be used in a wide variety of industrial applications. Shape Memory Alloys (SMAs) are one specific kind of smart materials. Their specific behaviors arise from the possibility of SMAs to undergo a reversible martensitic transformation, which can be induced either by thermal, mechanical or thermomechanical loadings. The material can sustain large reversible deformations (until 10 %), recovered either by heating (shape memory effect) or by mechanical unloading (pseudoelasticity). Discovered in the 1930's, their first applications came only thirty years later, when some Nickel-Titanium alloys were found to exhibit the Shape Memory effect. Since then, the shape memory effect and the pseudoelasticity, their two main properties, have promoted their use in many applications ranging from the biomedical field (as orthodontic wires, stents...) to the aeronautic industries, as actuators. Shape Memory Alloys are also used in civil engineering as seismic dampers.

In many of these applications, SMA structures are subject to cyclic thermomechanical loadings that may induce fatigue failure of the structure after a small number of cycles. Fatigue studies have begun in the 1850's after the Versailles-Paris train accident for classical metals. Wöhler curves (also called SN curves) exhibit two main fatigue domains with different properties: the high-cycle fatigue domain, where structures have an infinite lifetime and are shown to behave elastically at both the macroscopic and the mesoscopic scales. Energy dissipation may occur in some grains but remains confined (elastic shakedown at the mesoscale); the low-cycle fatigue domain, where structures fails after a small number of cycles, because of energy dissipation at each cycle.

Fatigue of Shape Memory Alloys deals with low-cycle fatigue, as we are mainly interested in the fatigue occurring in the pseudoelastic domain. Fatigue studies for SMAs remain scattered, in the sense that no 3D criterion including all major effects associated with SMA has yet been proposed. The different studies of the literature include experiments on the effect of different parameters (either loading parameters or metallurgical properties) on the fatigue lifetime, met-

allurgical studies, or few fatigue criteria, which are mainly restricted to 1D Manson-Coffin type criteria.

This thesis aims to fill this gap by proposing a comprehensive approach for fatigue design of SMA structures. To this end, a precise constitutive law, reproducing all main effects displayed by the material, is required for determining the thermomechanical asymptotic state with good accuracy. Indeed, it is well known that for metallic structures, the fatigue lifetime is investigated using the stabilized thermomechanical state as an input to a fatigue criterion.

For Shape Memory Alloys under pseudoelastic loading, we identified four issues that must be taken into account in order to get an accurate evaluation of the fatigue lifetime of a SMA structure. First, a reliable constitutive law that takes into account the evolution of the yield stresses with temperature and loading direction is required; this includes the tension-compression asymmetry exhibited by shape memory alloys. Second, the constitutive law must consider the effect of the latent heat of phase transformation which induces a strong thermomechanical coupling that influences drastically the mechanical response. Third, an original numerical method to compute the stabilized state of the structure must be developed. In fact, the classical incremental method may lead to prohibitive computation time. Finally, the fatigue criterion should be defined and validated for 3D structures, and should account for all the observed thermomechanical effects, which are not reproduced by simple Manson-Coffin laws.

Our work aims at developing such a fatigue approach that considers the aforementioned issues. This is achieved in three steps.

The first step is devoted to the computing of the asymptotic state. It consists in proposing a cyclic constitutive law accounting for all the pre-cited effects able to predict the stabilized state of a SMA structure. Among the cyclic models available in the literature, we choose to work on the ZM models developed by [Zaki and Mounni \[2007a,b\]](#), because both monocycle and cyclic models are developed within the same framework, at a macroscopic scale; it allows the prediction of any behavior of SMAs with only two driving mechanisms (phase transformation and orientation of martensite), including 3D non proportional cyclic loadings. As the ZM models do not account for tensile-compressive asymmetry nor for thermomechanical coupling, these two effects are introduced in the models within this thesis, and the extended models are validated against experimental data. Modelling the thermomechanical coupling is achieved for both the monocycle and the cyclic models. The developed extensions of the models widen the validity domain of the ZM models, to tension, compression and torsion loadings, for loading rates ranging from  $10^{-5}$  to  $10^{-2} \text{ s}^{-1}$ .

The second step concerns the development of a numerical method allowing direct determination of the asymptotic state of a SMA structure submitted to cyclic loadings.

The third step deals with the prediction of the fatigue lifetime of the structure using the thermomechanical stabilized state computed in the two first steps. To this end, a modified energy-based criterion is proposed, which relates the fatigue lifetime of the structure to a combination of the hysteresis area at the stabilized cycle and of the maximum hydrostatic pressure. It is shown that choosing the hysteresis area as a fatigue parameter allows taking into account the effect of thermomechanical coupling on the fatigue lifetime. An attempt of validation for torsion experiments is given.

The next section is devoted to a brief description of the unusual behaviors and the applications of Shape Memory Alloys. A more detailed description of the objectives of the PhD as well as the outline of the dissertation are then given.

## 1.2 OVERVIEW OF SHAPE MEMORY ALLOYS

Shape Memory Alloys (SMAs) are metallic alloys which exhibit interesting properties when subject to thermomechanical loadings: they can recover large inelastic strains upon heating (shape memory effect) or accommodate large strains that can be recovered with the removal of the load (pseudoelasticity). The unusual properties of SMAs are associated with their capability to undergo the martensitic phase transformation.

### 1.2.1 The martensitic transformation

The martensitic transformation is a solid-solid phase change, from a solid phase called austenite into another solid phase with lower crystallographic symmetry called martensite. The lower symmetry of this phase enables the existence of several martensite variants defined by the orientation of their habit plane<sup>1</sup>. The existence of a martensitic variant depends on the thermomechanical state. Two types of martensitic structures may exist within a SMA:

- self-accommodating martensite, when all variants are equiprobable. The martensite is said to be "twinned" in this case and no macroscopic strain is observed.
- detwinned martensite, when a stress state favors the growth of some particular variants of martensite; this leads to the apparition of a macroscopic strain.

In SMAs, the martensitic transformation is a thermoelastic transformation, because the interfaces between phases are mobile enough to allow the shrinkage of the martensite plates through a backward movement [cf. [Otsuka and Wayman, 1999](#)]; it is crystallographically reversible. The crystallographical theory of the martensitic transformation has been studied by [Wechsler et al. \[1953\]](#) and [Bowles and Mackenzie \[1954\]](#). The martensitic transformation is characterized by an inelastic transformation of the crystal lattice. It is a displacive transformation involving collective and cooperative motions of atoms, on a distance smaller than the lattice parameters, with no diffusion. The martensitic transformation is a first-order transition; during a martensitic transformation, martensite and austenite coexist, separated by an invariant plane. Volumetric and shear strains are created, with shear strain being far greater. During the transformation, a latent heat is absorbed or released, according to the direction of transformation. The amount of heat produced is proportional to the volume fraction of the transformed material.

Finally, the transformation is greatly influenced by temperature and by stress; the influence of stress is related to the displacive character of the martensitic transformation. It is possible to summarize the different ways the martensitic transformation can occur in a stress-temperature diagram (cf. Fig. 1). In three regions separated by the transformation lines, the material is single-phased and its deformation is thermoelastic. Forward and reverse transformations, reorientation of twinned martensite and detwinning occur when the loading path crosses a transformation line. The behavior of shape memory alloys strongly depends on the thermomechanical loading path.

### 1.2.2 Different behaviors

This section introduces the different behaviors of SMAs according to the loading path.

<sup>1</sup> A habit plane is a crystallographic plane or system of planes along which certain phenomena such as twinning occur.

### *One Way Shape Memory Effect*

The Shape Memory Effect is probably the most well-known property of shape memory alloys. The material response is represented in the stress-strain-temperature diagram shown in Fig. 2. An initially austenitic structure is first cooled at zero strain to get twinned martensite without macroscopic strain (path (a)  $\rightarrow$  (b) in Figs. 1 and 2). The SMA is then deformed (path (b)  $\rightarrow$  (c) in Figs. 1 and 2), the martensite gets detwinned, leading to the creation of inelastic strains, which remain after unloading (path (c)  $\rightarrow$  (d) in Figs. 1 and 2). The apparent permanent strain is recovered by heating above a temperature  $A_f^0$ , characteristic of the material (path (d)  $\rightarrow$  (e) in Figs. 1 and 2). Temperature  $A_f^0$  is the austenite finish temperature, at which reverse transformation is completed.

### *Pseudoelasticity*

Pseudoelasticity is associated with a stress-induced martensitic transformation. The stress-strain curve is schematically represented on Fig. 3. An austenitic material is loaded thermoelastically until the martensitic yield stress is reached: the direct transformation begins and detwinned martensite is directly formed (path (f)  $\rightarrow$  (g) in Figs. 1 and 3). The large inelastic strain obtained at the end of the load is recovered during unloading (path (g)  $\rightarrow$  (f) in Figs. 1 and 3). As the yield stresses for direct and reverse phase change are different, this gives rise to an hysteresis, which reflects the energy dissipated in the cycle.

### *Assisted two-way shape memory effect*

The assisted two-way shape memory effect (or superthermal effect) is associated with a temperature induced transformation under constant stress (path (h)  $\leftrightarrow$  (i) in Figs. 1 and 4). The applied stress favors the nucleation of preferentially oriented martensite variants: the martensite is detwinned. Thus, by cooling the material, a macroscopic strain is obtained which is recovered by heating above the  $A_f$  temperature<sup>2</sup> (cf. Fig. 4).

### *Two-Way Shape Memory Effect*

The two-way shape memory effect has been reported for the first time by Perkins [1974]. Contrary to the previous effects, it is an acquired (not intrinsic) property of Shape Memory Alloys. Cyclic repetitions of a thermomechanical loading path are necessary to induce it (training phase). Indeed, during the heating phase of the one-way shape memory effect, all the inelastic strain is not recovered and a residual strain remains, which accumulates during the cycles until saturation. This residual strain introduces microstructural oriented defects and internal stresses inside the structure, that favor some variants of martensite. When the material is trained, cooling the structure in the absence of external stress produces a transformation strain because of the internal stress state existing inside the structure. It is thus possible to transit between two stable shapes by heating or cooling without any applied stress assistance.

The loading path of the two-way shape memory effect is similar to the one of the superthermal effect (cf. Fig. 4).

### *Rubber-like effect*

The aging of the martensite phase enables the reversal of martensite twins: the inelastic strain formed during loading is recovered, leading to a reversible twinning and detwinning of martensitic variants. This effect is called rubber-like effect and has been discovered by Olander in 1932 in AuCd alloys.

<sup>2</sup>  $A_f$  stands for the austenite finish temperature under a stress  $\sigma$ .

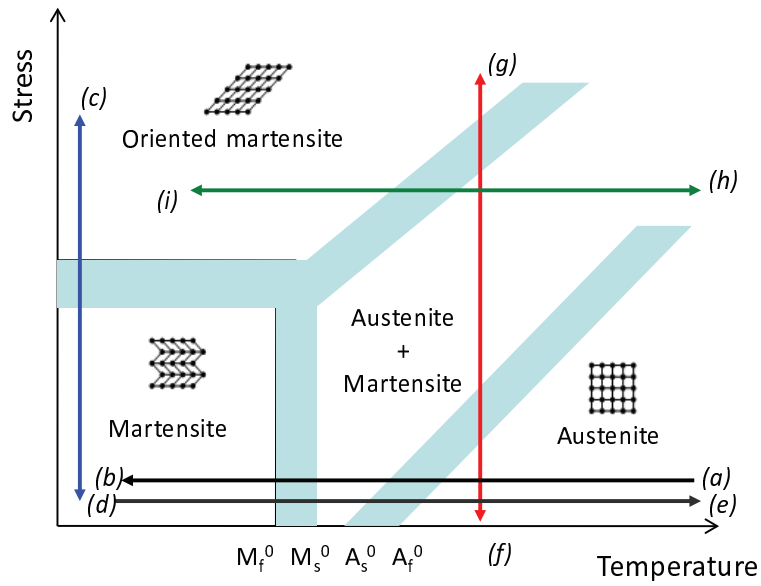


Figure 1. Schematic phase diagram of SMA. The different lines stand for the different properties: orientation of martensite (path  $b \rightarrow c$ ), pseudoelasticity (path  $f \leftrightarrow g$ ), superthermal effect (path  $h \leftrightarrow i$ ).

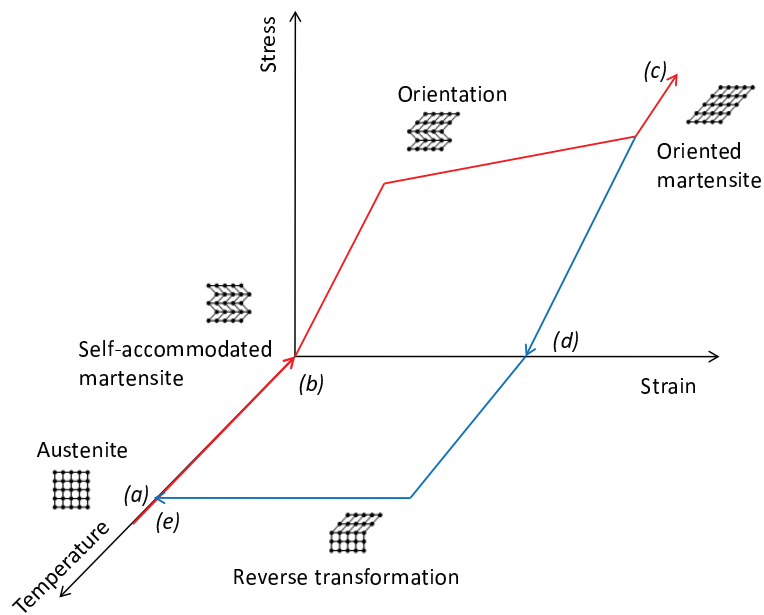


Figure 2. Thermomechanical response for the shape memory effect in the stress-strain-temperature diagram.

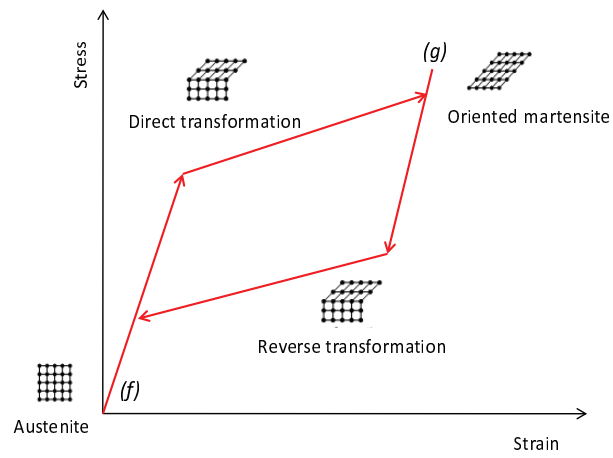


Figure 3. Stress-strain curve for the pseudoelastic response of an SMA

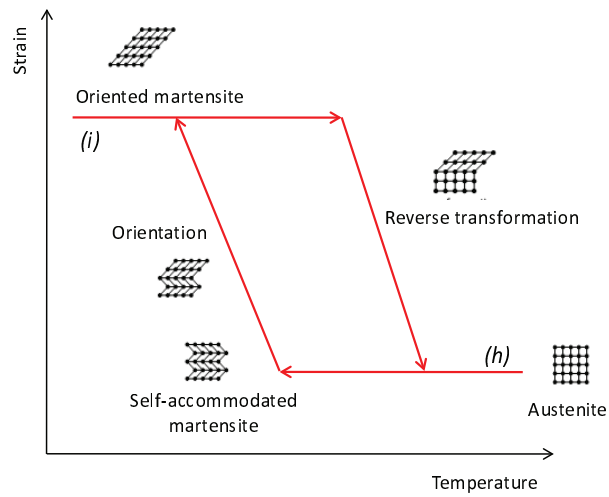


Figure 4. Strain-temperature response for the assisted two-way shape memory effect.

### 1.2.3 Applications of Shape Memory Alloys

The different behaviors of SMAs make them promising candidates for a wide range of applications, namely:

- In the biomedical field, NiTi SMA is used for manufacturing stents, bone clips, orthodontic wire, ..., because of the biocompatibility of NiTi alloy.
- In the aeronautics industry, they are used as actuators to open or close the trailing edge flaps of drones, as variable-geometry chevrons (VGCs) [Mabe et al., 2006], adaptative wings.
- In civil engineering, their damping capacity makes them good candidates for dissipative devices in seismic regions.

## 1.3 RESEARCH OBJECTIVES

A good understanding of fatigue in SMAs is necessary to improve the safety of the SMA materials in industrial applications as shape memory materials usually operate under cyclic loadings. Designing structures against fatigue requires a precise prediction of the thermomechanical stabilized state as well as a reliable fatigue criterion. The aim of this work is to propose a comprehensive approach for fatigue design of SMA structures. This approach is split into three major steps:

1. the development of a suitable constitutive law, that is able to predict with good accuracy the cyclic thermomechanical response of a SMA;
2. the development of a numerical method allowing direct determination of the asymptotic state;
3. the study of the fatigue behavior and the development of a fatigue criterion to predict the fatigue lifetime of the structure and the location of the crack initiation.

To this aim, the objectives of this research are to:

- Propose extensions of the constitutive models developed by Zaki and Moumni [cf. Zaki and Moumni, 2007a,b] to account for different effects that are not reproduced by the actual model, namely:
  - tensile-compressive asymmetry,
  - thermomechanical coupling,
  - simulation of non proportional loadings...

This is the aim of chapters 2 to 4.

- Develop an efficient numerical method for the computation of the stabilized cycle; this is done in chapter 5.
- Study the fatigue behavior, and especially:
  - validate the fatigue criterion proposed by Moumni et al. [2005];
  - study the frequency and temperature dependencies of the fatigue life.

This is the aim of chapter 6.

## 1.4 OUTLINE OF DISSERTATION

The outline of the dissertation is the following:

- The second chapter is devoted to a review of the constitutive models developed by Zaki and Moumni (ZM models). After a short presentation of the two models, an analytical solution of an SMA cylinder subjected to torsion loading is proposed; the solution shows non monotonic evolution of the stress along the radius of the cylinder during unloading. Finally, specific return mapping algorithms are developed for the ZM constitutive laws. Some results of structures subjected to different proportional and non proportional loading paths are exhibited using these return mapping algorithms.

- The third chapter introduces tensile-compressive asymmetry in the ZM monocycle model. Uneven expressions of different quantities are defined, which are functions of both the second and third invariants. This extension of the ZM model is validated with experimental data in tension and compression simultaneously for pseudoelastic and orientation loadings. Moreover, the model predicts tension, compression and shear yield stresses over a large range of temperature with good accuracy.

- The fourth chapter deals with thermomechanical coupling in SMAs. Strong dependence of the phase change yield stresses on temperature together with the presence of heat sources due to phase change lead to a strong thermomechanical coupling in SMA. Consequently, the mechanical response becomes dependent on strain rate, unless temperature variation is avoided by external control. It is then important to be able to predict such variations of the mechanical response. This is accounted for in the model by coupling the heat equation with the mechanical equilibrium and constitutive equations. The problem exhibits strong couplings: an evolution of the fraction of phases changes temperature, while the change in temperature leads to a change in yield stress and thus in the further evolution of the fraction of phases. The proposed algorithm takes into account these strong couplings. Both monocycle and cyclic models are extended and validated against experimental data. The main experimental features are reproduced with good accuracy by the coupled models, namely changes in the slopes of the phase change plateaus and in the hysteresis area. The changes in mechanical response are shown to depend on the geometry and on the thermal boundary conditions, which is experimentally verified. The main difficulty arises from the heterogeneous character of phase change, leading to localization of the temperature variation; as our model is at a macroscopic scale, no influence of the microscopic structure is accounted for and only an average response is estimated.

- The fifth chapter proposes a direct method to compute the mechanical stabilized state of an SMA structure subjected to cyclic loadings. Among the different methods existing in literature, we choose to extend the Direct Cyclic Method. Numerical results show that, for structures subjected to proportional loadings, a considerable gain of computation time is achieved using this direct method in comparison with the classical incremental method.

- In the last chapter finally, the fatigue of Shape Memory Alloys is discussed. The energy-based criterion, initially proposed by [Moumni et al. \[2005\]](#), is extended to account for the role of the hydrostatic pressure on the fatigue lifetime of structures. An attempt of validation of the criterion for torsion experiments is proposed. Finally, the influence of the thermomechanical coupling on the fatigue property of SMAs is discussed.

As a conclusion, a summary of the main novelties, a global review of our approach, as well as some prospects are given.

## 1.5 NOTATIONS USED IN THE THESIS

We summarize in this section the main notations used in all the manuscript. All tensors or vectors are written in bold.

Notation	Meaning	Expression
$\mathbf{1}$	Second-order identity tensor	
$\text{tr } \mathbf{M}$	Trace of tensor $\mathbf{M}$	$\sum_i M_{ii}$
$\text{dev } \mathbf{M}$	Deviator of $\mathbf{M}$	$\mathbf{M} - \frac{1}{3} (\text{tr} \mathbf{M}) \mathbf{1}$
$M_{VM}$	Von-Mises equivalent norm of $\mathbf{M}$	$\sqrt{\frac{3}{2} \text{dev} \mathbf{M} : \text{dev} \mathbf{M}}$
$\alpha$	Dissipative variable	
$\beta$	Non dissipative variable	
$\boldsymbol{\epsilon}$	Macroscopic strain tensor	$\frac{1}{2} (\nabla \boldsymbol{\xi} + {}^t \nabla \boldsymbol{\xi})$
$\boldsymbol{\epsilon}_{\text{ori}}$	Martensite orientation strain tensor	
$\lambda$	Lagrange multiplier associated with equality constraint	
$\lambda_{\text{eq}}$	Equivalent Lamé coefficient	$\frac{\nu E_{\text{eq}}}{(1-2\nu)(1+\nu)}$
$\mu, \nu_1, \nu_2$	Lagrange multipliers associated with inequality constraints	
$\mu_A$	Austenite shear modulus	$\frac{E_A}{2(1+\nu)}$
$\mu_M$	Martensite shear modulus	$\frac{E_M}{2(1+\nu)}$
$\mu_{\text{eq}}$	Equivalent shear modulus	$\frac{E_{\text{eq}}}{2(1+\nu)}$
$\nu$	Poisson coefficient of the material	
$\boldsymbol{\xi}$	Displacement field	
$\boldsymbol{\xi}^d$	Imposed displacement field	
$\rho$	Density of the material	
$\boldsymbol{\sigma}$	Stress tensor	
$\sigma_{VM}$	Von-Mises equivalent stress	$\sqrt{\frac{3}{2} \mathbf{s} : \mathbf{s}}$
$\Psi$	Pseudo-potential of dissipation	

Notation	Meaning	Expression
$A_\alpha$	Thermodynamic force associated to the dissipative variable $\alpha$	$-\frac{\partial \mathcal{W}}{\partial \alpha}$
$c_p$	Specific heat capacity	
$\mathcal{D}$	Total dissipation	$\mathcal{D}_1 + \mathcal{D}_2$
$\mathcal{D}_1$	Intrinsic dissipation	
$\mathcal{D}_2$	Thermal dissipation	
$E_A$	Young modulus of austenite	
$E_{eq}$	Equivalent Young modulus	$\left(\frac{1-z}{E_A} + \frac{z}{E_M}\right)^{-1}$
$El_A$		$\frac{1+\nu}{E_A}$
$El_M$		$\frac{1+\nu}{E_M}$
$El_{MA}$		$El_M - El_A$
$E_M$	Young modulus of martensite	
$\mathbf{f}$	Body force applied on the structure	
$\mathcal{F}_z^1$	Direct phase change yield function	
$\mathcal{F}_z^2$	Reverse phase change yield function	
$\mathcal{F}_{ori}$	Orientation yield function	
$\mathcal{J}$	Interaction energy	
$J_2$	Second invariant of a deviatoric tensor $\mathbf{a}$	$\sqrt{\mathbf{a} : \mathbf{a}} = \frac{1}{2} \text{tr} (\mathbf{a}^2)$
$J_3$	Third invariant of a deviatoric tensor $\mathbf{a}$	$\frac{1}{3} \text{tr} (\mathbf{a}^3)$
$\mathbf{K}$	Equivalent elasticity tensor	$(1-z) \mathbf{K}_A^{-1} + z \mathbf{K}_M^{-1}$
$k$	Specific conductivity	
$\mathcal{L}$	Lagrangian	$\mathcal{W} + \mathcal{W}_l$
$P_A$		$-\frac{\nu}{E_A}$
$P_M$		$-\frac{\nu}{E_M}$

Notation	Meaning	Expression
$P_{MA}$		$P_M - P_A$
$P_{\max}$	Maximum hydrostatic pressure	$\frac{1}{3} \max\{\text{tr}(\boldsymbol{\sigma})\}$
$s$	Entropy density	$-\frac{\partial \mathcal{W}}{\partial T}$
$\mathbf{s}$	Stress deviator	$\text{dev} \boldsymbol{\sigma}$
$\mathbf{S}$	Equivalent compliance tensor	$\mathbf{K}^{-1}$
$T$	Temperature	
$T_0$	A reference temperature	
$\mathbf{T}^d$	Contact force applied on boundary of the structure	
$\mathcal{W}$	Helmholtz free energy of the material	$(1 - z) \mathcal{W}_A + z \mathcal{W}_M + \mathcal{J}$
$\mathcal{W}_A$	Helmholtz free energy of austenite	
$\mathcal{W}_I$	Potential associated with internal constraints	
$\mathcal{W}_M$	Helmholtz free energy of martensite	
$z$	Volume fraction of martensite	

Table 1. Notations used in the thesis.

# 2 | THE ZM MODELS

---

2.1	Constitutive models for Shape Memory Alloys	12
2.2	Review of the ZM models	14
2.2.1	Presentation of the model	14
2.2.2	Extension to cyclic loading	17
2.3	Analytical solution in torsion	20
2.3.1	Position of the problem and main hypotheses	20
2.3.2	Stress-strain response	21
2.3.3	Results	24
2.3.4	Evolution of the response in the section and torque-angle response	27
2.4	Numerical resolution: return mapping algorithm	27
2.4.1	Position of the problem	27
2.4.2	Presentation of the return mapping algorithm	29
2.4.3	Results	35
2.5	Conclusion and prospects	46

---

A global approach for fatigue design requires the computation of the stabilized response of a structure subject to cyclic thermomechanical loadings. The first step is the choice of a constitutive law, that should be, on the one hand sufficiently simple to be easily implemented into a finite element code, to allow the computation of industrial structures by avoiding too large computation times, and on the other hand, sufficiently precise and complete to reproduce the actual behavior of the structure with good accuracy.

This chapter gives an overview of the constitutive models that will be used within the frame of the global approach; these models will be extended in the following chapters and implemented in a finite element code. In first section, the main constitutive models for SMAs are reviewed. In the second section, the original ZM constitutive models for both monocytle and cyclic behaviors of Shape Memory Alloys are presented. In the third section, the monocytle model is used to derive an analytical solution for a boundary value problem involving a Shape Memory Alloy cylinder subjected to torsion. The fourth section develops the return mapping algorithms for both proportional and non proportional pseudoelastic loadings in the case of the ZM models. Finally, some prospects are given.

## 2.1 CONSTITUTIVE MODELS FOR SHAPE MEMORY ALLOYS

Constitutive modelling of SMAs has received considerable attention in the last thirty years. The different models available in the literature are usually classified into three categories: microscale approaches, micro-macro models, and macroscale models.

- Microscopic approaches are interested in modelling processes at the lattice scale, such as nucleation, interface motion, phase change kinetics, twin growth... Among the different contributions, [Falk \[1980\]](#) used the Ginsburg-Landau theory to develop a model for the martensitic

phase transformation, introducing new order parameters to describe nucleation and propagation of the martensitic plates. Different models [*cf.* e.g. Ball and James, 1987; Bowles and Mackenzie, 1954; Wechsler et al., 1953] assumed the existence of an invariant plane [Wayman, 1994] to study the orientation and structure of the martensite plates. Other microscopic models have been proposed by Gall et al. [2001]; Achenbach and Müller [1982]; Sittner and Novak [2000]...

- Micro-macro models have been initiated by Patoor et al. [1988] and combined microscale ingredients, by studying the constitutive behavior at the grain level, and homogenization techniques to obtain the macroscopic quantities. It has been used e.g. by Sun and Hwang [1993]; Fischer and Tanaka [1992]; Patoor et al. [2006]. The main limitation of these models is that they lead to an important number of degrees of freedom, which generate high computation time, and they often define parameters that are not easy to identify.

- Macroscopic models are simpler to identify and to use for structure computations. However, multiaxial loading paths are not usually well predicted by these models, and they generally focus on the simulation of one particular behavior of the SMA.

Among the 1D models, Tanaka [1986] introduced three variables for the description of SMA behavior, which are the macroscopic strain, temperature and the volume fraction of martensite. The authors proposed an exponential evolution of the volume fraction of martensite with respect to the stress state and to temperature. The model by Liang and Rogers [1990] is somewhat similar, using a cosine law for the evolution of the martensite volume fraction. Subsequent work proposed enhancement of the initial model to account, e.g., for the detwinning of martensite responsible for the shape memory effect. Brinson and Huang [1996] separated the martensite volume fraction into a stress-induced and a temperature-induced fractions. Tanaka et al. [1995] extended Tanaka's model to account for cyclic behavior by introducing residual strain and stress fields.

Ivshin and Pence [1994] proposed a 1D Reuss model with three energy wells (two wells are associated with two variants of martensite and one well with austenite). A similar three-well model was proposed by Muller and Seelecke [2001], but it was based on statistical thermodynamics.

Abeyaratne et al. [1994] proposed a 1D model which introduces the maximum orientation strain as only internal variable.

A 3D model developed within the thermodynamic framework of Generalized Standard Materials was proposed by Frémond [2001] and extended in subsequent works. It introduces different variants of martensite and accounts for internal constraints using indicator functions.

Raniecki and Lexcelent [1998] developed a 3D model which was extended and improved upon in a number of later publications. The authors also used the martensite volume fraction as internal variable, introduced (in a subsequent work) an interaction energy between the phases and derived the evolution laws from yield functions.

Bo and Lagoudas [Bo and Lagoudas, 1999a; Lagoudas and Bo, 1999a; Bo and Lagoudas, 1999b; Lagoudas and Bo, 1999b] developed a 3D model accounting for most of the phenomena exhibited by SMAs, by introducing a volume fraction of martensite and an orientation strain tensor for martensite. A generalization of this model was proposed by Lagoudas and Entchev [2004] to account for plastic strain induced by training.

Using the same plasticity framework, Auricchio et al. [Auricchio et al., 2009; Auricchio and Petrini, 2002] developed several 1D and 3D models and extended their work to cyclic loading [Auricchio and Sacco, 2001].

Finally, Bekker and Brinson [1997, 1998] proposed a 1D model which was later extended to 3D. The model introduces the volume fraction of self-accommodated and oriented martensites, and their evolution laws are described from the state diagram of the SMA using "switching points". The loading path is partitioned into a series of arcs in stress-temperature space that are connected by "switching points".

A limited number of models account for the cyclic behavior of shape memory alloys. For [Abe-yaratne and Kim \[1997\]](#), the cyclic evolution of SMA response is explained by the generation of irreversible defects, promoting the formation of martensite. In their model, the thermodynamic force associated with martensite formation depends on the density of defects. The higher the density, the lower the stress threshold for the forward phase transformation. The model also introduces an asymptotic limit for the internal variables in order to reproduce the stabilization of the material response. The model is experimentally validated. [Lexcellent and Bourbon \[1996\]](#) introduced the cumulated fraction of martensite to account for the evolution of the hysteresis loop until stabilization. Finally, the model developed by [Tanaka et al. \[1995\]](#) accounts for cyclic evolution of the mechanical response, by introducing residual stress and strain.

We choose to work on the two models developed by [Zaki and Mounni \[2007a,b\]](#). Their models (monocycle model and cyclic model) are developed in the framework of Generalized Standard Materials and allow to simulate the different behaviors of SMAs with two internal variables and the associated yield criteria. These are 3D macroscopic models, which account for phase change and martensite reorientation, and are thus good candidates for use for structure calculations. The next section presents the detailed review of the two models.

## 2.2 REVIEW OF THE ZM MODELS

The Zaki-Mounni model for shape memory alloys is based on the theory developed by [Mounni \[1995\]](#). It was first introduced by [Zaki and Mounni \[2007a\]](#) and was later extended to account for cyclic SMA behavior and training [[Zaki and Mounni, 2007b](#)], low-cycle fatigue [[Mounni et al., 2009](#)] and plastic yield of martensite [[Zaki et al., 2010](#)]. The model is developed within the framework of Generalized Standard Materials with internal constraints [[Halphen and Nguyen, 1975](#); [Mounni et al., 2008](#)] in order to guarantee thermodynamic consistency. An overview of this framework is provided in Appendix B. The monocyclic model is presented in section 2.2.1 followed by the cyclic model (section 2.2.2).

### 2.2.1 Presentation of the model

This section summarizes the model developed in [[Zaki and Mounni, 2007a](#)].

#### *State variables and free energy*

The description of the SMA behavior is done using six internal variables:

- $\epsilon$ , the macroscopic strain tensor,
- $\epsilon_A$ , the local strain tensor of austenite,
- $\epsilon_M$ , the local strain tensor of martensite,
- $z$ , the volume fraction of martensite,
- $\epsilon_{ori}$ , the martensite orientation strain tensor,
- $T$ , the temperature.

The two-phase structure is modeled using a Reuss model, where austenite is assumed to behave elastically, while martensite can undergo orientation. Due to the choice of the state

variables, the thermodynamic potential is chosen as the Helmholtz free energy density, taken as the sum of the free energy density of each phase and of an interaction energy:

$$\begin{aligned} \mathcal{W} = \mathcal{W}(T, \epsilon_A, \epsilon_M, z, \epsilon_{\text{ori}}) = & (1-z) \left[ \frac{1}{2} \epsilon_A : \mathbf{K}_A : \epsilon_A \right] \\ & + z \left[ \frac{1}{2} (\epsilon_M - \epsilon_{\text{ori}}) : \mathbf{K}_M : (\epsilon_M - \epsilon_{\text{ori}}) + C(T) \right] \\ & + G \frac{z^2}{2} + \frac{z}{2} [\alpha z + \beta (1-z)] \left( \frac{2}{3} \epsilon_{\text{ori}} : \epsilon_{\text{ori}} \right). \end{aligned} \quad (2.1)$$

In the above expression,  $\mathbf{K}_A$  and  $\mathbf{K}_M$  are the elasticity tensors of austenite and martensite respectively.  $G$ ,  $\alpha$ , and  $\beta$  are material parameters that influence the size of the superelastic hysteresis loop and the slopes of the stress-strain curve during phase change and martensite orientation.  $C(T)$  is a heat density associated with phase change, which depends on temperature through the relation:

$$C(T) = \xi(T - A_f^0) + \kappa, \quad (2.2)$$

where  $\xi$  and  $\kappa$  are material parameters and  $A_f^0$  is the reverse phase change finish temperature under zero stress.  $\xi$  is related to the latent heat of phase change, since:

$$\xi = \frac{\partial \mathcal{W}}{\partial T \partial z}. \quad (2.3)$$

#### Internal constraints

The state variables obey the following physical constraints:

- The macroscopic strain tensor  $\epsilon$  is an average over the Representative Elementary Volume (REV) of the strains within austenite and martensite. By construction of the ZM model (Reuss model),  $\epsilon$  is given by

$$(1-z) \epsilon_A + z \epsilon_M - \epsilon = 0; \quad (2.4)$$

- $z$  is the volume fraction of martensite, restricted to the  $[0,1]$  interval;
- The equivalent orientation strain is limited by a maximum value  $\gamma$ :

$$\gamma - \sqrt{\frac{2}{3} \epsilon_{\text{ori}} : \epsilon_{\text{ori}}} \geq 0. \quad (2.5)$$

Because the above constraints are assumed to be perfect, they derive from the following constraints potential [cf. Mounni, 1995]:

$$\mathcal{W}_l = -\lambda : [(1-z) \epsilon_A + z \epsilon_M - \epsilon] - \mu \left( \gamma - \sqrt{\frac{2}{3} \epsilon_{\text{ori}} : \epsilon_{\text{ori}}} \right) - \nu_1 z - \nu_2 (1-z), \quad (2.6)$$

where  $\lambda$ ,  $\nu_1$ ,  $\nu_2$ , and  $\mu$  are Lagrange multipliers subjected to the Kuhn-Tucker conditions:

$$\begin{aligned} \nu_1 &\geq 0, \quad \nu_1 z = 0, \\ \nu_2 &\geq 0, \quad \nu_2 (1-z) = 0, \\ \text{and } \mu &\geq 0, \quad \mu \left( \gamma - \sqrt{\frac{2}{3} \epsilon_{\text{ori}} : \epsilon_{\text{ori}}} \right) = 0. \end{aligned} \quad (2.7)$$

### Lagrangian and derivation of the state laws

The sum of the Helmholtz energy density (2.1) and of the constraints potential (2.6) gives the Lagrangian

$$\mathcal{L} = \mathcal{W} + \mathcal{W}_l, \quad (2.8)$$

which is then used to derive the state equations:

$$\begin{aligned} \frac{\partial \mathcal{L}}{\partial \boldsymbol{\epsilon}} &= \boldsymbol{\sigma} & -\frac{\partial \mathcal{L}}{\partial z} &= \mathcal{A}_z \\ \frac{\partial \mathcal{L}}{\partial \boldsymbol{\epsilon}_A} &= 0 & -\frac{\partial \mathcal{L}}{\partial \boldsymbol{\epsilon}_{\text{ori}}} &= \mathcal{A}_{\text{ori}} \\ \frac{\partial \mathcal{L}}{\partial \boldsymbol{\epsilon}_M} &= 0 & \frac{\partial \mathcal{L}}{\partial \lambda} &= 0. \end{aligned} \quad (2.9)$$

From these state equations, the stress-strain relation is obtained:

$$\boldsymbol{\sigma} = \mathbf{K} : (\boldsymbol{\epsilon} - z\boldsymbol{\epsilon}_{\text{ori}}), \quad (2.10)$$

where  $\mathbf{K}$  is the equivalent elasticity tensor of the material, given by:

$$\mathbf{K} = \left( (1-z)\mathbf{K}_A^{-1} + z\mathbf{K}_M^{-1} \right)^{-1}. \quad (2.11)$$

### Pseudo-potential and complementary laws

The volume fraction of martensite and the orientation strain tensor are dissipative variables. Their evolution laws are derived from a pseudo-potential of dissipation  $\Psi$ :

$$\Psi = \Psi(z, \dot{z}, \dot{\boldsymbol{\epsilon}}_{\text{ori}}) = [a(1-z) + bz]|\dot{z}| + z^2 Y \sqrt{\frac{2}{3} \dot{\boldsymbol{\epsilon}}_{\text{ori}} : \dot{\boldsymbol{\epsilon}}_{\text{ori}}}, \quad (2.12)$$

where  $a^1$ ,  $b$ , and  $Y$  are positive material parameters. This expression of the pseudo-potential of dissipation satisfies the different properties listed in section B.2.

According to Eq. (B.12), the thermodynamic forces associated with  $z$  and  $\boldsymbol{\epsilon}_{\text{ori}}$  are sub-gradients of the pseudo-potential of dissipation  $\Psi$ .

$$\begin{aligned} \mathcal{A}_z &\in \partial_{\dot{z}} \Psi(z, \dot{z} = 0, \dot{\boldsymbol{\epsilon}}_{\text{ori}}), \\ \mathcal{A}_{\text{ori}} &\in \partial_{\dot{\boldsymbol{\epsilon}}_{\text{ori}}} \Psi(z, \dot{z}, \dot{\boldsymbol{\epsilon}}_{\text{ori}} = 0), \end{aligned} \quad (2.13)$$

which can be expressed as:

$$\begin{aligned} \forall \dot{z}, \Psi(z, \dot{z}, \dot{\boldsymbol{\epsilon}}_{\text{ori}}) - \Psi(z, 0, \dot{\boldsymbol{\epsilon}}_{\text{ori}}) &\geq \mathcal{A}_z(\dot{z} - 0), \\ \forall \dot{\boldsymbol{\epsilon}}_{\text{ori}}, \Psi(z, \dot{z}, \dot{\boldsymbol{\epsilon}}_{\text{ori}}) - \Psi(z, \dot{z}, \mathbf{0}) &\geq \mathcal{A}_{\text{ori}} : (\dot{\boldsymbol{\epsilon}}_{\text{ori}} - \mathbf{0}), \end{aligned} \quad (2.14)$$

From these relations, the yield functions for phase change and martensite orientation are obtained. Namely,

<sup>1</sup> Contrary to the expression given by Eq. (60) of [Zaki and Mourni, 2007a], we propose to determine  $\kappa$  as  $\kappa = a$ . Indeed, during the heating phase of the one-way shape memory effect, both the phase change criterion and the orientation criterion are equal to zero, leading to a decrease to zero of the orientation strain when  $z = 0$ . Thus  $C(A_f^0) = a$  in Eq. (59) of [Zaki and Mourni, 2007a]

- $\mathcal{F}_z^1$ , for forward phase change ( $\dot{z} \geq 0$ ),

$$\begin{aligned} \mathcal{F}_z^1 = & \frac{1}{3} \text{El}_{MA} \sigma_{VM}^2 + \frac{1}{2} \left( \frac{1}{3} \text{El}_{MA} + P_{MA} \right) (\text{tr } \sigma)^2 - C(T) + \sigma : \epsilon_{ori} \\ & - (G + b)z - a(1 - z) - \left[ (\alpha - \beta)z + \frac{\beta}{2} \right] \left( \frac{2}{3} \epsilon_{ori} : \epsilon_{ori} \right) \leq 0, \end{aligned} \quad (2.15)$$

- $\mathcal{F}_z^2$  for reverse phase change ( $\dot{z} \leq 0$ ),

$$\begin{aligned} \mathcal{F}_z^2 = & -\frac{1}{3} \text{El}_{MA} \sigma_{VM}^2 - \frac{1}{2} \left( \frac{1}{3} \text{El}_{MA} + P_{MA} \right) (\text{tr } \sigma)^2 + C(T) - \sigma : \epsilon_{ori} \\ & + (G - b)z - a(1 - z) + \left[ (\alpha - \beta)z + \frac{\beta}{2} \right] \left( \frac{2}{3} \epsilon_{ori} : \epsilon_{ori} \right) \leq 0, \end{aligned} \quad (2.16)$$

where  $\text{El}_{MA}$  and  $P_{MA}$  are related to the Young modulus of austenite and martensite as expressed in Table 1 in section 1.5.

- $\mathcal{F}_{ori}$  for martensite orientation,

$$\mathcal{F}_{ori} = \left\| \sigma - \frac{2}{3} [\alpha z + \beta (1 - z)] \epsilon_{ori} - \frac{\mu}{z} \frac{\partial}{\partial \epsilon_{ori}} \left( \sqrt{\frac{2}{3} \epsilon_{ori} : \epsilon_{ori}} \right) \right\|_{VM} - zY \leq 0. \quad (2.17)$$

The evolutions of state variables  $z$  and  $\epsilon_{ori}$  are governed by the complementary laws associated with the yield functions:

$$\begin{aligned} \mathcal{F}_z^1 & \leq 0, \dot{z} \geq 0, \mathcal{F}_z^1 \dot{z} = 0, \\ \mathcal{F}_z^2 & \leq 0, \dot{z} \leq 0, \mathcal{F}_z^2 \dot{z} = 0, \\ \dot{\epsilon}_{ori} & = \eta \frac{\partial \mathcal{F}_{ori}}{\partial \mathcal{A}_{ori}}, \mathcal{F}_{ori} \leq 0, \eta \geq 0, \mathcal{F}_{ori} \eta = 0. \end{aligned} \quad (2.18)$$

### 2.2.2 Extension to cyclic loading

The initial model was extended to account for training in [Zaki and Moumni, 2007b].

#### Introduction of new state variables

Experimental observations show an evolution of the hysteresis loop with the number of cycles up to stabilization (*cf.* Fig. 5).

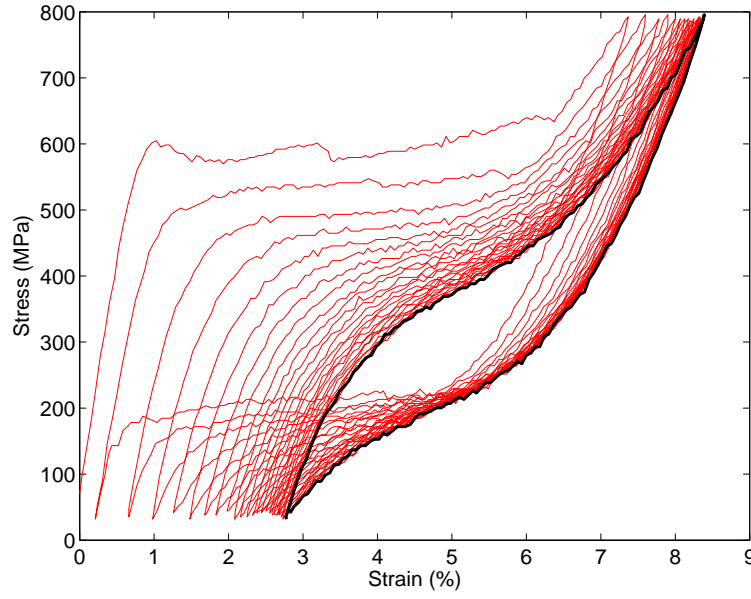


Figure 5. Cyclic stress-strain response.

To model this evolution, new state variables are introduced:

- A residual strain tensor  $\epsilon_r$ , to account for the appearance of residual strain during cycling,
- An internal stress tensor  $\mathbf{B}$ , which is created due to the incompatible residual strain,
- The cumulated fraction of martensite  $z_e$ , which allows to model the evolution of the hysteresis loop during cycling. It is defined by:

$$z_e = \int_0^t |\dot{z}| dt. \quad (2.19)$$

Almost all material parameters become function of this variable:

$$\forall f \in \{a, b, G, \xi, \kappa, \gamma\}, f = f^{(0)} + \left( f^{(\text{sat})} - f^{(0)} \right) \left( 1 - \exp \left( -\frac{z_e}{\tau} \right) \right), \quad (2.20)$$

where for all the above parameters,  $f^{(0)}$  and  $f^{(\text{sat})}$  correspond respectively to the value of the parameter for untrained SMA and for completely trained SMA.  $\tau$  is a time constant associated with the stabilization of the response. Moreover,  $\alpha$  and  $\beta$  depend on  $z_e$  through their dependence on  $\gamma$ :

$$\alpha = \frac{\sigma_{rf} - \sigma_{rs}}{\gamma}, \quad \beta = \frac{\sigma_{rf}}{\gamma}. \quad (2.21)$$

The previous state variables are still considered in this extended model.

### Change in the free energy and state laws

The Helmholtz free energies of each phase are modified to introduce the residual strain. In the free energy of martensite, an extra term is added, which corresponds to the creation of internal stress. This leads to:

$$\begin{aligned} \mathcal{W} = & (1-z) \left[ \frac{1}{2} (\epsilon_A - \epsilon_r) : \mathbf{K}_A : (\epsilon_A - \epsilon_r) \right] \\ & + z \left[ \frac{1}{2} (\epsilon_M - \epsilon_{\text{ori}} - \epsilon_r) : \mathbf{K}_M : (\epsilon_M - \epsilon_{\text{ori}} - \epsilon_r) + C(T) - \frac{2}{3} \mathbf{B} : \epsilon_{\text{ori}} \right] \\ & + G \frac{z^2}{2} + \frac{z}{2} [\alpha z + \beta (1-z)] \left( \frac{2}{3} \epsilon_{\text{ori}} : \epsilon_{\text{ori}} \right). \end{aligned} \quad (2.22)$$

No new internal constraint is added in the extended model. Thus, the potential associated with the internal constraints remains unchanged, except it is now a function of  $z_e$ . However, there are new state laws associated with the new state variables:

$$-\frac{\partial \mathcal{L}}{\partial \epsilon_r} = \mathcal{A}_r, \quad -\frac{\partial \mathcal{L}}{\partial \mathbf{B}} = \mathcal{A}_B, \quad -\frac{\partial \mathcal{L}}{\partial z_e} = \mathcal{A}_e, \quad (2.23)$$

where  $\mathcal{A}_r$ ,  $\mathcal{A}_B$  and  $\mathcal{A}_e$  are the thermodynamic forces associated with the variables  $\epsilon_r$ ,  $\mathbf{B}$  and  $z_e$  respectively. The stress-strain relation becomes:

$$\sigma = \mathbf{K} : (\epsilon - z \epsilon_{\text{ori}} - \epsilon_r), \quad (2.24)$$

where  $\mathbf{K}$  is still given by Eq. (2.11).

### Pseudo-potential and complementary laws

The new state variables are dissipative variables; it is thus necessary to define their evolution laws. To this end, empirical laws are proposed: they are not derived from a pseudo-potential but they fit the experimental observations:

- As the cumulated fraction of martensite is related to the volume fraction via Eq. (2.19), its evolution law follows the evolution of  $z$ :

$$\dot{z}_e = |\dot{z}|; \quad (2.25)$$

- From an experimental point of view, the residual strain increases exponentially with the number of cycles. This is modeled by the following empirical law:

$$\dot{\epsilon}_r = \frac{\epsilon_r^{\text{sat}}}{\tau} \left( \frac{3}{2} \frac{s}{\sigma_{VM}} \right) \exp(-z_e/\tau) \dot{z}_e; \quad (2.26)$$

- Finally, the evolution of the internal stress is given by:

$$\dot{\mathbf{B}} = \frac{B_{\text{sat}}}{\tau} \frac{\epsilon_{\text{ori}}}{\sqrt{\frac{2}{3} \epsilon_{\text{ori}} : \epsilon_{\text{ori}}}} \exp(-z_e/\tau) \dot{z}_e. \quad (2.27)$$

$B_{\text{sat}}$  and  $\epsilon_r^{\text{sat}}$  are positive scalars;  $\epsilon_r^{\text{sat}}$  represents the maximum residual strain in tension, associated with the stabilized superelastic loop. These empirical laws satisfy the second law of thermodynamics, since they lead to positive values of dissipation.

The evolution laws of  $z$  and  $\epsilon_{\text{ori}}$  are not modified and still derive from the pseudo-potential of dissipation, whose expression is unchanged, except the dependence on  $z_e$  of the material parameters  $a$  and  $b$ . Thus, the yield functions are modified, due to the changes in the free energy:

$$\mathcal{F}_z^1 = \left\{ \frac{1}{3} \text{El}_{\text{MA}} \sigma_{\text{VM}}^2 + \frac{1}{2} \left( \frac{1}{3} \text{El}_{\text{MA}} + P_{\text{MA}} \right) (\text{tr } \sigma)^2 - C(T, z_e) \right\} + \left( \sigma + \frac{2}{3} \mathbf{B} \right) : \epsilon_{\text{ori}} - (G + b)z - a(1 - z) - \left[ (\alpha - \beta)z + \frac{\beta}{2} \right] \left( \frac{2}{3} \epsilon_{\text{ori}} : \epsilon_{\text{ori}} \right), \quad (2.28)$$

$$\mathcal{F}_z^2 = - \left\{ \frac{1}{3} \text{El}_{\text{MA}} \sigma_{\text{VM}}^2 + \frac{1}{2} \left( \frac{1}{3} \text{El}_{\text{MA}} + P_{\text{MA}} \right) (\text{tr } \sigma)^2 - C(T, z_e) \right\} - \left( \sigma + \frac{2}{3} \mathbf{B} \right) : \epsilon_{\text{ori}} + (G - b)z - a(1 - z) + \left[ (\alpha - \beta)z + \frac{\beta}{2} \right] \left( \frac{2}{3} \epsilon_{\text{ori}} : \epsilon_{\text{ori}} \right), \quad (2.29)$$

$$\mathcal{F}_{\text{ori}} = \left\| \left( \sigma + \frac{2}{3} \mathbf{B} \right) - \frac{2}{3} [\alpha z + \beta(1 - z)] \epsilon_{\text{ori}} - \frac{2\mu}{3z} \frac{\epsilon_{\text{ori}}}{\sqrt{\frac{2}{3} \epsilon_{\text{ori}} : \epsilon_{\text{ori}}}} \right\|_{\text{VM}} - zY. \quad (2.30)$$

The complementary laws remain unchanged.

This completes the presentation of the ZM models.

## 2.3 ANALYTICAL SOLUTION IN TORSION

In this section, we propose an analytical resolution of an SMA cylinder structure subject to torsion loading. This solution will be used in order to validate the numerical algorithm developed in section 2.4. First, the problem and the main assumptions are presented. Second, the different steps of the resolution during loading are detailed: elastic solution, transformation radii and stress-strain relation in the transformation plateau. For the unloading path, only the differences with the loading solution are given. Finally, the results are discussed.

### 2.3.1 Position of the problem and main hypotheses

A cylindrical shaft, oriented as shown on Fig. 6, with radius  $R_e$  and height  $h$ , is acted upon at its ends by an imposed torsional displacement (maximum twist angle:  $\phi_{\text{max}}$ ). The lateral surface of the shaft is stress free. All plane cross sections normal to the  $z$ -axis remain plane, and the deformation consists of relative rotation of the cross sections. A set of cylindrical coordinates  $(\mathbf{e}_r, \mathbf{e}_\theta, \mathbf{e}_z)$  is used. The boundary conditions of the problem are:

$$\begin{aligned} \text{on } z = 0 : \xi_r &= \xi_\theta = 0, T_z = 0, \\ \text{on } z = h : \xi_r &= 0, \xi_\theta = \phi r, T_z = 0, \\ \text{on } r = R_e : \mathbf{T} &= 0, \end{aligned} \quad (2.31)$$

where  $\mathbf{T}$  is the imposed force on a given surface,  $T_z$  is the component of the imposed force along the  $z$ -axis, and  $\xi = (\xi_r, \xi_\theta, \xi_z)$  is the displacement vector. The elastic solution to the problem is

obtained under the assumption of small perturbations<sup>2</sup>, implying that  $\frac{\phi r z}{h} \ll 1$  and  $\frac{\phi r}{h} \ll 1$ . No warp of the cross sections is assumed.

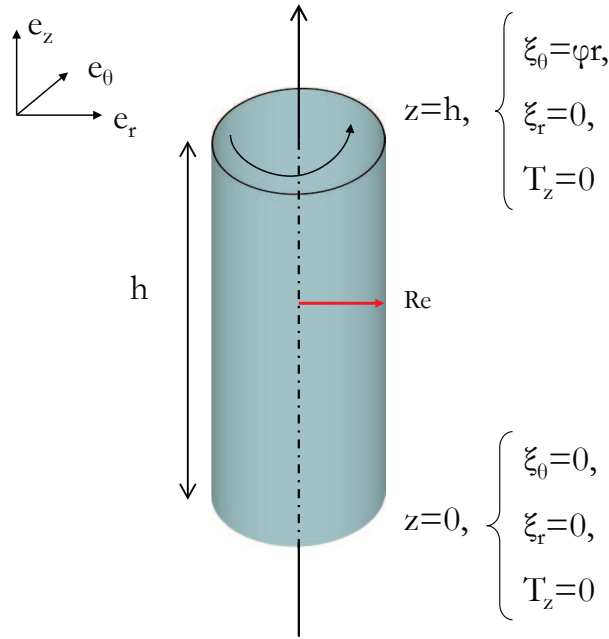


Figure 6. Position of the problem

### 2.3.2 Stress-strain response

#### *Elastic solution during loading*

Because of the symmetry of the problem, only one component of the stress and strain fields is not vanishing:

$$\epsilon = \epsilon_{\theta z} (\mathbf{e}_\theta \otimes \mathbf{e}_z + \mathbf{e}_z \otimes \mathbf{e}_\theta), \quad (2.32)$$

$$\sigma = \sigma_{\theta z} (\mathbf{e}_\theta \otimes \mathbf{e}_z + \mathbf{e}_z \otimes \mathbf{e}_\theta), \quad (2.33)$$

and only depend on  $r$ . This is in agreement with the equilibrium equation  $\text{div } \sigma = 0$ , and satisfies the boundary conditions (2.31). The elastic strain and stress fields are given by:

$$\epsilon = \frac{\phi r}{2h} (\mathbf{e}_\theta \otimes \mathbf{e}_z + \mathbf{e}_z \otimes \mathbf{e}_\theta), \quad (2.34)$$

$$\sigma = \frac{\mu_A \phi r}{h} (\mathbf{e}_\theta \otimes \mathbf{e}_z + \mathbf{e}_z \otimes \mathbf{e}_\theta); \quad (2.35)$$

$\mu_A$  is the austenitic shear modulus. This solution holds until the yield function for direct phase change is equal to zero. The transformation strain is taken as<sup>3</sup>

$$\epsilon_{\text{ori}} = \frac{\sqrt{3}}{2} \gamma (\mathbf{e}_\theta \otimes \mathbf{e}_z + \mathbf{e}_z \otimes \mathbf{e}_\theta). \quad (2.36)$$

<sup>2</sup> Small perturbation = small displacement and small strain

<sup>3</sup> This expression originates in the nullity of the orientation yield function. More details are given in the next section 2.4.2.

Considering the expression of the stress field, simplified expressions of the phase change criteria are used, which only depend on  $\sigma_{\theta z}$  and on  $z$ .

$$\mathcal{F}_z^1 = \text{El}_{MA} \sigma_{\theta z}^2 - C + \sqrt{3} \sigma_{\theta z} \gamma - (G + b) z - a(1 - z) - \left[ (\alpha - \beta) z + \frac{\beta}{2} \right] \gamma^2, \quad (2.37)$$

$$\mathcal{F}_z^2 = -\text{El}_{MA} \sigma_{\theta z}^2 + C - \sqrt{3} \sigma_{\theta z} \gamma + (G - b) z - a(1 - z) + \left[ (\alpha - \beta) z + \frac{\beta}{2} \right] \gamma^2. \quad (2.38)$$

#### Direct transformation radii

Given the expressions of the stress and strain fields, the transformation front propagates from the outer surface to the center of the cylinder, dividing the cylinder into three zones for sufficiently high rotation angle: the outer ring corresponds to fully martensitic material, the inner zone to fully austenitic material and the middle one to the transformation zone. The limits of these zones are determined by the nullity of the phase change criterion, assuming that the solution remains elastic at the boundary of an elastic zone (*cf.* Fig. 7). For a given angle  $\phi$ , the direct

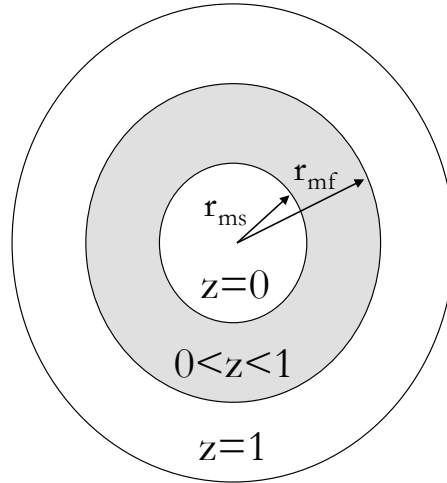


Figure 7. Definition of the direct transformation radii

transformation begins at a radius  $r_{ms}$  such that  $\mathcal{F}_z^1(z = 0) = 0$ ,

$$r_{ms} = \frac{-\sqrt{3}\gamma + \sqrt{3\gamma^2 + 4\text{El}_{MA} \left( C + a + \frac{\beta}{2} \gamma^2 \right)}}{2\mu_A \text{El}_{MA}} \frac{h}{\phi}, \quad (2.39)$$

The direct transformation ends at  $r_{mf}$  such that  $\mathcal{F}_z^1(z = 1) = 0$ ,

$$r_{mf} = \frac{-\sqrt{3}\gamma + \sqrt{3\gamma^2 + 4\text{El}_{MA} \left( C + G + b + \left( \alpha - \frac{\beta}{2} \right) \gamma^2 \right)}}{2\mu_M \text{El}_{MA}} \frac{h}{\phi}. \quad (2.40)$$

A fully martensitic zone (*i.e.*  $r \geq r_{mf}$  radius) exists either for high rotation angle or for high external radius of the cylinder.

*Solution in the direct transformation zone*

In the transformation zone, the elastic expression of the strain field (2.34) holds, and the stress field is still assumed to have only one non vanishing component (cf. Eq. (2.32)). As shown by Suquet [2008], these expressions of the fields satisfy the equilibrium equation and the different boundary conditions. In the direct transformation zone, stress, strain and volume fraction of martensite are related through two equations:

- the stress-strain relation

$$\sigma_{\theta z} = 2\mu_{eq} \left( \epsilon_{\theta z} - \frac{\sqrt{3}z\gamma}{2} \right) \quad (2.41)$$

with  $\mu_{eq} = \frac{1}{2(1+\nu)} \left( \frac{1-z}{E_A} + \frac{z}{E_M} \right)^{-1}$ ;

- the nullity of the phase change criterion  $\mathcal{F}_z^1$ , for  $z$  in  $[0, 1]$  leads to:

$$z = \frac{El_{MA} \sigma_{\theta z}^2 + \sqrt{3}\gamma \sigma_{\theta z} - C - a - \frac{\beta}{2}\gamma^2}{G + b - a + (\alpha - \beta)\gamma^2}. \quad (2.42)$$

The combination of these two equations gives a polynomial equation of degree three for  $\sigma_{\theta z}$ .

$$\begin{aligned} & \frac{El_{MA}^2}{D} \sigma_{\theta z}^3 + \frac{3\sqrt{3}El_{MA}\gamma}{2} \sigma_{\theta z}^2 + \left[ El_A - \frac{El_{MA}}{D} \left( C + a + \frac{\beta}{2}\gamma^2 \right) + \frac{3}{2} \frac{\gamma^2}{D} \right] \sigma_{\theta z} \\ & - \frac{\sqrt{3}}{2} \frac{C + a + \frac{\beta}{2}\gamma^2}{D} \gamma = \epsilon_{\theta z}, \end{aligned} \quad (2.43)$$

with

$$D = G + b - a + (\alpha - \beta)\gamma^2. \quad (2.44)$$

The positive root of Eq. (2.42) for  $z = 0$  gives the yield stress for beginning of the direct phase change  $\sigma_{ms}$  and the positive root of Eq. (2.42) for  $z = 1$  gives the finish stress of the direct phase change  $\sigma_{mf}$ :

$$\begin{aligned} \sigma_{ms} &= \frac{-\sqrt{3}\gamma + \sqrt{3\gamma^2 + 4El_{MA}(C + a + \frac{\beta}{2}\gamma^2)}}{2El_{MA}}, \\ \sigma_{mf} &= \frac{-\sqrt{3}\gamma + \sqrt{3\gamma^2 + 4El_{MA}(C + G + b + (\alpha - \frac{\beta}{2})\gamma^2)}}{2El_{MA}}. \end{aligned} \quad (2.45)$$

Consequently, on the direct phase change plateau, the stress belongs to the interval:

$$\sigma_{\theta z} \in [\sigma_{ms}, \sigma_{mf}]. \quad (2.46)$$

The stress-strain relation in the transformation zone is given by the inversion of Eq. (2.43). Among the three solutions, only one belongs to the interval (2.46). When the volume fraction of martensite is equal to 1 (fully martensitic material), the response is elastic:

$$\sigma = 2\mu_M (\epsilon - \epsilon_{ori}) \quad (2.47)$$

where  $\epsilon$  and  $\epsilon_{ori}$  are given by Eq. (2.34) and Eq. (2.36) respectively and  $\mu_M$  is the shear modulus of martensite.

In summary, the solution during loading is:

$$\xi(r) = \frac{\phi r z}{h} \mathbf{e}_\theta, \quad \forall r \in [0, R_e], \quad (2.48)$$

$$\epsilon(r) = \frac{\phi r}{2h} (\mathbf{e}_\theta \otimes \mathbf{e}_z + \mathbf{e}_z \otimes \mathbf{e}_\theta) \quad \forall r \in [0, R_e], \quad (2.49)$$

$$\sigma(r) = \frac{\mu_A \phi r}{h} (\mathbf{e}_\theta \otimes \mathbf{e}_z + \mathbf{e}_z \otimes \mathbf{e}_\theta), \quad z = 0, \quad \text{for } r \leq r_{ms}, \quad (2.50)$$

$$\sigma(r) = \left( \frac{\mu_M \phi r}{h} - 3\mu_M \gamma \right) (\mathbf{e}_\theta \otimes \mathbf{e}_z + \mathbf{e}_z \otimes \mathbf{e}_\theta), \quad z = 1, \quad \text{for } r \geq r_{mf}. \quad (2.51)$$

For  $0 \leq z \leq 1$ ,  $\sigma_{\theta z}$  is given by Eq. (2.43), and  $z$  by Eq. (2.42).

### Unloading

The twist angle reached at the end of the loading is  $\phi_{max}$ ; for an unloading angle  $\phi_d$ , the displacement and strain fields are given by

$$\xi_d(r) = \frac{r z}{h} (\phi_{max} - \phi_d) \mathbf{e}_\theta, \quad \forall r \in [0, R_e], \quad (2.52)$$

$$\epsilon_d(r) = \frac{r}{2h} (\phi_{max} - \phi_d) (\mathbf{e}_\theta \otimes \mathbf{e}_z + \mathbf{e}_z \otimes \mathbf{e}_\theta) \quad \forall r \in [0, R_e]. \quad (2.53)$$

To get the stress field, it is necessary to determine whether the reverse transformation takes place or not for a given  $\phi_d$ . The nullity of the reverse phase change criterion  $\mathcal{F}_z^2$  leads to equations similar to Eqs. (2.42, 2.43); this allows the determination of hypothetical volume fraction of martensite and stress field. Special attention must be paid: at the beginning of the unloading, this hypothetical volume fraction, solution of  $\mathcal{F}_z^2 = 0$ , may be higher than the volume fraction calculated at the end of the loading  $z_{max}(r)$ . This is because the beginning of the unloading is elastic. Thus, as long as the volume fraction obtained as the solution of  $\mathcal{F}_z^2 = 0$  is higher than the volume fraction calculated at the end of the loading for a given point  $r$ , the solution is elastic, and the stress is given by:

$$\sigma_d(r) = \sigma_{max}(r) - 2\mu(z_{max}(r)) \epsilon_d(r). \quad (2.54)$$

This holds as long as

$$\mathcal{F}_z^2(\sigma_d(r), z_{max}(r)) < 0. \quad (2.55)$$

When the value of the stress is such that the phase change criterion becomes equal to zero for  $z = z_{max}(r)$ , this signifies that the computed volume fraction is equal to  $z_{max}(r)$  and thus the reverse phase change begins at this point. The calculated volume fraction becomes then lower than the volume fraction reached at the end of the loading, and a similar system of equations as Eqs. (2.42, 2.43) is solved to obtain the stress field.

### 2.3.3 Results

The equations are solved with a numerical solver. The parameters are given in Table 2. Results are first given for the same values of Young modulus for austenite and martensite,  $E_A = E_M = 24000$  MPa (cf. Fig. 8 and 9). As expected, during loading, the transformation front begins at the outer radius of the cylinder and propagates towards the center. The unloading curves

show non monotonic evolution of the stress along a radius. Indeed, Eq. (2.54) shows that, for constant elastic moduli, the stress decrease is proportional to the radius value  $r$ , through the strain decrease:  $\sigma_d(r) = \sigma_{\max}(r) - 2\mu\epsilon_d(r)$ . The stress decrease is larger at the outer surface. For the points with biphasic microstructure, the slope of the stress decrease is higher than the slope of the plateau, leading to a negative slope of stress versus  $r$ . Similarly, for large unloading angles  $\phi_d$ , a negative slope is observed between the fully austenitic response and the phase change plateau. Indeed, at these points, the stress decrease is too small to reach the yield stress to induce reverse phase change at this unloading angle. The reverse phase change front also propagates from the outer surface  $r = R_e$  towards the center. The stress-strain curves for different radii are given on Fig. 9.

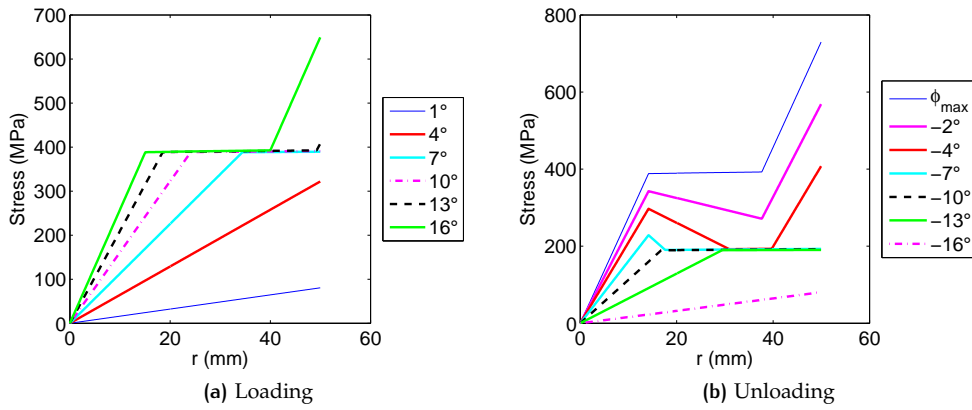


**Figure 8.** Evolution of the stress field in the cross section of the cylinder: (a) for different loading angles and (b) for different unloading angles.  $\phi_{\max} = 17^\circ$ . In these figures,  $E_A = E_M = 24000$  MPa.

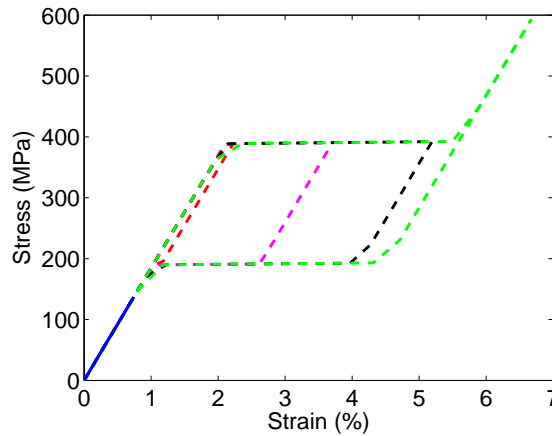


**Figure 9.** Stress-strain response at different radii:  $r=5$  mm (blue), 15 mm (red), 25 mm (magenta), 35 mm (black), 45 mm (green). In this figure,  $E_A = E_M = 24000$  MPa.

In the case where the two phases have different Young moduli, the tendencies are identical, except that during reverse phase change both radius and Young modulus changes cause the negative slope of the stress vs. radius curve (*cf.* Figs. 10 and 11).

Parameters values			
$E_A$	61500 MPa	$\alpha$	6.8920 MPa
$E_M$	24000 MPa	$b$	6.9091 MPa
$\nu$	0.3	$G$	4.6556 MPa
$\alpha$	2750 MPa	$\beta$	5500 MPa
$\gamma$	110 MPa	$A_f^0$	40 °C
$\xi$	0.2914 MPa/°C	$\kappa$	6.8920 MPa
$\gamma$	4.0 %	$\phi_{\max}$	17 °
$R_e$	50 mm	$h$	100 mm

Table 2. Model parameters

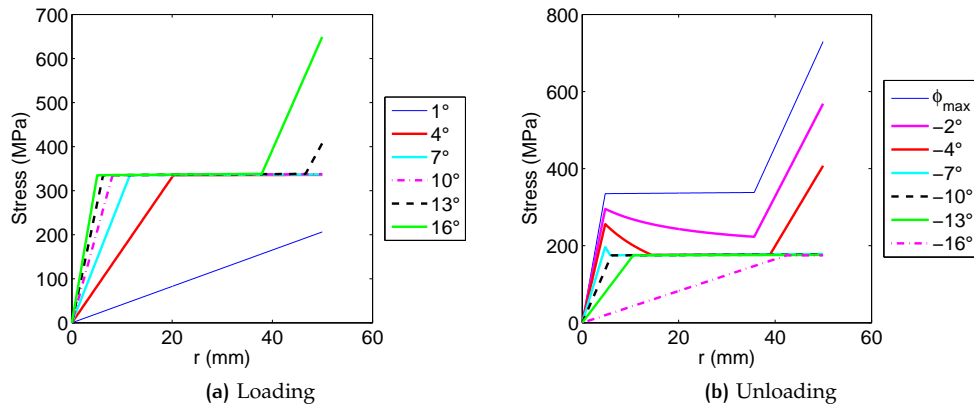


Figure 10. Evolution of the stress field in the cross section of the cylinder: (a) for different loading angles, and (b) for different unloading angles.  $\phi_{\max} = 17^\circ$ . In these figures,  $E_A = 61500$  MPa and  $E_M = 24000$  MPa.

### 2.3.4 Evolution of the response in the section and torque-angle response

During torsion experiments, measurements give the torque and the angle to which the structure is subject. For our problem, the torque is given by:

$$M = \int_{\theta=0}^{2\pi} \int_{r=0}^{R_e} \sigma_{\theta z} r^2 dr d\theta = 2\pi \int_{r=0}^{R_e} \sigma_{\theta z}(r) r^2 dr. \quad (2.56)$$

A typical torque-angle response given by the ZM model is shown in Fig. 12. The curve presents three different responses : the first part is the elastic response of the austenite phase. The second part is the phase change plateau. Contrary to tensile curve, the beginning of the plateau is gradual, because of the non homogeneous stress state of the cross section. The last part of the curve begins when the outer radius is fully martensitic. The slope of the curve still evolves due to the propagation of the end of the phase front. During unloading, the slope of the first unloading part is equal to the slope of the beginning of the loading part (for equal Young moduli for both phases): the unloading is first elastic for the whole cylinder. This corresponds to the linear part of the torque-angle unloading response. The reverse transformation starts at the external radius of the cylinder and propagates to the center.

## 2.4 NUMERICAL RESOLUTION: RETURN MAPPING ALGORITHM

The non-linear behavior of SMA structures requires the development of a specific algorithm to compute the pseudoelastic response of the structure. This is the aim of this section.

### 2.4.1 Position of the problem

The problem consists of determining the stabilized response of a superelastic shape memory alloy structure occupying a volume  $\Omega$  assuming infinitesimal transformations and isothermal, quasistatic possibly cyclic loading over a time interval  $[0, T]$ . The structure is subject to a distribution of body forces  $\mathbf{f}(\mathbf{x}, t)$  over  $\Omega \times [0, T]$  and contact forces  $\mathbf{T}^d(\mathbf{x}, t)$  over part of the boundary  $\partial\Omega_T$ ; the remaining part  $\partial\Omega_\xi$  is subject to an imposed displacement field  $\xi^d(\mathbf{x}, t)$ .

The problem consists of the following equations:

- Static and kinematic admissibility

$$\operatorname{div} \boldsymbol{\sigma} + \mathbf{f} = \mathbf{0} \text{ in } \Omega, \quad (2.57)$$

$$\xi = \xi^d \text{ in } \partial\Omega_\xi, \quad (2.58)$$

$$\boldsymbol{\sigma} \cdot \mathbf{n} = \mathbf{T}^d \text{ in } \partial\Omega_T. \quad (2.59)$$

- Strain compatibility

$$\boldsymbol{\epsilon} = \frac{1}{2} (\nabla \xi + {}^t \nabla \xi) \text{ in } \Omega. \quad (2.60)$$

- Constitutive equations

$$\boldsymbol{\sigma} = \mathbf{K} : (\boldsymbol{\epsilon} - z \boldsymbol{\epsilon}_{\text{ori}}), \text{ or, for cyclic loadings, } \boldsymbol{\sigma} = \mathbf{K} : (\boldsymbol{\epsilon} - z \boldsymbol{\epsilon}_{\text{ori}} - \boldsymbol{\epsilon}_r). \quad (2.61)$$

where the evolution laws of  $z$  and  $\boldsymbol{\epsilon}_{\text{ori}}$  are governed by the yield functions  $\mathcal{F}_z^1$ ,  $\mathcal{F}_z^2$  and  $\mathcal{F}_{\text{ori}}$  (cf. Eqs. (2.15)-(2.17) or, for cyclic loadings, (2.28)-(2.30)) and by the verification of the Kuhn-Tucker conditions (cf. Eqs. (2.18)).

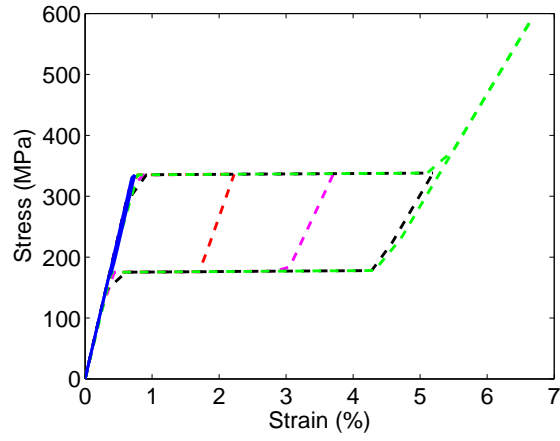


Figure 11. Stress-strain response at different radii:  $r=5$  mm (blue), 15 mm (red), 25 mm (magenta), 35 mm (black), 45 mm (green). In this figure,  $E_A = 61500$  MPa and  $E_M = 24000$  MPa.

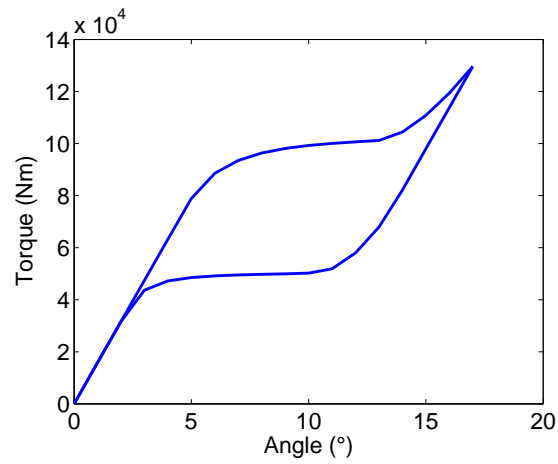


Figure 12. Torque-angle curve. In this figure,  $E_A = E_M = 24000$  MPa.

### 2.4.2 Presentation of the return mapping algorithm

#### *Simplification to the case of proportional loadings*

Restricting the discussion to the case of proportional loadings in pseudoelasticity, the stress tensor  $\sigma$  in any Representative Elementary Volume of the SMA can be written in terms of a scalar variable  $t$  as

$$\sigma = t\sigma_0, \quad (2.62)$$

where  $\sigma_0$  is a constant tensor defining the direction of the state of stress in  $\mathbb{R}^6$  while  $t$  determines its algebraic magnitude. Likewise, the orientation strain tensor  $\epsilon_{\text{ori}}$  maintains a constant direction in the deviatoric strain space, which can easily be shown to be parallel to that of the stress deviator  $s$ : writing the orientation yield function  $\mathcal{F}_{\text{ori}}$  for  $z = 0^+$  and considering that the Lagrange multiplier  $\mu$  remains equal to zero for  $z = 0^+$  gives

$$\left\| t\sigma_0 - \frac{2\beta}{3}\epsilon_{\text{ori}} \right\|_{\text{VM}} \leq 0, \quad (2.63)$$

which cannot hold unless  $\epsilon_{\text{ori}}$  is proportional to the stress deviator. If one further assumes that the orientation finish stress is lower than the critical stress for forward phase change (*i.e.* that  $\sigma_{\text{rf}} < \sigma_{\text{ms}}$ ), the created martensite is completely oriented for any value of  $z$ . This is in accord with the properties of SMA reported by [Patoor et al. \[2006\]](#).  $\epsilon_{\text{ori}}$  can be written in this case as

$$\epsilon_{\text{ori}} = \gamma\epsilon_0, \quad (2.64)$$

where  $\epsilon_0$  is a constant deviatoric tensor proportional to  $s$  and satisfying

$$\sqrt{\frac{2}{3}}\epsilon_0 : \epsilon_0 = 1. \quad (2.65)$$

The simplified form given in (2.64) can be used to readily determine  $\epsilon_{\text{ori}}$ , bypassing the need for the yield function  $\mathcal{F}_{\text{ori}}$  and for the associated consistency conditions.

Under the above assumptions, the stress-strain relation can be written as

$$\sigma = \mathbf{K} : (\epsilon - z\gamma\epsilon_0). \quad (2.66)$$

In the following, the elasticity tensor  $\mathbf{K}$  or the compliance tensor  $\mathbf{S} = \mathbf{K}^{-1}$  are equally used.

#### *Algorithm for proportional loadings*

The loading history is divided into  $N$  intervals over which the mechanical problem is solved incrementally, using a return mapping algorithm. Assuming the solution is known for load increment  $n$  ( $n \geq 0$ ), the solution at increment  $n + 1$  is determined iteratively. In the equations below, the increment number is written as a subscript and the iteration number  $k$  as a superscript enclosed in parentheses.

The algorithm involves two steps:

- First, the equilibrium equations (Eqs. (2.57)-(2.60)) are solved assuming the SMA to be elastic (*i.e.* maintaining the internal variables constant). This is the so-called predictor step. The following discrete form of the stress-strain relation is used in this step:

$$\sigma_{n+1}^{(0)} = \mathbf{S}_{n+1}^{(0),-1} : \left( \epsilon_{n+1} - z_{n+1}^{(0)}\gamma\epsilon_0 \right) \text{ with } z_{n+1}^{(0)} = z_n. \quad (2.67)$$

- The yield functions are computed with the new stress field  $\sigma_{n+1}^{(k)}$  and the unchanged values of the internal variables. If they are positive, a corrector step is introduced to enforce consistency with the constitutive equations.

- If  $\mathcal{F}$  is a yield function governing phase change ( $\mathcal{F} = \{\mathcal{F}_z^1, \mathcal{F}_z^2\}$ ), the associated consistency condition  $\mathcal{F}_{n+1}^{(k)} = 0$  can be written in discrete form as follows:

$$\mathcal{F}_{n+1}^{(k-1)} + \partial_{\sigma} \mathcal{F}_{n+1}^{(k-1)} : \Delta \sigma_{n+1}^{(k)} + \partial_z \mathcal{F}_{n+1}^{(k-1)} \Delta z_{n+1}^{(k)} = 0, \quad (2.68)$$

where  $\Delta a_{n+1}^{(k)} = a_{n+1}^{(k)} - a_{n+1}^{(k-1)}$  for any variable  $a$  to be incremented.

- Similarly, the stress-strain relation can be written in discrete incremental form as

$$\Delta \sigma_{n+1}^{(k)} = \mathbf{S}_{n+1}^{(k-1), -1} : \left[ \Delta \epsilon_{n+1}^{(k)} - \left( \Delta \mathbf{S}_{n+1}^{(k)} : \sigma_{n+1}^{(k-1)} + \Delta z_{n+1}^{(k)} \gamma \epsilon_0 \right) \right], \quad (2.69)$$

where  $\Delta \epsilon_{n+1}^{(k)} = 0$  ( $\epsilon$  is not updated in the corrector step) and the increment of the elastic compliance tensor is given by (cf. Eq. (2.11))

$$\Delta \mathbf{S}_{n+1}^{(k)} = (\mathbf{S}_M - \mathbf{S}_A) \Delta z_{n+1}^{(k)}. \quad (2.70)$$

Eq. (2.69) becomes

$$\Delta \sigma_{n+1}^{(k)} = -\mathbf{S}_{n+1}^{(k-1), -1} : \mathbf{R}_{1,n+1}^{(k-1)} \Delta z_{n+1}^{(k)}, \quad (2.71)$$

with

$$\mathbf{R}_{1,n+1}^{(k-1)} = (\mathbf{S}_M - \mathbf{S}_A) : \sigma_{n+1}^{(k-1)} + \gamma \epsilon_0. \quad (2.72)$$

The increment of the martensite volume fraction is then calculated as

$$\Delta z_{n+1}^{(k)} = - \frac{\mathcal{F}_{n+1}^{(k-1)}}{-\partial_{\sigma} \mathcal{F}_{n+1}^{(k-1)} : \mathbf{S}_{n+1}^{-1, (k-1)} : \mathbf{R}_{1,n+1}^{(k-1)} + \partial_z \mathcal{F}_{n+1}^{(k-1)}}. \quad (2.73)$$

The corrector step is repeated until consistency is achieved with the constitutive equations. The algorithm is then repeated until a solution is reached that fulfills both equilibrium and consistency conditions. The algorithm is summarized in Table 3. In this algorithm,  $\mathbf{F}_{n+1}$  is the loading applied on the structure at the instant  $t_{n+1}$ , and  $\|\cdot\|$  is for instance the maximum norm over the second order tensor space.

#### Extension to proportional cyclic loadings

The restriction to proportional loadings of the ZM cyclic model leads to the same simplifications for the stress-strain relation:

$$\sigma = \mathbf{S}^{-1} : (\epsilon - z\gamma\epsilon_0 - \epsilon_r), \quad (2.74)$$

where  $\epsilon_0$  is proportional to the stress deviator  $s$  and verifies Eq. (2.65);  $\gamma$  now depends on  $z_e$ . The algorithm is similar except that all parameters must be derived with respect to  $z_e$ . The return mapping algorithm for the cyclic model is given in Table 4.

---

Input: model parameters,  $\sigma_n, z_n, F_{n+1}$ , two tolerances:  $\text{tol}_1, \text{tol}_2$ .

Output:  $\epsilon_{n+1}, \sigma_{n+1}, z_{n+1}$ .

Set  $k = 0, z_{n+1}^{(0)} = z_n, S_{n+1}^{(0)} = S_n$ .

1. Compute the displacement field by solving the equilibrium equation:

$$\mathbf{K}(z_{n+1}^{(k)}) \cdot \mathbf{U}_{n+1}^{(k)} = F_{n+1}.$$

2. Compute the strain field:

$$\epsilon_{n+1}^{(k)} = \frac{1}{2} \left( \nabla \mathbf{U}_{n+1}^{(k)} + {}^t \nabla \mathbf{U}_{n+1}^{(k)} \right).$$

3. Thermoelastic prediction and return mapping algorithm:

- a) Compute the thermoelastic prediction (Eq. (2.67)) and evaluate the yield functions

$$(i = 1, 2): \mathcal{F}_{z,n+1}^{i,(k)} = \mathcal{F}_z^i(\sigma_{n+1}^{(k)}, z_{n+1}^{(k)}).$$

- b) If  $\mathcal{F}_{z,n+1}^{i,(k)} < 0$  (or during the iterations  $|\mathcal{F}_{z,n+1}^{i,(k)}| < \text{tol}_1$ ) then set  $k = k + 1$  and go to 4.

- c) Else, compute the increment of the martensite volume fraction  $\Delta z_{n+1}^{(k+1)}$  (Eq. (2.73)).

- d) Update the state variables  $\sigma_{n+1}^{(k)}, z_{n+1}^{(k)}$ .

- e) Set  $k = k + 1$  and go to 3.

4. Compute the residual:  $\mathbf{R} = \mathbf{K}(z_{n+1}^{(k+1)}) \cdot \mathbf{U}_{n+1}^{(k+1)} - F_{n+1}$

5. If  $\|\mathbf{R}\| > \text{tol}_2$  then go to 1., else end.
- 

Table 3. Return mapping algorithm for proportional loadings.

- Input: model parameters,  $z_n, z_{e,n}, \mathbf{B}_n, \boldsymbol{\epsilon}_{r,n}, \Delta\boldsymbol{\epsilon}_{n+1}$ .
- Output:  $\boldsymbol{\sigma}_{n+1}, z_{n+1}, z_{e,n+1}, \mathbf{B}_{n+1}, \boldsymbol{\epsilon}_{r,n+1}$ , updated model parameters and elastic properties.

1. Set  $k = 0$ ,

$$\boldsymbol{\epsilon}_{n+1} = \boldsymbol{\epsilon}_n + \Delta\boldsymbol{\epsilon}_{n+1}, z_{n+1}^{(k)} = z_n, z_{e,n+1}^{(k)} = z_{e,n},$$

$$\mathbf{B}_{n+1}^{(k)} = \mathbf{B}_n, \boldsymbol{\epsilon}_{r,n+1}^{(k)} = \boldsymbol{\epsilon}_{r,n}, \mathbf{S}_{n+1}^{(k)} = \mathbf{S}_n.$$

2. Calculate a thermoelastic prediction :

$$\boldsymbol{\sigma}_{n+1}^{(k)} = \mathbf{S}_{n+1}^{(k),-1} : \left( \boldsymbol{\epsilon}_{n+1} - z_{n+1}^{(k)} \boldsymbol{\epsilon}_{\text{ori},n+1}^{(k)} - \boldsymbol{\epsilon}_{r,n+1}^{(k)} \right)$$

$$\text{where } \mathbf{S}_{n+1}^{(k)} \text{ is the compliance tensor given by } \mathbf{S}_{n+1}^{(k)} = \left( 1 - z_{n+1}^{(k)} \right) \mathbf{S}_A + z_{n+1}^{(k)} \mathbf{S}_M$$

and evaluate the yield functions :

$$\mathcal{F}_z^1 \left( \boldsymbol{\sigma}_{n+1}^{(k)}, z_{n+1}^{(k)}, \mathbf{B}_{n+1}^{(k)}, z_{e,n+1}^{(k)} \right),$$

$$\mathcal{F}_z^2 \left( \boldsymbol{\sigma}_{n+1}^{(k)}, z_{n+1}^{(k)}, \mathbf{B}_{n+1}^{(k)}, z_{e,n+1}^{(k)} \right).$$

If  $\mathcal{F}_{z,n+1}^{1,(k)} \leq 0$  (or during the iterations  $|\mathcal{F}_{z,n+1}^{1,(k)}| < \text{tolerance}$ ) (loading), or  $\mathcal{F}_{z,n+1}^{2,(k)} \leq 0$  (or during the iterations  $|\mathcal{F}_{z,n+1}^{2,(k)}| < \text{tolerance}$ ) (unloading) then exit.

3. Else, compute the increment of the martensite volume fraction. For example, during direct phase change, the following equation must be solved:

$$0 = \mathcal{F}_{z,n+1}^{1,(k-1)} + \left[ -\partial_{\boldsymbol{\sigma}} \mathcal{F}_{z,n+1}^{1,(k-1)} : \mathbf{S}_{n+1}^{-1,(k-1)} : \mathbf{R}_{1,n+1}^{(k-1)} + \partial_z \mathcal{F}_{z,n+1}^{1,(k-1)} + \partial_{z_e} \mathcal{F}_{z,n+1}^{1,(k-1)} \right] \Delta z_{n+1}^{(k)},$$

where :

$$\begin{aligned} \mathbf{R}_{1,n+1}^{(k-1)} &= (\mathbf{S}_M - \mathbf{S}_A) : \boldsymbol{\sigma}_{n+1}^{(k-1)} + \gamma_{n+1}^{(k-1)} \boldsymbol{\epsilon}_{\text{ori}} \\ &+ \left[ z_{n+1}^{(k-1)} \frac{\boldsymbol{\epsilon}_{\text{ori}}}{\tau} (\gamma^{\text{sat}} - \gamma^0) + \frac{\epsilon_r^{\text{sat}}}{\tau} \left( \frac{3}{2} \frac{\mathbf{S}_{n+1}^{(k-1)}}{\sigma_{VM,n+1}^{(k-1)}} \right) \right] \exp \left( -\frac{z_{e,n+1}^{(k-1)}}{\tau} \right). \end{aligned}$$

4. Update the state variables and the parameters of the model.

5. Set  $k = k + 1$  and go to 2.

Table 4. Return mapping algorithm for the cyclic model.

*General case of phase change combined with reorientation of martensite*

For general loading paths, both phase change and martensite reorientation can take place simultaneously. It is thus necessary to develop an algorithm where both state variables can evolve. For the clarity of the equations, this paragraph is restricted to the monocycle ZM model, and only the case of direct phase change is presented. As soon as the martensite is formed, it is assumed to be totally oriented (this is justified when  $\sigma_{rf} < \sigma_{ms}$ ):

$$\sqrt{\frac{2}{3}} \epsilon_{ori} : \epsilon_{ori} = \gamma \quad (2.75)$$

is always verified. The Lagrange multiplier  $\mu$  associated to this unilateral constraint takes non zero values, and the orientation yield function can be written as (*cf.* Eq. (81) from [Zaki and Moumni, 2007a]):

$$\mathcal{F}_{ori} = X_{VM} - zY \text{ with } X = s - \frac{2}{3\gamma^2} (s : \epsilon_{ori}) \epsilon_{ori}. \quad (2.76)$$

The problem is governed by the following constitutive equations:

$$\sigma = S^{-1} : (\epsilon - z\epsilon_{ori}) \quad (2.77)$$

$$\mathcal{F}_z^1(\sigma, z, \epsilon_{ori}) \leq 0, \dot{z} \geq 0, \dot{\mathcal{F}}_z^1 = 0 \quad (2.78)$$

$$\mathcal{F}_{ori}(\sigma, z, \epsilon_{ori}) \leq 0, \dot{\epsilon}_{ori} = \eta \frac{\partial \mathcal{F}_{ori}}{\partial X} = \frac{3\eta X}{2X_{VM}}, \eta \geq 0, \eta \mathcal{F}_{ori} = 0. \quad (2.79)$$

The algorithm involves two steps, as previously: the predictor step and the corrector step.

- The predictor step consists in computing the strain increment and the stress state assuming an elastic evolution (*i.e.* without any evolution of the internal variables).

$$\begin{aligned} z_{n+1}^{(0)} &= z_n, \\ \epsilon_{ori,n+1}^{(0)} &= \epsilon_{ori,n}, \\ \sigma_{n+1}^{(0)} &= S^{-1} \left( z_{n+1}^{(0)} \right) : \left( \epsilon_{n+1} - z_{n+1}^{(0)} \epsilon_{ori,n+1}^{(0)} \right) \end{aligned} \quad (2.80)$$

- The corrector step: the criteria are computed with the new stress state and the unchanged values of internal variables. If the inequalities

$$\begin{aligned} \mathcal{F}_z^1(\sigma_{n+1}^{(k)}, z_{n+1}^{(k)}, \epsilon_{ori,n+1}^{(k)}) &\leq 0 \\ \text{and } \mathcal{F}_{ori}(\sigma_{n+1}^{(k)}, z_{n+1}^{(k)}, \epsilon_{ori,n+1}^{(k)}) &\leq 0, \end{aligned} \quad (2.81)$$

are simultaneously verified, the increment is elastic, and no evolution of the internal variables has to be computed. Else, the evolution of  $z$  and of  $\epsilon_{ori}$  must be computed. Three sets of discrete equations are used to obtain the relations between the increments of the different state variables, namely:

- Taylor series of degree one of both yield functions,

$$\begin{aligned} \mathcal{F}_{z,n+1}^{1,(k)} &= \mathcal{F}_{z,n+1}^{1,(k-1)} + \partial_{\sigma} \mathcal{F}_{z,n+1}^{1,(k-1)} : \Delta \sigma_{n+1}^{(k)} \\ &\quad + \partial_z \mathcal{F}_{z,n+1}^{1,(k-1)} \Delta z_{n+1}^{(k)} + \partial_{\epsilon_{ori}} \mathcal{F}_{z,n+1}^{1,(k-1)} : \Delta \epsilon_{ori,n+1}^{(k)} = 0, \end{aligned} \quad (2.82)$$

$$\begin{aligned} \mathcal{F}_{ori,n+1}^{(k)} &= \mathcal{F}_{ori,n+1}^{(k-1)} + \partial_{\sigma} \mathcal{F}_{ori,n+1}^{(k-1)} : \Delta \sigma_{n+1}^{(k)} \\ &\quad + \partial_z \mathcal{F}_{ori,n+1}^{(k-1)} \Delta z_{n+1}^{(k)} + \partial_{\epsilon_{ori}} \mathcal{F}_{ori,n+1}^{(k-1)} : \Delta \epsilon_{ori,n+1}^{(k)} = 0, \end{aligned} \quad (2.83)$$

- the discrete stress-strain relation,

$$\Delta \boldsymbol{\sigma}_{n+1}^{(k)} = \mathbf{S}_{n+1}^{(k-1),-1} : \left[ \Delta \boldsymbol{\epsilon}_{n+1}^{(k)} - \left( \Delta \mathbf{S}_{n+1}^{(k)} : \boldsymbol{\sigma}_{n+1}^{(k-1)} + \Delta z_{n+1}^{(k)} \boldsymbol{\epsilon}_{\text{ori},n+1}^{(k-1)} + z_{n+1}^{(k-1)} \Delta \boldsymbol{\epsilon}_{\text{ori},n+1}^{(k)} \right) \right], \quad (2.84)$$

where  $\Delta \mathbf{S}_{n+1}^{(k)}$  is function of  $\Delta z_{n+1}^{(k)}$ , given by Eq. (2.70);

- and the discrete consistency condition,

$$\Delta \boldsymbol{\epsilon}_{\text{ori},n+1}^{(k)} = \frac{3}{2} \eta \frac{\mathbf{X}_{n+1}^{(k)}}{\mathbf{X}_{\text{VM},n+1}^{(k)}} = \frac{3}{2} \eta \mathbf{N}_{n+1}^{(k)}, \quad (2.85)$$

where  $\mathbf{N}_{n+1}^{(k)} = \frac{3}{2} \frac{\mathbf{X}_{n+1}^{(k)}}{\mathbf{X}_{\text{VM},n+1}^{(k)}}$  is a unit tensor. For elastoplastic constitutive laws, the elastic prediction of the unit tensor is shown to be parallel to the final unit tensor [see, e.g. [Bonnet and Frangi, 2006](#)]. In the case of pure martensite reorientation, without phase change, this relation holds true:

$$\mathbf{N}_{n+1}^{(k)} = \mathbf{N}_{n+1}^{(k),\text{elas}}. \quad (2.86)$$

However, in the general case, the equality is not verified; as the increment of orientation tensor has to be normal to the final orientation surface, we assume that the elastic prediction of the unit tensor is better oriented than the unit tensor at the previous time step and thus decreases the number of iterations of the return-mapping algorithm. This is why, in the following algorithm, the tensor  $\mathbf{N}$  is  $\mathbf{N}_{n+1}^{(k)}$ , calculated as the elastic prediction (Eq. (2.86)). Because of the iterations of the return-mapping algorithm to get the nullity of the orientation yield function, the final orientation tensor satisfies the constitutive law.

The values of the multiplier  $\eta$  and of the increment of the martensite volume fraction are given by:

$$\Delta z_{n+1}^{(k)} = -\frac{\mathcal{F}_{z,n+1}^{1,(k-1)}}{A_z} - \frac{A_{\text{tr}}}{A_z} \left( \frac{B_z \mathcal{F}_{z,n+1}^{1,(k-1)} - A_z \mathcal{F}_{\text{ori},n+1}^{(k-1)}}{A_z B_{\text{tr}} - B_z A_{\text{tr}}} \right) \quad (2.87)$$

$$\eta = \frac{B_z \mathcal{F}_{z,n+1}^{1,(k-1)} - A_z \mathcal{F}_{\text{ori},n+1}^{(k-1)}}{A_z B_{\text{tr}} - B_z A_{\text{tr}}} \quad (2.88)$$

with:

$$A_z = \partial_z \mathcal{F}_{z,n+1}^{1,(k-1)} - \partial_{\boldsymbol{\sigma}} \mathcal{F}_{z,n+1}^{1,(k-1)} : \mathbf{S}_{n+1}^{-1,(k-1)} : \left( (\mathbf{S}_M - \mathbf{S}_A) : \boldsymbol{\sigma}_{n+1}^{(k-1)} + \boldsymbol{\epsilon}_{\text{ori},n+1}^{(k-1)} \right) \quad (2.89)$$

$$A_{\text{tr}} = \partial_{\boldsymbol{\epsilon}_{\text{ori}}} \mathcal{F}_{z,n+1}^{1,(k-1)} : \mathbf{N}_{n+1}^{(k)} - z_{n+1}^{(k-1)} \partial_{\boldsymbol{\sigma}} \mathcal{F}_{z,n+1}^{1,(k-1)} : \mathbf{S}_{n+1}^{-1,(k-1)} : \mathbf{N}_{n+1}^{(k)} \quad (2.90)$$

$$B_z = \partial_z \mathcal{F}_{\text{ori},n+1}^{(k-1)} - \partial_{\boldsymbol{\sigma}} \mathcal{F}_{\text{ori},n+1}^{(k-1)} : \mathbf{S}_{n+1}^{-1,(k-1)} : \left( (\mathbf{S}_M - \mathbf{S}_A) : \boldsymbol{\sigma}_{n+1}^{(k-1)} + \boldsymbol{\epsilon}_{\text{ori},n+1}^{(k-1)} \right) \quad (2.91)$$

$$B_{\text{tr}} = \partial_{\boldsymbol{\epsilon}_{\text{ori}}} \mathcal{F}_{\text{ori},n+1}^{(k-1)} : \mathbf{N}_{n+1}^{(k)} - z_{n+1}^{(k-1)} \partial_{\boldsymbol{\sigma}} \mathcal{F}_{\text{ori},n+1}^{(k-1)} : \mathbf{S}_{n+1}^{-1,(k-1)} : \mathbf{N}_{n+1}^{(k)} \quad (2.92)$$

In the case of phase change without martensite reorientation (*i.e.*  $\mathcal{F}_{\text{ori}} \leq 0$  and  $\mathcal{F}_z^1 \geq 0$ ),  $\eta = 0$  and the expression of the increment of martensite volume fraction is identical to the case of proportional loadings. In the case of reorientation without phase change (*i.e.*  $\mathcal{F}_{\text{ori}} \geq 0$  and  $\mathcal{F}_z^1 \leq 0$ ),  $\Delta z = 0$  and  $\eta = -\frac{\mathcal{F}_{\text{ori},n+1}^{(k-1)}}{B_{\text{tr}}}$ . The positivity of the multiplier  $\eta$  is numerically verified.

### 2.4.3 Results

In this section, different simulation results are given, for both proportional and non proportional loadings. Results for cyclic loading cases will be given in chapter 5 dedicated to the Direct Cyclic Method.

#### Proportional loadings

A z-axis cylinder shaft (radius 5 mm, height 100 mm) is subject to tension, torsion, or combined tension-torsion loadings. The material parameters used for these simulations are listed in Table 5. The temperature of the specimen is 70 °C. One end of the cylinder is cantilevered, while the other end is subject to imposed displacement.

Parameters values			
$E_A$	61500 MPa	$a$	6.8920 MPa
$E_M$	24000 MPa	$b$	6.9091 MPa
$\nu$	0.3	$G$	23.278 MPa
$\alpha$	2750 MPa	$\beta$	5500 MPa
$\gamma$	4.0 %	$A_f^0$	40 °C
$\xi$	0.2914 MPa/°C	$\kappa$	6.8920 MPa

Table 5. Model parameters

- Tensile loading

The imposed displacement is

$$\xi_d = \xi_{\max} \frac{t}{T} \mathbf{e}_z, \quad \text{with } t \in [0, T]. \quad (2.93)$$

The only non vanishing component of the stress and strain tensor is the tensile component in the z-direction ( $\epsilon_{zz}, \sigma_{zz}$ ), leading to the following expression of the orientation strain tensor (in Cartesian coordinates):

$$\epsilon_{\text{ori}} = \begin{pmatrix} -\gamma/2 & 0 & 0 \\ 0 & -\gamma/2 & 0 \\ 0 & 0 & \gamma \end{pmatrix}. \quad (2.94)$$

The stress-strain response obtained for an imposed tensile displacement of 8 mm is plotted on Fig. 13.

- Torsion loading and comparison with the analytical solution

For pure torsion loading, the mechanical response is not homogeneous through the section, as shown by the analytical resolution. The boundary conditions of the problem are given by Eq. (2.31) and the expression of the orientation tensor by Eq. (2.36). The results are presented for a point situated on the external radius of the cylinder, where stress and strain are maximum. For an imposed torsion angle of  $25^\circ$ , the stress-strain relation  $\epsilon_{\theta z} - \sigma_{\theta z}$  is plotted on Fig. 14.

The numerical algorithm is validated using the analytical solution. For this simulation only, the cylinder has a radius of 10 mm and a height of 50 mm, and it is subject to a twist angle of  $20^\circ$ . Fig. 15 shows the comparison between the analytical solution (in red) and the numerical one (in blue) for three points, situated at different radii of the cylinder. Fig. 16 is the comparison of the torque-angle responses. The perfect superposition of both responses is a validation of the return-mapping algorithm.

- Tension-torsion loading paths

Three tension-torsion loading paths are then simulated, corresponding to different imposed tensile displacement. The expression of the orientation strain tensor depends on the ratio between the maximum tensile stress and the maximum shear stress. Strictly speaking, for displacement-driven loading path, the ratio remains constant only for linear elastic constitutive law, and the assumption of proportional loading is then not valid in the case of pseudoelastic loading. However, the computations are done under this assumption to make them easier, and at the end, the orientation function is computed to verify that the yield criterion is not violated; it is indeed possible that non proportional loading does not lead to reorientation of martensite, when the ratio between the two components does not change considerably; this is verified for either very large or very small ratios, that is if one loading direction is predominant with respect to the other.

So, we assume that the orientation tensor is determined numerically using the nullity of the orientation yield function  $\mathcal{F}_{\text{ori}}$  for  $z = 0^+$ :

$$\epsilon_{\text{ori}} = \frac{3}{2\beta} s_0, \quad (2.95)$$

where  $s_0$  is the stress deviator solution of the elastic problem for the maximum loading.

The different stress-strain responses are reported on Fig. 17. For each case, the tensile response (resp. the shear response) is plotted in red (resp. in blue), while the equivalent stress is plotted with respect to the equivalent strain<sup>4</sup> in black. All responses are given for a point situated on the external radius of the cylinder, to have maximum shear stress.

It is important to verify that the orientation yield function is smaller than a given tolerance. It is plotted in Fig. 18 for all three cases. We notice that, at the very beginning of the direct transformation as well as at the very end of the reverse transformation (*i.e.* when  $z$  and consequently the yield limit  $z_Y$  tend to zero), the yield function is positive, but the maximum value remains reasonably small (3 MPa maximum for both the 5 mm and the 7 mm maximum displacements). However, for the first case ( $\xi_{\text{max}} = 2\text{mm}$ ) where tensile and shear stresses have comparable values, the negativity of the orientation criterion is not verified (black line of Fig. 18). Consequently, the response plotted in Fig. 17a is not correct, and the response has to be computed using the non proportional loading algorithm.

#### *Non-proportional loadings*

Non proportional loadings lead to large computation time, because of the higher number of unknown variables to be computed; the orientation strain tensor is now unknown, and must

<sup>4</sup> The equivalent strain is defined as  $\epsilon_{\text{eq}} = \sqrt{\epsilon_{xx}^2 + \frac{4}{3}\epsilon_{xy}^2}$

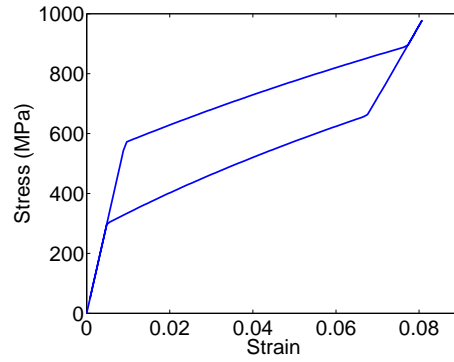


Figure 13. Stress-strain response to an imposed displacement of 8 mm in tension.

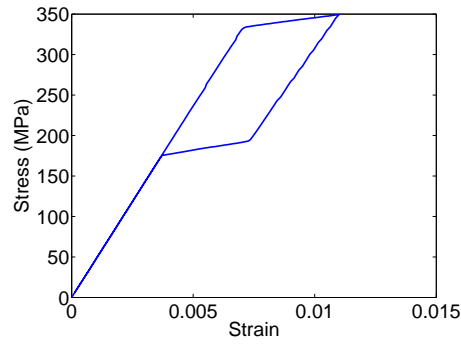


Figure 14. Stress-strain response at a point situated on the external radius of the cylinder and subjected to a  $25^\circ$  torsion angle.

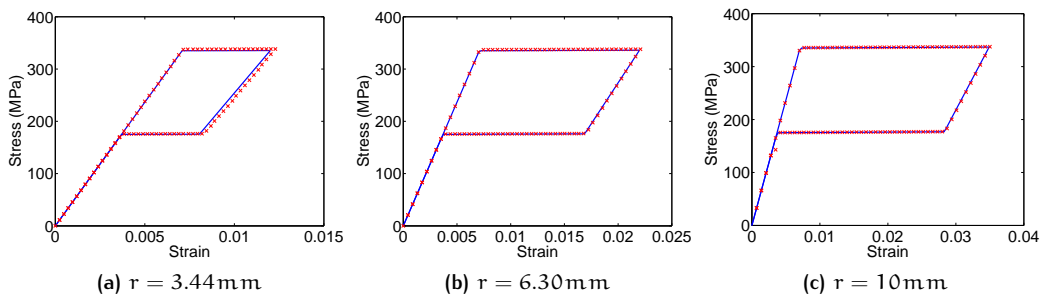


Figure 15. Comparison of analytical (red) and numerical (blue) stress-strain responses for points situated at different radii specified under each figure. In these simulations, the parameters come from Table 5, except  $G=4.6556 \text{ MPa}$ .

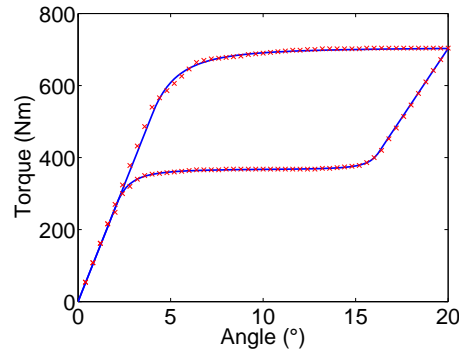


Figure 16. Comparison of analytical (red) and numerical (blue) torque-angle responses for a maximum angle of  $20^\circ$ .

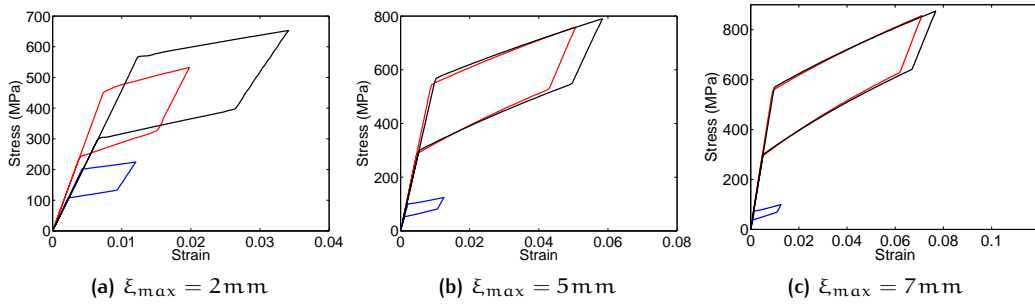


Figure 17. Stress-strain responses for tension-torsion loading paths. The maximum imposed torsion angle is  $30^\circ$ , and the maximum tensile displacement  $\xi_{\max}$  is specified under each figure. In all figures, the blue line is related to the shear response, the red one to the tensile components and the black one to the equivalent stress-strain response.

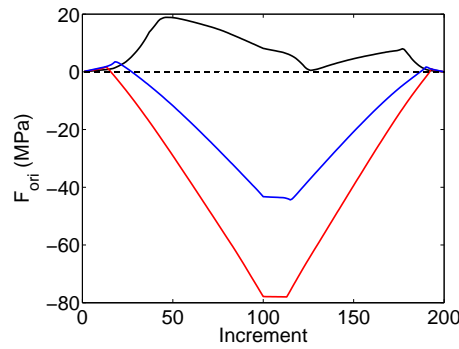


Figure 18. Evolution of the orientation yield function for the different loading paths. The black dotted line corresponds to zero. The black (resp. blue, red) curve corresponds to a maximum tensile displacement of 2 mm (resp. 5 mm and 7 mm)

be determined using the consistency conditions associated to the orientation yield function. For simplicity, the algorithm, restricted to one axial and one shear component of the stress tensor, is first implemented in Matlab.

- Martensite orientation in Matlab

The case of martensite orientation is similar to elasto-plastic behavior with kinematic hardening. Indeed,

$$\mathcal{F}_{\text{ori}} = \begin{cases} \|\sigma - \alpha \epsilon_{\text{ori}}\| - Y \leq 0 & \text{if } \|\epsilon_{\text{ori}}\| < \gamma \\ \left\| \sigma - \frac{2}{3\gamma^2} (\mathbf{s} : \epsilon_{\text{ori}}) \epsilon_{\text{ori}} \right\| - Y \leq 0 & \text{if } \|\epsilon_{\text{ori}}\| = \gamma \end{cases}. \quad (2.96)$$

It consists thus in implementing the elasto-plastic return mapping algorithm, which is easier than the completely non proportional one.

The problem is stress-driven, and consists of determining both the strain and the orientation strain.

For a tensile loading, the stress-strain curve is given on Fig. 19.

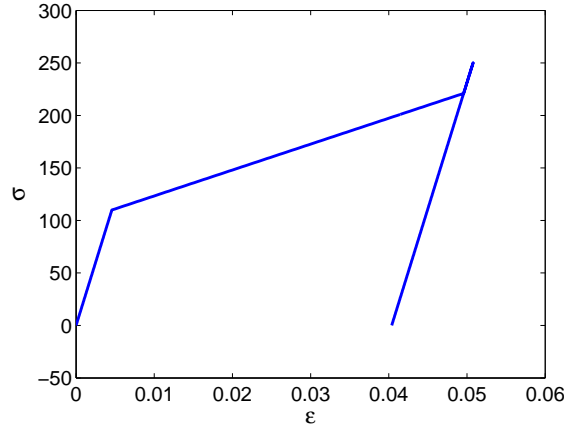


Figure 19. Martensite orientation stress-strain response in tension.

Two square-paths are then considered.

1. The loading is first in the tensile direction, then, under constant tensile stress, a shear stress is applied. Maintaining the maximum shear stress, the tensile stress is unloaded and finally the shear stress is removed (*cf.* Fig. 20). The corresponding results are given in Figs. 20b, 21. During the first part of the loading path, the tensile component of the orientation strain increases, while the shear component is zero (Fig. 20b). This leads to the classical stress-strain response (blue line of Fig. 20a). Then, when the shear stress increases under constant tensile stress, the tensile component of the orientation tensor decreases in favor of the shear component, which increases. Consequently, the tensile strain decreases to maintain constant stress, and the shear strain increases, first elastically; the reorientation does not occur immediately, but only when the ratio of the shear and tensile stresses reaches a critical value (red responses in Figs. 20b and 21). Third, the tensile stress is removed, leading to a small reorientation of the martensite, as seen by the increase of the shear strain, and by the different slope of the tensile stress-strain curve. A tensile

residual strain exists when the tensile load is removed (black line of Fig. 20b). Finally, the shear stress is removed and as previously, a small reorientation occurs, to maintain the nullity of the orientation yield function. The reorientation involves a small increase of the tensile strain at the beginning of the unloading. The end of the unloading occurs elastically (magenta lines).

2. The second loading path begins with the shear stress increase (cf. Fig. 22a). The corresponding stress-strain responses and shear-tensile strain response are given in Fig. 22b and 23. Similar responses are observed, except that during the removal of the tensile loading, no reorientation occurs; indeed, the orientation yield function is negative during the last portion of the loading path.

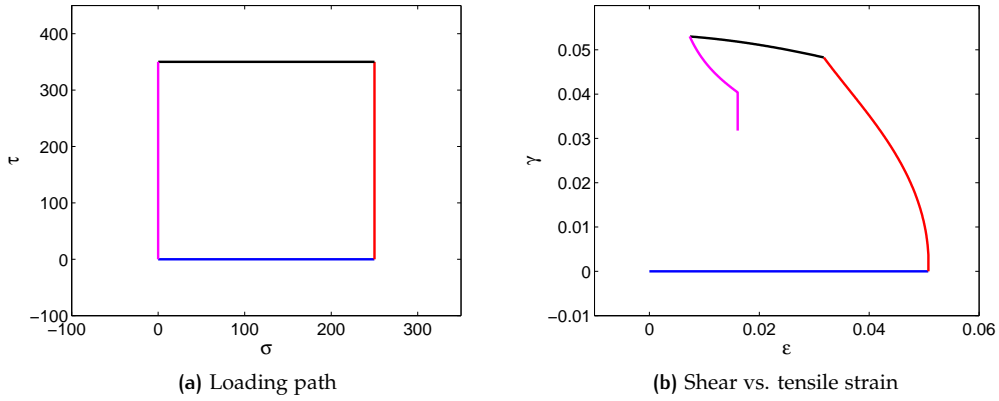


Figure 20. (a) Loading path: from a natural unloaded state, the material is loaded along the blue, red, black, and finally magenta paths. (b) Shear strain vs. tensile strain response corresponding to the loading path presented in (a).

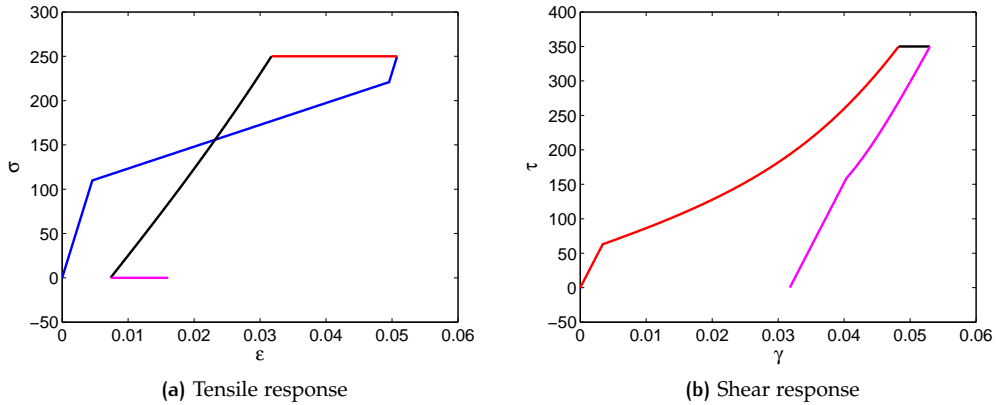


Figure 21. Stress-strain responses for both components, corresponding to the loading path plotted in Fig. 20.

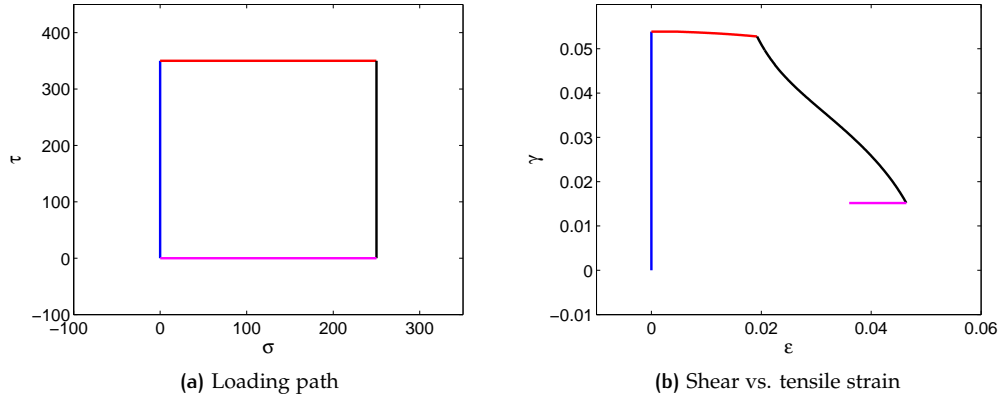


Figure 22. (a) Loading path: from a natural unloaded state, the material is loaded along the blue, red, black, and finally magenta paths. (b) Shear strain vs. tensile strain response corresponding to the loading path presented in (a).

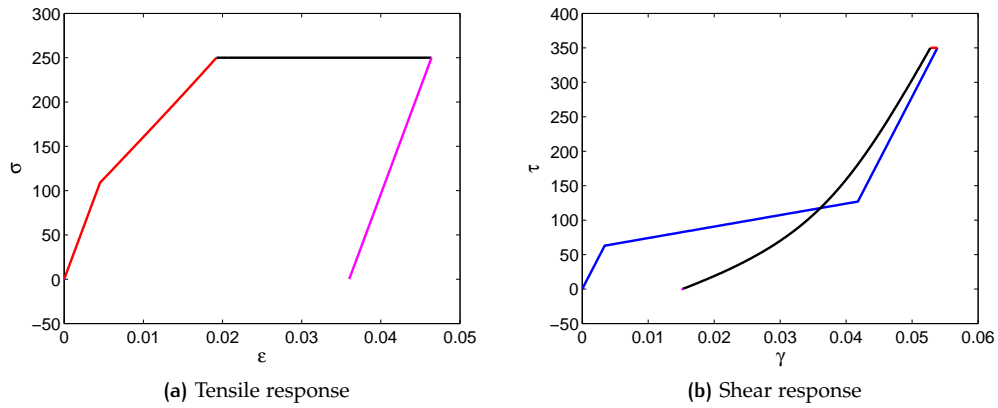


Figure 23. Stress-strain responses for both components, corresponding to the loading path plotted in Fig. 22a.

- Local resolution of non proportional pseudoelasticity in Matlab

Let us now present the results obtained with Matlab for pseudoelasticity under non proportional loading. Different strain-driven loading paths are considered, and the different responses are compared and commented. In figures 24-26, tensile response is plotted with red line, shear response with blue line and equivalent response with black dotted line. The material parameters are those given in Table 2. The temperature is 50 °C.

- Proportional loadings are first simulated: tensile loading and shear loading (*cf.* Fig. 24). A maximum strain of 6 % is applied. Combined tensile-shear loading is presented in Fig. 25. We notice that the orientation strain components are not perfectly constant as expected; this local problem is strictly speaking non proportional.
- Two non-proportional loading paths are chosen. A tensile (*resp.* shear) strain is imposed followed by a shear (*resp.* tensile) strain. The unloading phase follows the same path as the loading phase. The responses are plotted in Fig. 26. The increase of the shear strain causes the instantaneous reorientation of the martensite, as the stress state is higher than the orientation yield stress. Thus, the tensile component of the orientation strain decreases, while the shear one increases, maintaining an equivalent strain constant and equal to the maximum orientation strain. The inverse tendency is observed during unloading. The decrease of the orientation tensile strain due to the reorientation induces a stress softening. However, the beginning of the unloading is elastic, until the ratio between shear and tensile stresses changes enough to induce reorientation. This explains the small horizontal plateau visible on the stress-strain response at the beginning of the unloading.

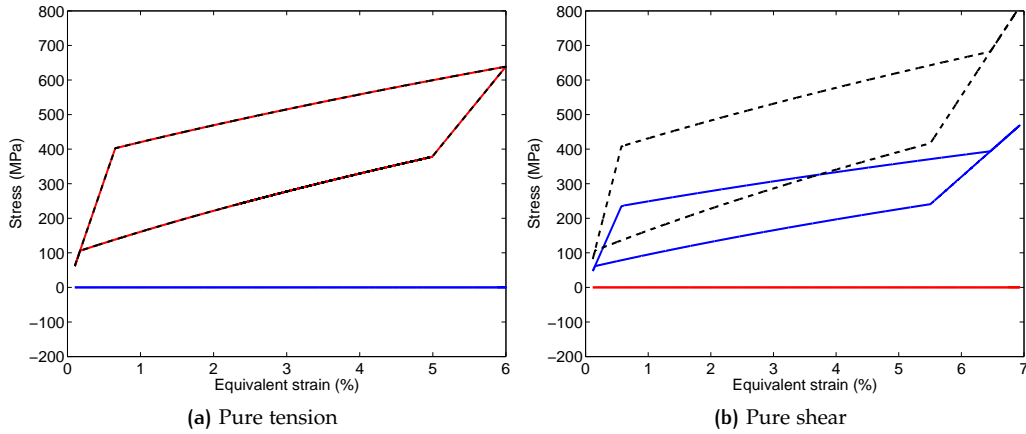


Figure 24. Stress-strain responses for pure tension loading (a) or pure torsion loading (b).

- Implementation of the non proportional algorithm in Castem

Let us consider a cube with a 10 mm-long edge. The axes of the cube are parallel to the cartesian coordinate vectors (*cf.* Fig. 27a).

The boundary conditions are

- $\xi(0, 0, 0) = 0,$
- $\xi(x, y, z = 0) = 0,$
- $\xi(x = 0, y, z) = 0,$

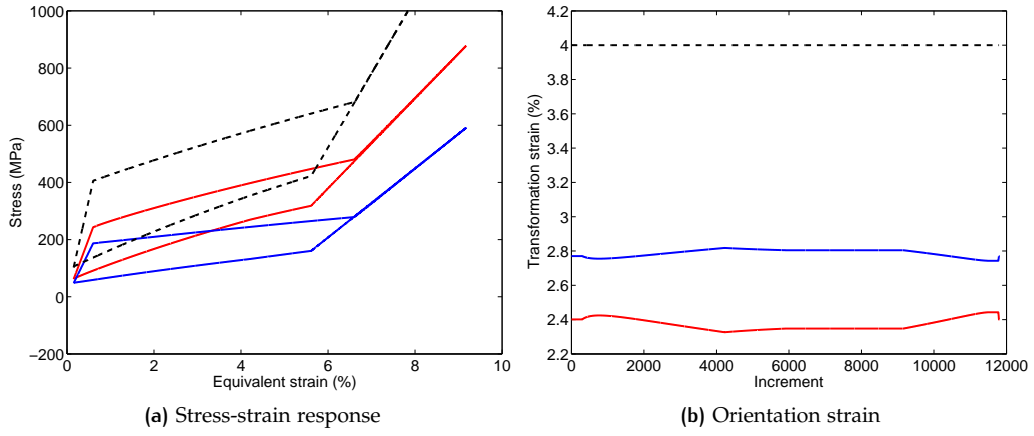


Figure 25. Proportional shear-tension loading. (a) Evolution of the mechanical response. (b) Evolution of the orientation strain components.

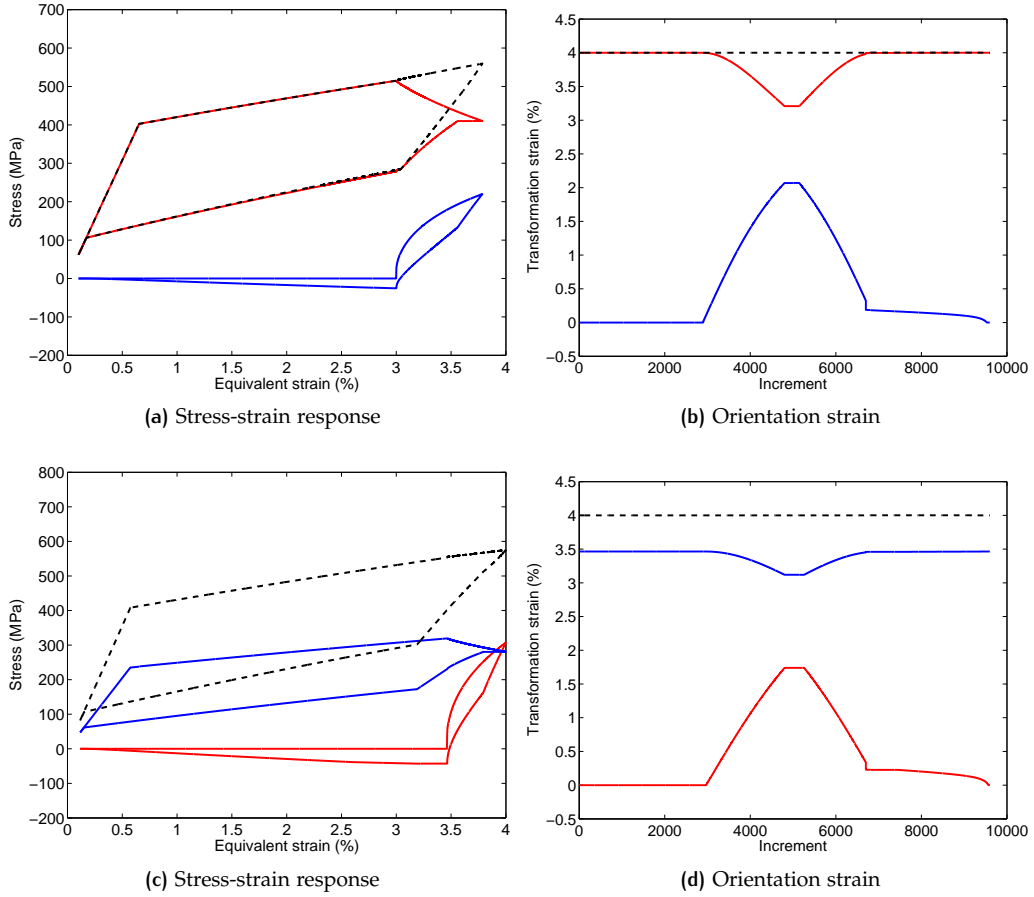


Figure 26. (a) and (b) 3 % tension strain followed by 2 % shear strain and unloading. (c) and (d) 3 % shear strain followed by 2 % tensile strain and unloading.

- $T_z(x, y, z = 10) = T_1$ ,
- $T_x(x = 10, y, z) = T_2$ .

The remaining boundary conditions are stress-free conditions.  $T_1$  is a tensile force, while  $T_2$  is a compressive force; their temporal evolution, plotted on Fig. 27b, are given below for loading; during unloading, the reverse path is taken.

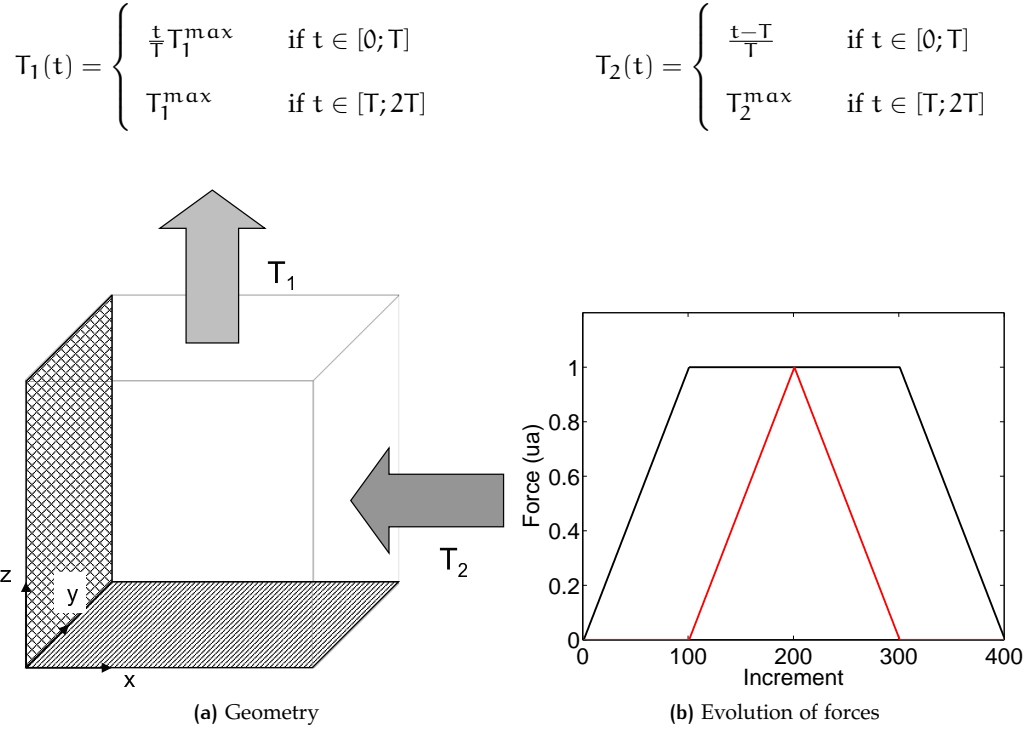


Figure 27. (a) Geometry and boundary conditions of the simulated specimen. Zero displacements are imposed perpendicularly to the colored surfaces. (b) Evolution of the loading direction with respect to time. The normalized tensile force in the z-direction (resp. the normalized compressive force in the x-direction) is plotted in black (resp. in red).

The problem is stress-driven. Fig. 28 shows the stress-strain responses in the x- and z- direction as well as the evolution of the orientation strain tensor with respect to the kinematic time. Fig. 29 shows the evolution of the different yield functions with respect to the kinematic time. In these figures, the different steps of the loading path have been plotted in different colors:

- red: increase of  $T_1$  (z-direction) while  $T_2 = 0$  (x-direction),
- black: increase of  $T_2$  (x-direction) while  $T_1 = T_1^{\max}$  (z-direction),
- blue: decrease of  $T_2$  (x-direction) while  $T_1 = T_1^{\max}$  (z-direction),
- magenta: decrease of  $T_1$  (z-direction) while  $T_2 = 0$  (x-direction).

During the first step, due to the tensile force in the z direction,  $\sigma_{zz}$  increases and reaches the yield value for phase change ( $\mathcal{F}_z^1$  becomes equal to zero). The orientation tensor is equal to  $\gamma$  for

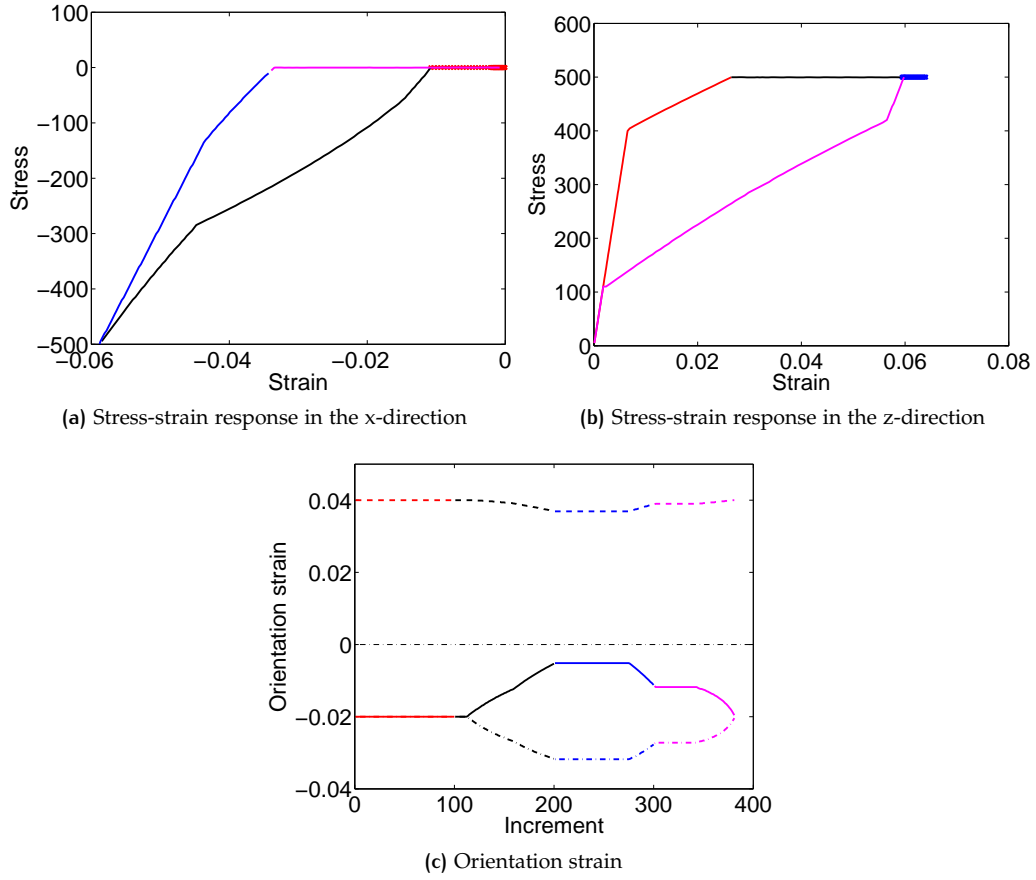


Figure 28. (a) Stress strain response in the x-direction. (b) Stress-strain response in the z-direction. (c) Evolution of different components of the orientation tensor with respect to the kinematic time; the solid line stands for the y-direction, the dotted line – for the z-direction and the dotted line -. for the x-direction.

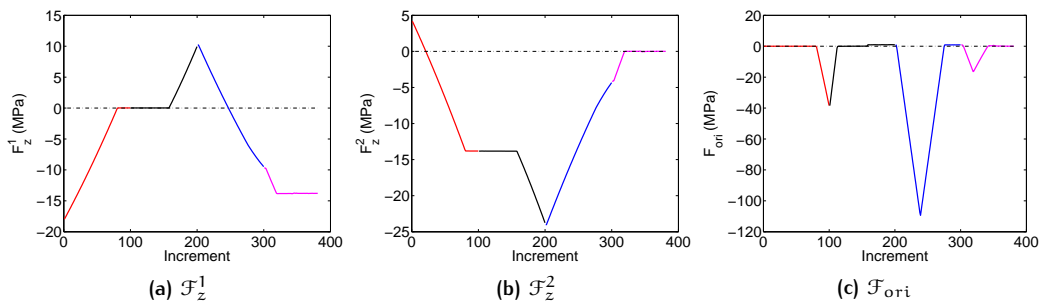


Figure 29. Evolution of the different yield functions with respect to the kinematic time.

the tensile direction. Besides, the strain in the other directions increases to maintain a zero stress state.

During the second step of the loading, two different responses must be distinguished. First, the increase of stress allows the phase change to go further ( $\mathcal{F}_z^1$  remains equal to zero); soon after the beginning of the compression, reorientation of the martensite occurs ( $\mathcal{F}_{ori}$  becomes equal to zero). The x-component of the orientation strain tensor increases, and the z-component decreases a little : the increase of the x-component is balanced by the decrease of the y-component (which could not be seen in the Matlab analysis). The second phase begins when phase change is finished. The stress-strain response becomes linear, but the reorientation of martensite continues.

During the third step, the compressive force along the x-direction is removed. During this step, no phase change is induced ( $\mathcal{F}_z^2 < 0$ ). In the beginning, the behavior is linear elastic, without martensite reorientation. When the compressive force becomes too small, reorientation is induced in the material ( $\mathcal{F}_{ori} = 0$ ): the x-component decreases in favor of the y-component and to a lesser extent in favor of the z-component. Besides, the strain in the z-direction increases to maintain a constant stress in this direction.

Finally, during the removal of the tensile force, the response is first elastic without phase change ( $\mathcal{F}_z^2 < 0$ ) or reorientation ( $\mathcal{F}_{ori} < 0$ ). During the beginning of the reverse phase change, no reorientation occurs, but only at the end: the yield stress, which depends on  $z$ , is small enough to induce reorientation.

The presented results show the ability of the model to simulate either proportional cyclic loading paths or more complex loading paths. However, due to the large number of parameters to derive, the algorithm for cyclic non proportional loadings is not implemented. Besides, the computation time becomes quite large for complex non proportional loading, because of the difficulty to reach both admissibilities with constitutive law and with equilibrium.

## 2.5 CONCLUSION AND PROSPECTS

This chapter presented the main features of the ZM models, as well as the return mapping algorithms necessary for numerical implementation of the models. The presented return mapping algorithms allow the computation of SMA structures subjected to pseudoelastic loadings. In the case of proportional loadings, the return mapping leads to reasonable computation time, but the computation time becomes large for non proportional loadings, due to the higher number of criteria which have to be simultaneously verified. The analytical solution in torsion is useful to validate the return-mapping algorithm.

Although the ZM models are 3D models able to simulate the main behaviors of SMA within a unique framework, they present some drawbacks. The behavior of Shape Memory Alloys is known to have a more complex yield surface of phase change and to show different responses in tension and in compression. Besides, the role of temperature is not taken into account accurately; the model only allows imposed temperature variations, and does not reproduce the thermomechanical couplings in these alloys and resulting from the dependence of the yield stresses on temperature. These drawbacks are taken into account and some extensions of the models are proposed in the following chapters.

# 3 | MODELING TENSILE-COMPRESSIVE ASYMMETRY

---

3.1	Literature review on tensile-compressive asymmetry	47
3.1.1	Experimental observations	47
3.1.2	Different models for tensile-compressive asymmetry	49
3.2	Tensile compressive asymmetry in the ZM model	50
3.2.1	Mathematical framework of Raniecki and Mroz	50
3.2.2	Introducing the third invariant	51
3.2.3	Parameters identification procedure	54
3.3	Validation	55
3.3.1	Comparison with experimental results	55
3.3.2	Comparison with the phase change yield function of <a href="#">Orgeas and Favier [1998]</a>	57
3.4	Conclusion	57

---

The prediction of the stabilized state of the structure requires a model able to reproduce the main features of the shape memory alloy behavior. The tensile-compressive asymmetry leads to changes in the yield stresses, slopes of the plateaus and thus in the hysteresis area as well as in the maximum hydrostatic pressure. For this reason, it is important to incorporate the asymmetry in the ZM model to get a correct prediction of the number of cycles to failure, since the fatigue lifetime is evaluated using the hysteresis area. In this chapter, the ZM model for Shape Memory Alloys is extended to simulate tensile-compressive asymmetry for superelasticity. Experimental validation of the extended model is shown to reproduce the asymmetric stress-strain response for pseudoelasticity and martensite detwinning.

## 3.1 LITERATURE REVIEW ON TENSILE-COMPRESSIVE ASYMMETRY

The martensitic transformation is influenced by the sign of the applied load, which makes the macroscopic behavior of SMAs generally asymmetric in tension-compression. This asymmetry seems to have been first reported by [Wasilewski \[1971\]](#) and has since attracted the interest of a number of researchers.

### 3.1.1 Experimental observations

[Wasilewski \[1971\]](#) reported that compressive loadings lead to

- higher yield stresses,
- higher slopes of the phase change plateaus,
- and lower recoverable strain,

compared to tensile loadings.

Orgéas and Favier [1998] carried mechanical experiments in the pseudoelastic domain as well as in the martensite orientation domain (*cf.* Figs. 30 and 31).

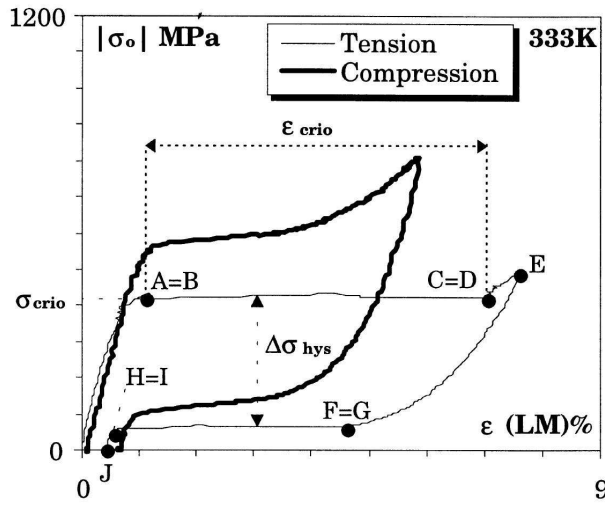


Figure 30. Experimental stress-strain curves in tension and in compression for a pseudoelastic NiTi SMA. The figure is taken from Orgéas and Favier [1998].

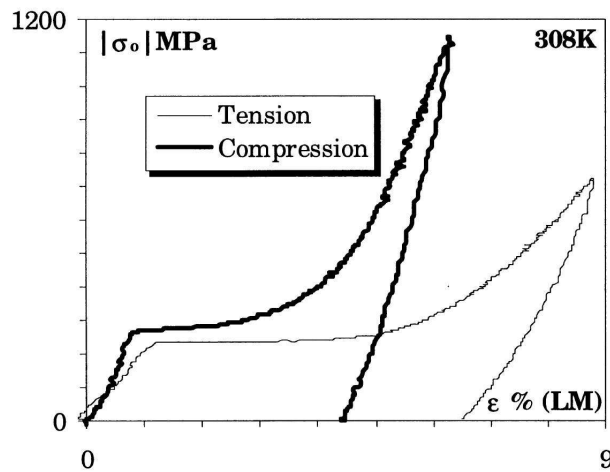


Figure 31. Experimental stress-strain curves in tension and in compression for a martensitic NiTi SMA. The figure is taken from Orgéas and Favier [1998].

Fig. 30 shows the stress-strain response of a pseudoelastic NiTi shape memory alloy in tension and in compression, while Fig. 31 shows the stress-strain response in the case of martensite orientation. Both kinds of responses are influenced by the sign of the load, and the three previous observations from Wasilewski are verified. For shear tests, it was found that the evolution of the critical stress for martensite transformation with respect to temperature is almost linear for all three modes of loading, but with different slopes. However, for temperatures near the martensite start temperature  $M_s$ , plastic deformation seems to play an important role and the relation is no more linear. Orgéas and Favier found that the shear to tensile yield stress ratio is

compatible with the Von Mises criterion (a ratio of  $\sqrt{3}$ ). This conclusion does not hold, however, for compressive stress. The authors demonstrated that hydrostatic pressure cannot explain the observed asymmetry between tension and compression, although it seems to play a role in reducing the magnitude of the asymmetry. Finally, they observed Lüders-like behavior in tension but not in compression.

Explanations of the asymmetry at the microscopic scale are proposed by different authors. Among them, [Liu et al. \[1998\]](#) observed that compressive loading of martensite introduces a high density of dislocations inside twin bands and in the accommodation areas; no reorientation of martensitic variants is observed in compression whereas tensile loading leads to the detwinning of the martensitic variants. The driving mechanism of the martensite orientation process is different: it consists in the generation and movement of lattice defects for compression, while tension induces the migration of the variant interfaces. The difference in driving mechanisms between tension and compression has also been reported by [Gall et al. \[2001\]](#).

[Gall and Sehitoglu \[1999\]](#) performed experiments for different orientations of single crystals and polycrystals. According to them, the tensile-compressive asymmetry is due to the strong orientation dependence of the single crystal. It is also strongly influenced by the size of the precipitates, as precipitates do not undergo the martensitic transformation. Concerning the asymmetry observed in polycrystals, they noted a strong influence of the texture.

### 3.1.2 Different models for tensile-compressive asymmetry

#### *Micromechanics based models*

[Gall and Sehitoglu \[1999\]](#) proposed a micromechanics model based on Schmid's law that was shown to agree with experimental data on single crystals. [Sittner and Novak \[2000\]](#) used constant stress averaging to determine the behavior of polycrystalline SMAs from experimental data on single crystals. [Brocca et al. \[2002\]](#) proposed a micro-plane approach to model the asymmetry of the martensite orientation. [Lexcelent and Blanc \[2004\]](#) developed a specific micro-macro model for NiTi alloy, as NiTi alloy exhibit different crystallographic mechanisms for the martensitic transformation. Some models are based on the phenomenological theory of martensite crystallography [see e.g., [Buchheit et al., 1995](#); [Ono and Shimanuki, 1990](#); [Patoor et al., 1995](#)] or on lattice deformation models. The results of the latter models seem to be doubtful, according to [Orgeas and Favier \[1998\]](#). Finally, the model from [Buchheit and Wert \[1996\]](#) combined the first approach with the introduction of a detwinning process, which leads to good agreement with experimental results, even for NiTi alloys, because of the important role of detwinning in the tensile compressive asymmetry.

#### *Macroscale models*

[Orgeas and Favier \[1998\]](#) proposed a yield criterion for phase change based on the deviatoric stress tensor intensity (proportional to the second invariant of stress) and its phase (proportional to the ratio between the second and the third invariants). Their yield criterion is shown to be in good agreement with experimental data.

[Qidwai and Lagoudas \[2000\]](#) used the first stress invariant with the second and third invariants of the stress deviator to build a class of 'generalized' transformation functions for NiTi SMAs. The functions were shown to fit superelastic tensile-compressive data but martensite orientation at lower temperatures was not considered. However, the introduction of the first stress invariant seems contradictory with experimental results dealing with the role of the hydrostatic pressure.

[Anand and Gurtin \[2003\]](#) developed a 3D constitutive model for single-crystal shape memory materials. The ability of the model to account for tension-compression asymmetry was shown through numerical simulations, which were not validated experimentally.

[Paiva et al. \[2005\]](#) developed a model accounting for tensile-compressive asymmetry by introducing different variants of martensite (namely one for tension, one for compression) with different elastic properties. Thus, the model contains no physical explanation of the asymmetry.

[Auricchio et al. \[2009\]](#) extended a model initially developed by [Auricchio and Petrini \[2002\]](#) to account for tensile-compressive asymmetry by rewriting the yield functions governing the orientation of martensite in terms of Prager-Lode instead of Von Mises equivalent stress. The extended model successfully captures the asymmetry of the phase change thresholds but considers identical slopes for the stress-strain curve during phase change in tension and in compression.

### 3.2 TENSILE COMPRESSIVE ASYMMETRY IN THE ZM MODEL

Our work aims at extending the ZM model to account for the tensile-compressive asymmetry. The extended model should be able to reproduce the asymmetry of the yield stresses, as predicted by most of the previous authors, the asymmetry of the slopes of the phase change plateau, and the asymmetry of the recoverable strain. This will be done by introducing the third invariant of different quantities, using the framework proposed by [Raniecki and Mroz \[2008\]](#).

#### 3.2.1 Mathematical framework of Raniecki and Mroz

[Raniecki and Mroz \[2008\]](#) proposed a class of yield functions depending on the second and third invariants. This allows modelling the Strength Differential Effect exhibited by a number of metallic alloys, including by shape memory alloys. Prior to this work, another class of uneven criteria had been developed by introducing the first and second invariants, which is associated with pressure dependent flow. Using the first invariant does not seem appropriate, because martensite transformation is generally accepted to be insensitive to pressure [cf. [Orgeas and Favier, 1998](#)]. The asymmetric criterion is defined in terms of the second and third deviatoric stress invariants,

$$J_2 = \frac{1}{2} \text{tr}(\mathbf{s}^2), \quad (3.1)$$

$$J_3 = \frac{1}{3} \text{tr}(\mathbf{s}^3) = \det(\mathbf{s}). \quad (3.2)$$

The Lode invariants are introduced:

$$r = \sqrt{2J_2} \quad (3.3)$$

$$y = \frac{3\sqrt{3}J_3}{2(J_2)^{3/2}} \text{ and } y \in [-1, 1]. \quad (3.4)$$

The general form of the yield criterion is:

$$\mathcal{F} = f(y)r - \sqrt{2}\tau_c = 0 \text{ with } f(y) > 0, f(0) = 1. \quad (3.5)$$

[Raniecki and Mroz \[2008\]](#) study more precisely two general forms of the function  $f$ :

- the exponential shape function,
- the power shape function.

For each class of yield functions, they give conditions on the material parameters required to fulfill the convexity condition. Finally, they derive the form of the pseudo-potential of dissipation for such yield functions.

As our model will be extended using the power shape function, let us develop the main properties of this class of yield functions. The function  $f$  is chosen as

$$f(y) = (1 + by)^n \text{ with } |b| \leq 1. \quad (3.6)$$

Particular values of the exponent  $n$  give the yield functions proposed by other scientists. The convexity condition can be expressed by:

$$\mathcal{C} = A_0 y^2 + B_0 y + C_0 \geq 0, \quad (3.7)$$

where:

$$\begin{aligned} A_0 &= b^2 (1 - 9n^2), \\ B_0 &= b (2 - 9n), \\ C_0 &= 1 + 9b^2 n (n - 1). \end{aligned} \quad (3.8)$$

In the proposed extension of the ZM model, the third invariant is being introduced in different quantities in the following way:

$$a^{\text{eff}} = \sqrt[3]{k_a (J_{2,a}^{3/2} - c_a J_{3,a})}, \quad (3.9)$$

where  $a$  is a second-order tensor,  $J_2$  and  $J_3$  its second and third deviatoric invariants, and  $k_a$  and  $c_a$  are material parameters. This gives:

$$n = \frac{1}{3}, \quad (3.10)$$

$$b = -\frac{2c_a}{3\sqrt{3}}. \quad (3.11)$$

Thus, the convexity condition reduces to:

$$\begin{aligned} A_0 &= 0, \\ B_0 &= -b, \\ C_0 &= 1 - 2b^2, \\ \mathcal{C} &= -by + 1 - 2b^2 \geq 0, \text{ for } y \in [-1, 1], \end{aligned} \quad (3.12)$$

leading to:

$$|b| \leq \frac{1}{2} \Rightarrow |c_a| \leq \frac{3\sqrt{3}}{4}. \quad (3.13)$$

No restriction is imposed on the parameter  $k_a$ .

### 3.2.2 Introducing the third invariant

The extension of the ZM model to account for tensile-compressive asymmetry has been started by [Zaki \[2010\]](#). He proposes extension for the case of martensite reorientation. We generalize this work to the entire ZM model, and show that it is simultaneously able to reproduce both martensite orientation and pseudoelastic tensile-compressive asymmetry. Von-Mises equivalent quantities are replaced by Raniecki and Mroz functions as shown in the following sections. The different steps of the model construction are reviewed and adequately modified.

### Internal constraints

Following [Raniecki and Mroz \[2008\]](#), the third invariant of the orientation strain tensor is used to build the following sign-sensitive expression of the equivalent orientation strain:

$$\epsilon_{\text{ori}}^{\text{eff}} = \sqrt[3]{k_{\text{ori}} \left( J_{2,\text{ori}}^{3/2} - c_{\text{ori}} J_{3,\text{ori}} \right)}, \quad (3.14)$$

where  $k_{\text{ori}}$  and  $c_{\text{ori}}$  are material parameters and  $J_{2,\text{ori}}$  and  $J_{3,\text{ori}}$  are the second and third invariants of  $\epsilon_{\text{ori}}$ . If the parameter  $k_{\text{ori}}$  is taken such that  $\epsilon_{\text{ori}}^{\text{eff}}$  is the equivalent tensile orientation strain, the constraint in (2.5) can be rewritten as

$$\gamma_t - \epsilon_{\text{ori}}^{\text{eff}} \geq 0, \quad (3.15)$$

where  $\gamma_t$  is the maximum orientation strain in uniaxial tension.

### The Helmholtz free energy

The interaction energy, which was defined in the original ZM model as

$$\mathcal{J} = \frac{z}{2} (\alpha z + \beta (1 - z)) \left( \frac{2}{3} \epsilon_{\text{ori}} : \epsilon_{\text{ori}} \right), \quad (3.16)$$

is modified. This modification leads to modified phase transformation functions  $\mathcal{F}_z^1$  and  $\mathcal{F}_z^2$  and martensite orientation yield function  $\mathcal{F}_{\text{ori}}$ . An expression similar to Eq. (3.14) is used to define a new equivalent orientation strain, which is then employed to construct a new expression of  $\mathcal{J}$ , which becomes

$$\mathcal{J} = \frac{z}{2} (\alpha z + \beta (1 - z)) \left( \epsilon_{\text{ori}}^{\text{eff}2} \right)^2, \quad (3.17)$$

where

$$\epsilon_{\text{ori}}^{\text{eff}2} = \sqrt[3]{k_h \left( J_{2,\text{ori}}^{3/2} - c_h J_{3,\text{ori}} \right)}; \quad (3.18)$$

$k_h$  and  $c_h$  are material parameters.

The expression of the Lagrangian becomes

$$\begin{aligned} \mathcal{L} = \mathcal{L}(\epsilon, T, \epsilon_A, \epsilon_M, z, \epsilon_{\text{ori}}) = & (1 - z) \left[ \frac{1}{2} \epsilon_A : \mathbf{K}_A : \epsilon_A \right] \\ & + z \left[ \frac{1}{2} (\epsilon_M - \epsilon_{\text{ori}}) : \mathbf{K}_M : (\epsilon_M - \epsilon_{\text{ori}}) + C(T) \right] \\ & + G \frac{z^2}{2} + \frac{z}{2} [\alpha z + \beta (1 - z)] \left\{ k_h \left( J_{2,\text{ori}}^{3/2} - c_h J_{3,\text{ori}} \right) \right\}^{2/3} \\ & - \nu_1 z - \lambda : [(1 - z) \epsilon_A + z \epsilon_M - \epsilon] \\ & - \mu \left( \gamma_t - \sqrt[3]{k_{\text{ori}} \left( J_{2,\text{ori}}^{3/2} - c_{\text{ori}} J_{3,\text{ori}} \right)} \right) - \nu_2 (1 - z), \end{aligned} \quad (3.19)$$

where  $\lambda$ ,  $\mu$ ,  $\nu_1$ , and  $\nu_2$  are Lagrange multipliers satisfying the Kuhn-Tucker conditions (2.7).

### Yield functions

With regard to the original ZM model, the expressions of the thermodynamic forces associated with  $z$  and with  $\epsilon_{\text{ori}}$  are now modified but the pseudo-potential of dissipation (2.12) remains the same. The expressions of the yield functions become

$$\begin{aligned} \mathcal{F}_z^1 = & \frac{1}{3} \text{El}_{\text{MA}} \sigma_{\text{VM}}^2 + \frac{1}{2} \left( \frac{1}{3} \text{El}_{\text{MA}} + \text{P}_{\text{MA}} \right) (\text{tr } \sigma)^2 - C(T) + \sigma : \epsilon_{\text{ori}} - (G + b) z \\ & - a(1 - z) - \left[ (\alpha - \beta) z + \frac{\beta}{2} \right] \left\{ k_h \left( J_{2,\text{ori}}^{3/2} - c_h J_{3,\text{ori}} \right) \right\}^{2/3}, \end{aligned} \quad (3.20)$$

$$\begin{aligned} \mathcal{F}_z^2 = & -\frac{1}{3} \text{El}_{\text{MA}} \sigma_{\text{VM}}^2 - \frac{1}{2} \left( \frac{1}{3} \text{El}_{\text{MA}} + \text{P}_{\text{MA}} \right) (\text{tr } \sigma)^2 + C(T) - \sigma : \epsilon_{\text{ori}} + (G - b) z \\ & - a(1 - z) + \left[ (\alpha - \beta) z + \frac{\beta}{2} \right] \left\{ k_h \left( J_{2,\text{ori}}^{3/2} - c_h J_{3,\text{ori}} \right) \right\}^{2/3}, \end{aligned} \quad (3.21)$$

and

$$\mathcal{F}_{\text{ori}} = \|\mathbf{X}\|_{\text{VM}} - zY, \quad (3.22)$$

where  $\mathbf{X}$  is given by:

$$\mathbf{X} = \sigma - (\alpha z + \beta(1 - z)) \epsilon_{\text{ori}}^{\text{eff}2} \frac{\partial \epsilon_{\text{ori}}^{\text{eff}2}}{\partial \epsilon_{\text{ori}}} - \frac{\mu}{3z} \frac{k_{\text{ori}}}{(\epsilon_{\text{ori}}^{\text{eff}})^3} \left( \frac{3}{2} \sqrt{J_{2,\text{ori}}} \mathbf{1} - c_{\text{ori}} \epsilon_{\text{ori}} \right) \cdot \epsilon_{\text{ori}}, \quad (3.23)$$

where  $\mathbf{1}$  is the identity tensor.

The yield function for martensite orientation is even, which does not allow for different thresholds in tension and in compression. Nevertheless, the asymmetry of the hardening moduli in tension and in compression is accounted for. In order to obtain different stress thresholds, following Raniecki and Mroz [2008], this expression of  $\mathcal{F}_{\text{ori}}$  is assumed:

$$\mathcal{F}_{\text{ori}} = X^{\text{eff}} - zY, \quad (3.24)$$

where

$$X^{\text{eff}} = \sqrt[3]{k_X \left( J_{2,X}^{3/2} - c_X J_{3,X} \right)}. \quad (3.25)$$

In the above equation,  $k_X$  and  $c_X$  are material parameters and  $J_{2,X}$  and  $J_{3,X}$  are the second and third invariants of the deviator of  $\mathbf{X}$ . The pseudo-potential of dissipation associated to the yield function can be derived following Raniecki and Mroz [2008]. As shown by these authors, if the parameters  $k_X$  and  $c_X$  verify the convexity condition, the obtained potential is still convex and equal to zero for zero fluxes of the variables. This ensures the positivity of the intrinsic dissipation associated to the orientation tensor. The intrinsic dissipation associated to phase change is positive, as the phase change yield function derives from the pseudo-potential of dissipation.

The extension of the ZM model introduced new parameters which have to be identified; this is the topic of the next section.

### 3.2.3 Parameters identification procedure

The modified model has the following parameters:

- Young's moduli of austenite  $E_A$  and martensite  $E_M$  and the Poisson coefficient  $\nu$  assumed to be identical for the two phases,
- The maximum orientation strain in tension,  $\gamma_t$ ,
- $a$  and  $b$ , which control the width of the hysteresis superelastic loop;  $Y$ , the orientation yield stress;  $G$ , which influences the slope of the stress-strain curve during phase transition;  $\alpha$  and  $\beta$ , controlling the evolution of stress with the orientation strain;  $\xi$  and  $\kappa$ , which influence the dependence on temperature of the critical stresses for phase change,
- $k_{ori}$  and  $c_{ori}$ , governing the tensile-compressive asymmetry of the maximum orientation strain,
- $k_X$  and  $c_X$ , governing the tensile-compressive asymmetry of the orientation stress thresholds,
- $k_h$  and  $c_h$ , governing the asymmetry of strain hardening.

All the parameters that come from the original ZM model are determined following the procedure described in [Zaki and Moumni, 2007a]:

- $C(T)$  is assumed to be taken as the same linear function of temperature as in (2.2),
- $E_M$ ,  $Y$ ,  $\alpha$ , and  $\beta$  are determined from a martensite orientation experiment in tension,
- $E_A$ ,  $a$ ,  $b$ ,  $G$ ,  $\kappa$ , and  $\xi$  are determined from a tensile pseudoelastic experiment.

The parameters introduced to account for asymmetric behavior are defined in terms of the following ratios:

$$r_{ori} = \frac{\gamma_t}{\gamma_c}, \quad r_X = \frac{\sigma_{rs,t}}{\sigma_{rs,c}}, \quad \text{and} \quad r_h = \frac{h_t}{h_c}, \quad (3.26)$$

where  $\gamma_c$  is the maximum orientation strain in compression,  $\sigma_{rs,t}$  and  $\sigma_{rs,c}$  are the critical stresses for martensite orientation and  $h_t$  and  $h_c$  are the strain hardening moduli in tension and in compression respectively.

•  $k_{ori}$  and  $c_{ori}$  are defined such that orientation strain has a maximum of  $\gamma_t$  in tension and  $\gamma_c$  in compression. They are given by:

$$k_{ori} = \left( \left( \frac{3}{4} \right)^{3/2} - \frac{c_{ori}}{4} \right)^{-1}, \quad (3.27)$$

$$c_{ori} = \frac{3}{2} \frac{(r_{ori}^3 - 1) \sqrt{3}}{r_{ori}^3 + 1}. \quad (3.28)$$

The Von-Mises equivalent strain is obtained for  $c_{ori} = 0$ .

•  $k_X$  and  $c_X$  are determined such that the tensile and compressive thresholds are respectively equal to  $\sigma_{rs,t}$  and  $\sigma_{rs,c}$ . They are given by:

$$k_X = \left( \left( \frac{1}{3} \right)^{3/2} - \frac{2c_X}{27} \right)^{-1}, \quad (3.29)$$

$$c_X = \frac{3}{2} \frac{(r_X^3 - 1) \sqrt{3}}{r_X^3 + 1}. \quad (3.30)$$

•  $k_h$  and  $c_h$  are related to the hardening moduli for martensite orientation.  $c_h$  is obtained by solving the following equation:

$$r_h = \frac{\left(\frac{3\sqrt{3}}{4} - c_h\right)}{\left(\frac{3\sqrt{3}}{4} + c_h\right)} \sqrt[3]{\frac{\left(\frac{3\sqrt{3}}{2} + c_h\right)}{\left(\frac{3\sqrt{3}}{2} - c_h\right)}}, \quad (3.31)$$

and  $k_h$  is given by:

$$k_h = \left( \left( \frac{3}{4} \right)^{3/2} - \frac{c_h}{4} \right)^{-1}. \quad (3.32)$$

### 3.3 VALIDATION

The validation of the extended model uses the experimental results from [Orgeas and Favier \[1998\]](#). Two different validations are proposed. First, the model is validated at a given temperature for tensile and compressive pseudoelasticity and martensite orientation. Parameters are chosen so that the convexity condition is verified. Second, using the same parameters, the extended ZM model is compared to the model proposed by [Orgeas and Favier \[1998\]](#) in terms of prediction of the direct phase change yield stress.

#### 3.3.1 Comparison with experimental results

The validation of the extended model is restricted to the uniaxial case. The structure is a beam with one end cantilevered and the other subjected to an imposed stress  $\sigma_0(t)$ , which is varied in time to control loading (*cf.* Fig. 32). Moreover, it is assumed that the critical stresses for phase change are sufficiently high so that maximum orientation is achieved as soon as phase change is activated. The constitutive equations are solved using Matlab. The assumption of uniaxiality simplifies the integration of the equilibrium equation  $\frac{\partial \sigma}{\partial x} = 0$  to obtain an explicit value for the stress, taking into account the Newton boundary condition  $\sigma = \sigma_0(t)$  at the end where loading is imposed. The experimental curves from Figs. 30 and 31 are used to validate the uniaxial model,

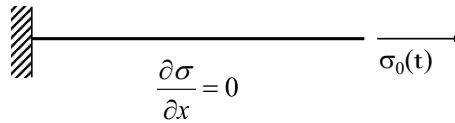


Figure 32. Geometry and boundary conditions of the problem

whose parameters are determined as described in section 3.2.3 and listed in Table 6<sup>1</sup>.

<sup>1</sup>  $r_{ori} = 1.74 \Leftrightarrow c_{ori} = \frac{3\sqrt{3}}{4}$ . All equivalent expressions satisfy the convexity condition 3.13.

Parameters values			
$E_A$	61000 MPa	$a$	11.310 MPa
$E_M$	35000 MPa	$b$	11.150 MPa
$\nu$	0.3	$G$	15.126 MPa
$\alpha$	456.08 MPa	$\beta$	4560.8 MPa
$Y$	243 MPa	$A_f^0$	55 °C
$\xi$	0.5 MPa/°C	$\kappa$	3.3190 MPa
$\gamma_t$	5.92 %	$r_{ori}$	1.74
$c_h$	1.299	$k_h$	3.290
$c_\chi$	-0.4142	$k_\chi$	4.482

Table 6. Model parameters

The experimental curves for pseudoelasticity were obtained for  $T = 60^\circ\text{C}$ , more details can be found in [Orgeas and Favier, 1998]. A comparison between experimental and numerical simulation data using the extended model is shown in Fig. 33 for superelasticity and in Fig. 34 for martensite orientation. Only three curves are used to determine the parameters of the model, the pseudoelastic curve in compression is used for validation.

The differences between the predictions of the model and experimental data are essentially due to differences in maximum tensile orientation strains for superelasticity and martensite orientation. These quantities are assumed to be equal even though experimental observation shows them to be slightly different. The thresholds for phase change and for martensite orientation and the slopes of the stress-strain curves are correctly estimated by the model.

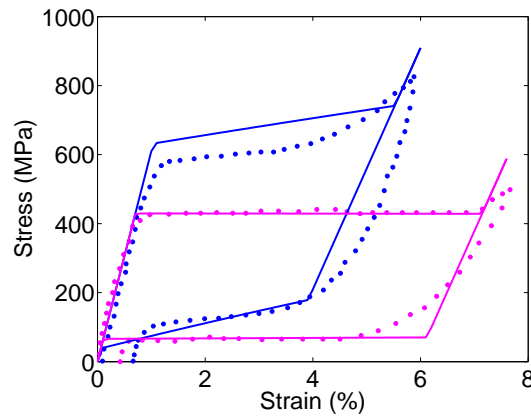


Figure 33. Simulated (solid lines) vs. experimental (circles) superelastic stress-strain curves in tension (pink) and in compression (blue).

### 3.3.2 Comparison with the phase change yield function of Orgeas and Favier [1998]

We now compare the predictions of the direct phase change yield stress given by our criterion and by the Orgeas and Favier [1998]'s criterion at different temperatures with experimental data.

Orgeas and Favier [1998] used a Raniecki and Mroz function to describe the direct phase change yield function; indeed, their criterion may be written in terms of the Lode invariants as:

$$\mathcal{F}(r, y) = r(1 + \gamma_0 y)^{n_0} - Q_{\sigma_{\text{crio}}} \leq 0, \quad (3.33)$$

with  $\gamma_0 = 0.9$ ,  $n_0 = 0.1$  and  $Q_{\sigma_{\text{crio}}}$  being a linear function of temperature with a slope of 7.5 MPa/K. This function satisfies the convexity condition (3.7).

Using the experimental yield stresses for tension, compression and shear loadings with respect to temperature given by Orgeas and Favier [1998] (cf. Fig. 7 of their article), we compare the predicted yield stresses for both criteria. However, the comparison is limited to temperatures higher than 303 K to ensure pseudoelastic response of the specimen. For our criterion, the yield stresses are computed from  $\mathcal{F}_z^1 = 0$  (cf. Eq. (3.20)), assuming that the orientation strain tensor is parallel to the stress deviator and is completely oriented. For the criterion from Orgeas and Favier [1998], the yield stresses are given by:

- in tension, as  $y = 1$ ,

$$\sigma = \frac{Q_{\sigma_{\text{crio}}}}{(1 + \gamma_0)^{n_0}}, \quad (3.34)$$

- in compression, as  $y = -1$ ,

$$\sigma = \frac{Q_{\sigma_{\text{crio}}}}{(1 - \gamma_0)^{n_0}}, \quad (3.35)$$

- in shear, as  $y = 0$ ,

$$\tau = \frac{Q_{\sigma_{\text{crio}}}}{\sqrt{2}}. \quad (3.36)$$

The comparison is plotted in Fig. 35. Our criterion is able to predict with very good accuracy the different yield stresses in pseudoelasticity. For more precise comparisons, the sum of square distances between criterion ( $\sigma_{\text{crit}}$ ) and experimental ( $\sigma_{\text{exp}}$ ) values are computed for each criterion and divided by the number of values considered:

$$\Delta = \frac{1}{n} \sqrt{\sum_{i=1}^n \left( \frac{\sigma_{\text{crit}}}{\sigma_{\text{exp}}} - 1 \right)^2} \quad (3.37)$$

The results are reported in Table 7. Our criterion seems to give better values than the one from Orgeas and Favier [1998].

## 3.4 CONCLUSION

The mathematical framework of Raniecki and Mroz was used to generalize the ZM model for shape memory alloys. The generalized model now accounts for tension-compression asymmetry through the use of non-even functions to define equivalent stresses and strains instead of using

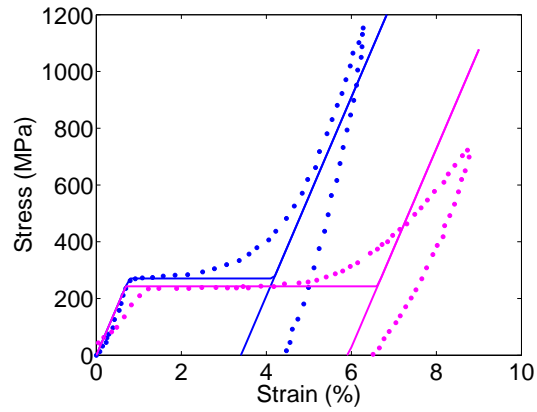


Figure 34. Simulated (solid lines) vs. experimental (circles) stress-strain curves in tension (pink) and in compression (blue) for martensite orientation.

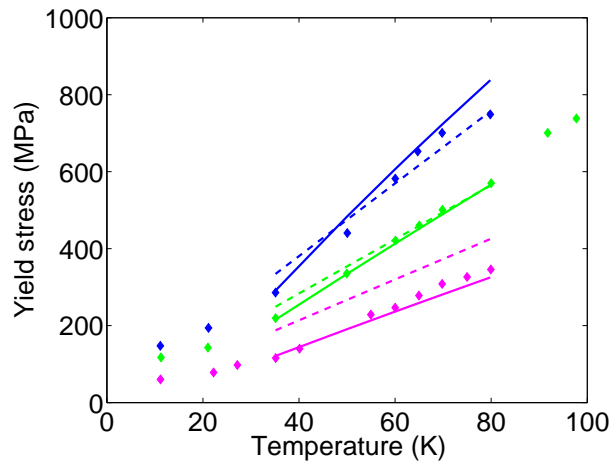


Figure 35. Comparison of the prediction of the direct phase change yield stresses in tension (green), compression (blue) and shear (pink) given by the criterion of Orgeas and Favier (dotted line) and by our criterion (solid line) with experimental data from Orgeas and Favier (markers).

	Tension	Compression	Shear
Modified ZM model	1.17 %	2.75 %	2.20 %
Orgeas and Favier's criterion	2.23 %	3.43 %	12.80 %

Table 7. Deviation of the different criteria with experimental data.

standard Von Mises equivalents. The model is validated in uniaxial tension and compression, where it shows good agreement with experimental data both for superelasticity and martensite orientation. Moreover, good yield stress values are predicted for shear loading.

To our knowledge, this is the first time that a phenomenological model is able to reproduce tensile-compressive asymmetry for 3D loadings in both pseudoelasticity and martensite orientation. Indeed, our model accounts for the different characteristics listed by Wasilewski [1971] and reproduces with good accuracy the variation of the yield stresses with respect to temperature for tensile, compressive and shear loadings. Work is underway to validate the model in 3D, namely for non-proportional tensile-torsional and compressive-torsional loadings.

With this extension of the model, a more accurate prediction of the stabilized cycle is achieved. However, this prediction will be shown to be valid only for very low strain rates. Indeed, the presence of a latent heat of phase change and the dependence of the phase change yield stresses on temperature modify the response of the SMA with strain rate... This is the topic of the next chapter.

# 4

## THERMOMECHANICAL COUPLING

---

4.1	Experimental evidence of thermomechanical coupling in SMA	61
4.1.1	Strain rate dependence	61
4.1.2	Influence of geometry and heat boundary conditions	62
4.1.3	Cyclic evolution	62
4.2	Literature review of the thermomechanical modelling	63
4.2.1	Main ideas of the macroscopic modeling	63
4.2.2	The different models	64
4.3	Introducing the thermomechanical coupling in the ZM model	65
4.3.1	Derivation of the heat equation	65
4.3.2	Position of the problem and getting the discrete equations	66
4.4	Results and interpretation	68
4.4.1	Experimental validation	70
4.4.2	Influence of the different heat sources	74
4.4.3	Influence of geometry and boundary conditions on hysteresis area	74
4.5	Extension to the cyclic behavior	76
4.5.1	Experimental investigation	76
4.5.2	Modelling	84
4.5.3	Validation of the coupled model	85
4.6	Conclusion	92

---

Most of the models currently available for shape memory materials do not account for strong thermomechanical coupling, even though the sensitivity of the mechanical behavior of SMAs to temperature is a commonly accepted fact. Thermomechanical coupling in SMAs is generally explained by the martensitic phase change being a first-order transformation that absorbs/releases latent heat. For example, during a pseudoelastic cycle, the direct phase change is exothermic: the latent heat is released to the surroundings. If the heat exchange with the surroundings is not sufficient, the released heat causes an increase of the material temperature. During unloading, the reverse phase change is endothermic resulting in an absorption of latent heat and causing a temperature decrease if heat exchange with the surroundings is not sufficient [*cf.* [Van Humbeeck and Delaey, 1981](#); [Shaw and Kyriakides, 1995](#); [Zhu and Zhang, 2007](#)]. Temperature variations spark off changes in the mechanical response of the material, as explained by [Ortin and Planes \[1989\]](#):

- During forward phase change, the temperature of the SMA increases due to heat generation. As a result, austenite becomes more stable and higher stress is required to drive the formation of martensite forward.
- During reverse phase change, because latent heat is predominant, the temperature of the SMA decreases making martensite more stable. Stress must then be decreased further for the reverse transformation to continue.

Temperature variations depend on heat exchange conditions and thus, the SMA mechanical response may depend on geometry and/or strain rate. Therefore, accounting for thermomechanical coupling is required for accurate modeling of SMA behavior.

This chapter is organized as follows: in the first section, detailed literature review on experimental evidence of thermomechanical coupling is given. The second section reviews the different modellings that account for it. The third section shows how to introduce it in the ZM model and gives the associated algorithm, while the fourth section is devoted to the discussion of the results. Finally, the fifth section is an extension to cyclic loadings, with experimental and modelling results.

## 4.1 EXPERIMENTAL EVIDENCE OF THERMOMECHANICAL COUPLING IN SMA

This section provides an overview of key experimental results available in literature, dealing with thermomechanical coupling in Shape Memory Alloys.

### 4.1.1 Strain rate dependence

[Van Humbeeck and Delaey \[1981\]](#) seem to have pioneered the investigation on the influence of strain rate on the superelastic response of Copper-based SMAs. Their experiments, conducted at ambient temperature in air, show a clear dependence on strain rate of the forward transformation stress. They also show that the variation of the hysteresis area and the difference between the forward and reverse transformation plateaus evolve non-monotonously with strain rate, with maximum hysteresis occurring at intermediate rates. The authors explain this behavior by the thermomechanical coupling in material behavior and the exchange of heat with the surroundings. They argue that, at high loading rate, a larger portion of the phase transformation heat goes into heating the material. The increase in temperature increases the stress onset for forward transformation and the slope of the tensile curves. For the highest strain rates, temperature within the material is always higher than ambient temperature because of smaller heat exchange. Consequently, the stress threshold for reverse phase change is higher than the one obtained for isothermal experiment. Inversely, at intermediate strain rates, temperature increases above ambient during direct phase change and becomes lower than ambient during reverse phase change. Thus, the stress threshold for reverse phase change is smaller than the isothermal one. This results in an increase of the hysteresis area at medium strain rates followed by a decrease at higher strain rates. [Mukherjee et al. \[1985\]](#) made similar observations in the case of NiTi SMAs. The influence of strain rate is found to depend on the position of the four transformation temperatures compared to the temperature during the experiment. This is also used to explain the presence of residual strain for some experimental setups. Moreover, the authors show that, if the loading cycle is paused, the onset of phase transformation will return to its isothermal value. (*cf.* Fig. 3 and 4 of [Mukherjee et al., 1985](#)). A thorough experimental study on strain-rate dependence is given by [Shaw and Kyriakides \[1995\]](#). The authors report higher amplitude of temperature variation during a loading cycle for higher strain rates. The explanation they provide is similar to the one given by [Van Humbeeck and Delaey \[1981\]](#). Similar results are also reported by [Leo et al. \[1993\]](#) and by [He et al. \[2010\]](#). The variation of the area of the hysteresis loop with strain rate can be explained by the relative position of the isothermal and non isothermal reverse phase change plateaus. Indeed, if the strain rate is moderate, temperature increases during forward phase change, but falls below the ambient value during the endothermic reverse phase change. The resulting reverse phase change plateau is thus partly above and partly below the isothermal plateau, and the hysteresis area increases. For higher strain rates, however, the increase in temperature is such that the reverse transformation plateau remains above the isothermal plateau,

which decreases the area of the hysteresis loop. Finally, [McCormick et al. \[1993\]](#) show that the amplitude of temperature variation saturates at sufficiently high strain rates.

#### 4.1.2 Influence of geometry and heat boundary conditions

Several authors carried out experiments on SMA samples in air and in water in order to understand the influence of the heat exchange coefficient on the way strain rate influences SMA response. [McCormick et al. \[1993\]](#) showed that, for test samples submerged in water, a significantly higher strain rate was required to obtain a sensible variation of the hysteresis area. This was explained by the higher value of the heat transfer coefficient in this case. [Shaw and Kyriakides \[1995\]](#) reported similar experimental observations for a range of experiments conducted in both air and water. They conclude that high strain rates and poor heat exchange with the surroundings lead to excessive heating and distort the stress-strain curve. [Leo et al. \[1993\]](#) also found that the increase of the hysteresis area with strain rate is reduced by higher heat transfer between the surrounding medium and the specimen. Similar conclusions are given by [He et al. \[2010\]](#) for experiments conducted in air; the variation in the heat transfer coefficient is achieved in this case by changing the air flow around the SMA sample. It was found that the strain rate, for which area of the hysteresis loop is maximal, increases with increased air convection. The authors justify their findings by comparing two characteristic times: maximum hysteresis area is achieved when the characteristic time of phase transition (characteristic of the material) is approximately equal to the characteristic time of heat transfer time (which depends on the boundary conditions). Recently, [Grabe and Bruhns \[2008\]](#) developed an experimental setup allowing precise control of the temperature of the sample and used it to conduct isothermal experiments at different strain rates. They found that the stress-strain response of the SMA is not modified when the strain rate is varied. The authors also performed relaxation tests which showed that no stress relaxation occurs within the material. They concluded that the viscosity of SMAs is negligible. [Piedboeuf et al. \[1998\]](#) analyzed the effect of thermomechanical coupling on the dynamic response of SMAs, with focus on the effect of strain amplitude, frequency and temperature on their damping behavior. Within the same context, [Heller et al. \[2009\]](#) attributed the variation of the superelastic damping capacity of SMAs with strain rate to the thermal effects associated with martensitic transformations.

#### 4.1.3 Cyclic evolution

Since components made of SMAs usually operate under cyclic thermomechanical loading, their design requires reliable prediction of the material's cyclic three-dimensional response and fatigue resistance. To this end, several authors performed cyclic experiments in order to emphasize the influence of heat transfer on the cyclic response. [Zhu and Zhang \[2007\]](#) studied the strain rate dependence for the cyclic behavior of SMA. To this aim, they performed cyclic experiments on SMA wires which had been previously trained in order to remove all effects of microstructure degradation. In the experiments, the first temperature cycles are not stable, because the heat generated during a complete cycle by mechanical dissipation is different from the heat lost to the surrounding medium. Consequently, the start and finish temperatures are not equal, and the yield stress required to start the direct transformation of the next cycle is different from the previous one: even for trained materials, thermomechanical coupling leads to a variation of the stress-strain response while cycling at a given strain rate. However, after a few cycles, thermal equilibrium is reached, and the start and finish temperatures become identical for all subsequent cycles, resulting in a stabilization of the mechanical response, which depends on the strain rate. The increase of the temperature amplitude with the strain rate has also been reported by [Tobushi et al. \[1997\]](#), who studied the dependence of fatigue on the loading fre-

quency for NiTi wires. Similar observations are made by [McCormick et al. \[1993\]](#). [Paradis et al. \[2008\]](#) studied the origin of the pause effect on SMA response; namely, when SMA structures are subject to interrupted cyclic loadings, a transient phase is observed as if the material returns to a training phase. It seems also that this pause effect has an influence on the fatigue life of SMAs. They showed that the pause effect may be attributed to the thermal evolution of the specimen: during the pause, the specimen temperature returns to the ambient temperature. This gives rise to an increase of the dissipated energy just after the pause, until the specimen is in thermal equilibrium, as shown by [Zhu and Zhang \[2007\]](#). In this thermal equilibrium, the dissipated energy has the same value as before the pause. During the pause, a part of the residual strain disappears, which tends to prove that this part of the residual strain is due to a thermal effect (a similar observation was made by [Mukherjee et al. \[1985\]](#)). [He and Sun \[2010\]](#) established some general tendencies for temperature evolution during cyclic loading: whatever the loading rate, a stabilized thermal cycle is always reached. Its temperature amplitude is increased when the loading frequency is increased, but reaches a saturated value for high strain rates; its mean temperature follows the same evolution. They developed a simple 1D analytical model to study the cyclic evolution of temperature with strain rate. They divided each loading cycle into five steps: during elastic steps, only heat convection leads to temperature change, whereas during phase change steps, both latent heat and convection determine the temperature evolution. Their simulations show that the higher the strain rate, the higher the number of cycles required to reach an equilibrium state. Moreover, for higher strain rates, the mean stabilized temperature is higher than the ambient temperature. On the one hand, the saturated amplitude of temperature at high strain rates may be estimated with the latent heat, the heat capacity and the mechanical dissipation. On the other hand, the temperature amplitude for each strain rate depends on the mechanical dissipation, the heat capacity and on the ratio between the loading period and the characteristic time for heat convection, as the amount of heat transferred to the surroundings is exactly equal to the mechanical dissipation.

To our knowledge, no experimental investigation has been carried during the training phase of SMAs.

## 4.2 LITERATURE REVIEW OF THE THERMOMECHANICAL MODELLING

This section is devoted to the presentation of the different models in the literature that take into account thermomechanical coupling.

### 4.2.1 Main ideas of the macroscopic modeling

Only few models take into account the thermomechanical coupling described in the previous part. Most of the models accounting for thermomechanical coupling have three sets of equations:

- The first set of equation consists of the stress-strain relation, which can be written (either for 1D or 3D models) as [cf. [Auricchio and Sacco, 2001](#); [Vitiello et al., 2005](#); [Kadkhodaei et al., 2007](#); [Zhu and Zhang, 2007](#)]:

$$\boldsymbol{\sigma} = \mathbf{K} : (\boldsymbol{\epsilon} - z\boldsymbol{\epsilon}_{\text{ori}}), \quad (4.1)$$

where  $\mathbf{K}$  is the elasticity tensor,  $z$  is the volume fraction of martensite, and  $\boldsymbol{\epsilon}_{\text{ori}}$  is an orientation strain tensor.

- The second set consists of an evolution law for the martensite volume fraction:

$$\dot{z} = f(\boldsymbol{\sigma}, z, T). \quad (4.2)$$

- The third set is an energy balance.

$$\rho C_p \dot{T} + \text{div } \mathbf{q} = \mathbf{b} \quad (4.3)$$

$$\mathbf{q} \cdot \mathbf{n} = h (T - T_{\text{ext}}). \quad (4.4)$$

In these equations,  $\text{div}$  stands for the divergence operator,  $\mathbf{q}$  is the heat flux,  $\mathbf{n}$  the normal vector to the surface,  $C_p$  is the heat capacity,  $\mathbf{b}$  is the heat source: two major heat sources are accounted for: the latent heat of phase change and the mechanical dissipation. Only [Entemeyer et al. \[2001\]](#) proposed a model which does not account for mechanical dissipation; it is based on the findings of [Peyroux et al. \[1998\]](#), who argued that the mechanical dissipation is zero. In a number of other models [cf. [Auricchio and Sacco, 2001](#); [Kadkhodaei et al., 2007](#); [Vitiello et al., 2005](#); [Zhu and Zhang, 2007](#)], the mechanical dissipation was always accounted for. Finally, heat is assumed to be exchanged with the surroundings by convection and  $h$  is the convective heat transfer coefficient.

#### 4.2.2 The different models

[Auricchio and Sacco \[2001\]](#) developed a 1D model using the theory of irreversible thermodynamics. The orientation strain is a scalar, identical for tension and compression. Their stress relation accounts for thermal expansion. Consequently, the heat equation has an extra heat source, the thermoelastic effect. The evolution equations were chosen to be linear and were numerically solved using a backward Euler scheme. Their model is able to reproduce qualitatively the experimental observations made by [Lim and McDowell \[2002\]](#): variation of the phase change plateaus with the strain rate, non monotonic variation of the hysteresis loop and temperature variations. They also obtained the same tendencies for cyclic loadings, with a different stabilized mean temperature according to the strain rate. [Vitiello et al. \[2005\]](#) employed the Tanaka's model [cf. [Tanaka et al., 1986](#); [Brinson and Huang, 1996](#)] reduced to 1D to describe the stress-strain relation and the evolution of the internal variables. The energy balance has two heat sources, which are latent heat (because of martensite or austenite production) and mechanical dissipation (linked to internal friction). They compare the prediction of the model with experimental results they obtain on 1 mm-diameter wire subjected to tensile loadings at different frequencies. They neglect the thermal expansion before latent heat. The model gives very good agreement at low strain rate for the stress-strain curve, and the accuracy decreases for higher strain rates ( $0.5 \text{ s}^{-1}$ ) but remains reasonable. The discrepancies are explained by the assumption of a constant heat generation during phase change, and a constant heat transfer coefficient. [Kadkhodaei et al. \[2007\]](#) propose a 1D model based on the Brinson model [cf. [Brinson, 1993](#)] for the martensite volume fraction evolution law. Their energy balance is obtained from the first principle where thermal expansion, mechanical dissipation and latent heat are considered. The convective heat transfer coefficient depends on temperature using different empirical relations. However, these relations were obtained for stationary regimes but are employed for variable regime. The comparison of the different relations shows that it is possible to reproduce the strain rate dependence on the hysteresis area with good accuracy for both mechanical and thermal responses. The effect of geometry and cyclic behavior is investigated without providing experimental validation. With regard to cyclic loadings, the authors reproduce the stabilization of the mechanical and thermal responses after a few cycles. [Zhu and Zhang \[2007\]](#) investigated the evolution of the cyclic SMA response for trained materials. Their model is a Voigt model coupled with an energy balance, where two heat sources are taken into account: latent heat and intrinsic dissipation. The complete set of equations is solved simultaneously using a fourth-order Runge-Kutta method. Their model is able to reproduce qualitatively and quantitatively with reasonable accuracy the experimental results previously described. Changes of phase transformation plateaus and hysteresis area are correctly reproduced, even if the increase of the slopes is higher in the experiments than

in their predictions. The tendencies of temperature variations are captured. The model is also able to reproduce partial martensitic transformation.

The aim of this chapter is to propose extension of the ZM models to account for thermomechanical coupling, which are 3D models, whereas the majority of the coupled models are 1D and do not always propose experimental validation. Moreover, it seems to be an important aspect for fatigue design, as it leads to important modifications of the mechanical response (maximum stress, size of the hysteresis area) as well as to dependence of the response on geometrical parameters or on heat exchange conditions.

### 4.3 INTRODUCING THE THERMOMECHANICAL COUPLING IN THE ZM MODEL

This section details the obtention of the coupled problem as well as the algorithm needed for numerical resolution.

#### 4.3.1 Derivation of the heat equation

##### *Heat capacity*

The Helmholtz free energy  $\mathcal{W}$  as defined in Eq. (2.1) does not include a heat capacity. This shortcoming is addressed here by introducing a constant specific heat capacity  $C_p$ , the same for austenite and martensite, such that the free energy  $\mathcal{W}$  of the SMA can be written as

$$\begin{aligned} \mathcal{W} = & (1-z) \left[ \frac{1}{2} \epsilon_A : \mathbf{K}_A : \epsilon_A \right] + z \left[ \frac{1}{2} (\epsilon_M - \epsilon_{\text{ori}}) : \mathbf{K}_M : (\epsilon_M - \epsilon_{\text{ori}}) + C(T) \right] \\ & + G \frac{z^2}{2} + \frac{z}{2} [\alpha z + \beta (1-z)] \left( \frac{2}{3} \epsilon_{\text{ori}} : \epsilon_{\text{ori}} \right) + \rho C_p \left( T - T_0 - T \ln \left( \frac{T}{T_0} \right) \right), \end{aligned} \quad (4.5)$$

$\rho$  being the mass density of the alloy and  $T_0$  being a reference temperature. The assumption that austenite and martensite have the same heat capacity simplifies the derivation of the constitutive equations. Indeed, only the state equation for entropy is modified in this case with respect to the original ZM model. If the heat capacity were dependent on the composition of the SMA, the expression of the thermodynamic force driving phase change and, consequently, the yield functions governing phase change would have been modified.

##### *Heat equation*

The introduction of a heat capacity modifies the state equation for entropy, which becomes

$$s = -\frac{\partial \mathcal{L}}{\partial T} = \rho C_p \ln \left( \frac{T}{T_0} \right) - \xi z. \quad (4.6)$$

The expression of the intrinsic dissipation is obtained in Appendix A (Eq. (A.15)). Developing the time derivative of the Helmholtz free energy, the intrinsic dissipation becomes:

$$\mathcal{D}_1 = \mathcal{A}_z \dot{z} + \mathcal{A}_{\text{ori}} : \dot{\epsilon}_{\text{ori}} \geq 0, \quad (4.7)$$

because the strain is not a dissipative mechanism. The intrinsic dissipation  $\mathcal{D}_1$  can also be written in terms of the Lagrangian  $\mathcal{L}$  as follows:

$$\begin{aligned}\mathcal{D}_1 &= T\dot{s} + \operatorname{div} \mathbf{q} - r \\ &= -T \frac{\partial^2 \mathcal{L}}{\partial T \partial \epsilon} : \dot{\epsilon} - T \frac{\partial^2 \mathcal{L}}{\partial T \partial \epsilon_{\text{ori}}} : \dot{\epsilon}_{\text{ori}} - T \frac{\partial^2 \mathcal{L}}{\partial T \partial z} \dot{z} - T \frac{\partial^2 \mathcal{L}}{\partial T^2} \dot{T} + \operatorname{div} \mathbf{q} - r.\end{aligned}\quad (4.8)$$

The first term on the right hand side accounts for thermoelastic effects and will be neglected. The second term accounts for coupling due to the orientation of martensite, the third accounts for latent heat and the fourth for heat capacity. Using Fourier's law of heat conduction,  $\mathbf{q} = -k\nabla T$ , and assuming the thermal conductivity  $k$  to be identical for austenite and martensite, the heat equation is obtained:

$$\rho C_p \dot{T} - \operatorname{div} (k\nabla T) = -T \frac{\partial \mathcal{A}_{\text{ori}}}{\partial T} : \dot{\epsilon}_{\text{ori}} - T \frac{\partial \mathcal{A}_z}{\partial T} \dot{z} + r + \mathcal{D}_1. \quad (4.9)$$

Here, only the heat generated by phase change is taken into account, because proportional loadings are assumed for simplicity. As a consequence, heat generation due to martensite orientation is null. If, moreover, phase change is considered to be the only dissipative mechanism, Eq. (4.9) becomes

$$\rho C_p \dot{T} - \operatorname{div} (k\nabla T) = -T \frac{\partial \mathcal{A}_z}{\partial T} \dot{z} + \mathcal{A}_z \dot{z}. \quad (4.10)$$

Because  $\mathcal{A}_z$  is taken as a sub-gradient of the pseudopotential of dissipation and because the pseudo-potential is homogeneous of degree one, the dissipation  $\mathcal{A}_z \dot{z}$  is equal to  $[a(1-z) + bz]|\dot{z}|$ , whence the equation

$$\rho C_p \dot{T} - \operatorname{div} (k\nabla T) = T \frac{\partial C(T)}{\partial T} \dot{z} + [a(1-z) + bz]|\dot{z}|. \quad (4.11)$$

The heat equation is coupled with metallurgical equation via the evolution of the martensite volume fraction. It is thus necessary to develop a coupled resolution of the whole set of equations.

#### 4.3.2 Position of the problem and getting the discrete equations

In this section, the complete coupled problem is presented, and the heat equation is discretized to get a finite element formulation.

##### *Sets of equations to be solved: strong thermomechanical coupling*

The problem consists of computing the thermomechanical response of a superelastic shape memory alloy structure occupying a volume  $\Omega$ , assuming infinitesimal transformations and quasi static loading. The structure is subject to a distribution of body forces  $\mathbf{f}$  over  $\Omega$  and contact forces  $\mathbf{T}_d$  over part of the boundary  $\partial\Omega_T$ ; displacement boundary conditions are prescribed on the remaining part  $\partial\Omega_\xi$ . Convective heat transfer is considered between the structure and its surroundings.

The behavior of the structure can be determined by solving the following equations:

- Static and kinematic admissibility

$$\operatorname{div} \boldsymbol{\sigma} = \mathbf{f} \text{ in } \Omega \quad (4.12)$$

$$\boldsymbol{\xi} = \boldsymbol{\xi}_d \text{ in } \partial\Omega_\xi \quad (4.13)$$

$$\boldsymbol{\sigma} \cdot \mathbf{n} = \mathbf{T}_d \text{ in } \partial\Omega_T \quad (4.14)$$

- Strain compatibility

$$\epsilon = \frac{1}{2} (\nabla \xi + {}^t \nabla \xi) \text{ in } \Omega \quad (4.15)$$

- Constitutive equations for proportional loadings (cf. section 2.4.2 for further details on the simplifications for proportional loadings):

$$\sigma = \mathbf{K} : (\epsilon - z\gamma\epsilon_0) \text{ in } \Omega \quad (4.16)$$

where the evolution of  $z$  is governed by the phase change yield functions  $\mathcal{F}_z^1$  and  $\mathcal{F}_z^2$  (cf. Eqs. (2.15) and (2.16), and  $\epsilon_0$  is defined by Eq. (2.65).

- Heat equation

$$\rho C_p \dot{T} - \operatorname{div}(\mathbf{k} \nabla T) = T \frac{\partial C(T)}{\partial T} \dot{z} + [a(1-z) + bz] |\dot{z}| \text{ in } \Omega, \quad (4.17)$$

$$\mathbf{q} \cdot \mathbf{n} = h(T - T_{\text{ext}}) \text{ in } \partial\Omega, \quad (4.18)$$

$$T(t=0) = T_{\text{ext}}, \quad (4.19)$$

where  $h$  is the convective heat transfer coefficient.

#### Discrete heat equation

The discretization of mechanical equations has already been presented in section 2.4 and only requires spatial discretization. Solving the heat equation requires time and space discretization. Using Stokes' theorem, the following weak form can be obtained for the heat equation:

$$\begin{aligned} & \int_{\Omega} \rho C_p \dot{T} w \, dV + \int_{\Omega} \mathbf{k} \nabla T \cdot \nabla w \, dV - \int_{\partial\Omega} \mathbf{k} \nabla T \cdot \mathbf{n} w \, dS \\ &= \int_{\Omega} \xi \dot{z} T w \, dV + \int_{\Omega} [a(1-z) + bz] |\dot{z}| w \, dV \end{aligned} \quad (4.20)$$

where  $w$  is a test function taken to be equal to zero on the boundaries where temperature is prescribed. Considering convective heat transfer only, the heat flux through the boundary is given by  $\mathbf{q} \cdot \mathbf{n} = h(T - T_{\text{ext}}) = -\mathbf{k} \nabla T \cdot \mathbf{n}$ . Substituting into Eq. (4.20) gives

$$\begin{aligned} & \int_{\Omega} \rho C_p \dot{T} w \, dV + \int_{\Omega} \mathbf{k} \nabla T \cdot \nabla w \, dV + \int_{\partial\Omega} h T w \, dS \\ &= \int_{\Omega} \xi \dot{z} T w \, dV + \int_{\Omega} [a(1-z) + bz] |\dot{z}| w \, dV + \int_{\partial\Omega} h T_{\text{ext}} w \, dS. \end{aligned} \quad (4.21)$$

The above equation can be arranged in the following form:

$$(\mathbf{C} + \mathbf{C}_1 + \mathbf{C}_h) \cdot \mathbf{T} + \mathbf{M} \cdot \dot{\mathbf{T}} = \mathbf{Q}, \quad (4.22)$$

where  $\mathbf{C}$  is the conductivity matrix,  $\mathbf{C}_l$  is a latent heat matrix,  $\mathbf{C}_h$  is a convection matrix, and  $\mathbf{M}$  is a heat capacity matrix. These matrices can be calculated as follows,  $\phi_i$  and  $\phi_j$  being finite-element base functions:

$$\mathbf{C}_{ij} = \int_{\Omega} k \nabla \phi_i \cdot \nabla \phi_j \, dV, \quad (4.23)$$

$$(\mathbf{C}_l)_{ij} = - \int_{\Omega} \xi \phi_i \phi_j \dot{z} \, dV, \quad (4.24)$$

$$(\mathbf{C}_h)_{ij} = \int_{\partial\Omega} h \phi_i \phi_j \, dS, \quad (4.25)$$

$$\mathbf{M}_{ij} = \int_{\Omega} \rho C_p \phi_i \phi_j \, dV, \quad (4.26)$$

$$\mathbf{Q}_i = \int_{\Omega} [\alpha(1-z) + bz] |\dot{z}| \phi_i \, dV + \int_{\partial\Omega} h T_{\text{ext}} \phi_i \, dS. \quad (4.27)$$

Using first-order implicit differentiation, the following approximations are obtained:

$$(\mathbf{C}_l)_{ij}^{n+1} = \frac{-1}{\Delta t} \int_{\Omega} \xi \phi_i \phi_j (z_{n+1} - z_n) \, dV, \quad (4.28)$$

$$\mathbf{Q}_i^{n+1} = \frac{1}{\Delta t} \int_{\Omega} [\alpha(1 - z_{n+1}) + bz_{n+1}] |z_{n+1} - z_n| \phi_i \, dV + \int_{\partial\Omega} h T_{\text{ext}} \phi_i \, dS, \quad (4.29)$$

where  $\Delta t$  is the duration of the load increment. The implicit discrete heat equation can thus be written as

$$(\mathbf{C} + \mathbf{C}_l^{n+1} + \mathbf{C}_h) \cdot \mathbf{T}^{n+1} + \mathbf{M} \cdot \frac{\mathbf{T}^{n+1} - \mathbf{T}^n}{\Delta t} = \mathbf{Q}^{n+1}. \quad (4.30)$$

The temperature at increment  $n+1$  is then given by

$$\mathbf{T}^{n+1} = \left( \mathbf{C} + \mathbf{C}_l^{n+1} + \mathbf{C}_h + \frac{\mathbf{M}}{\Delta t} \right)^{-1} \cdot \left( \mathbf{Q}^{n+1} + \frac{\mathbf{M}}{\Delta t} \cdot \mathbf{T}^n \right). \quad (4.31)$$

Assuming the increment of volume fraction is known from a previous computation, this last equation allows the computation of the increment of temperature. Let us detail the complete coupled algorithm.

#### *Algorithm for the coupled problem*

Phase transformation thresholds in SMAs strongly depend on temperature, which is in turn influenced by intrinsic dissipation and latent heat exchange during phase change. This is accounted for by the equations in section 4.3, which can be solved using the algorithm in Table 8. In this algorithm,  $\mathbf{F}_{n+1}$  is the loading applied on the structure at the instant  $t_{n+1}$ , and  $\|\cdot\|$  is for instance the maximum norm over the second order tensor space.

## 4.4 RESULTS AND INTERPRETATION

This section presents some experimental validation and limitation of the model, using experimental results from literature. A study of the influence of the different heat sources is proposed, to understand the effect of each source on the mechanical as well as the thermal responses. Finally, the model is shown to reproduce qualitatively well the effect of geometry and of boundary conditions on the thermomechanical responses.

---

Input: model parameters,  $\sigma_n, z_n, T_n, F_{n+1}$ , three tolerances:  $\text{tol}_1, \text{tol}_2, \text{tol}_3$ .

Output:  $\epsilon_{n+1}, \sigma_{n+1}, z_{n+1}, T_{n+1}$ .

Set  $k = 0, z_{n+1}^{(0)} = z_n, T_{n+1}^{(0)} = T_n, S_{n+1}^{(0)} = S_n$ .

1. Compute the isothermal response:
    - a) Compute the displacement field by solving the equilibrium equation:  $\mathbf{K}(z_{n+1}^{(k)}) \cdot \mathbf{U}_{n+1}^{(k)} = F_{n+1}$ .
    - b) Compute the strain field:
 
$$\epsilon_{n+1}^{(k)} = \frac{1}{2} \left( \nabla \mathbf{U}_{n+1}^{(k)} + {}^t \nabla \mathbf{U}_{n+1}^{(k)} \right).$$
    - c) Thermoelastic prediction and return mapping algorithm:
      - i. Compute the thermoelastic prediction: Eq. (2.67) and evaluate the yield functions ( $i = 1, 2$ ):  $\mathcal{F}_{i,n+1}^{z,(k)} = \mathcal{F}_i^z(\sigma_{n+1}^{(k)}, z_{n+1}^{(k)}, T_{n+1}^{(k)})$ .
      - ii. If  $\mathcal{F}_{i,n+1}^{z,(k)} < 0$  (or during the iterations  $|\mathcal{F}_{i,n+1}^{z,(k)}| < \text{tol}_1$ ) then set  $k = k + 1$  and go to 1.(d).
      - iii. Compute the increment of the martensite volume fraction  $\Delta z_{n+1}^{(k+1)}$  (Eq. (2.73)).
      - iv. Update the state variables.
      - v. Set  $k = k + 1$  and go to 1.(c).
    - d) Compute the residual:  $\mathbf{R} = \mathbf{K}(z_{n+1}^{(k+1)}) \cdot \mathbf{U}_{n+1}^{(k+1)} - F_{n+1}$
    - e) If  $\|\mathbf{R}\| > \text{tol}_2$  then go to 1.(a).
  2. Compute the actual temperature by solving the heat equation (Eq. (4.31), in which  $T^n, T^{n+1}, z^n$  and  $z^{n+1}$  must be replaced by  $T_{n+1}^{(k)}, T_{n+1}^{(k+1)}, z_{n+1}^{(k)}$  and  $z_{n+1}^{(k+1)}$  resp.).
  3. If  $|T_{n+1}^{(k+1)} - T_{n+1}^{(k)}| > \text{tol}_3 T_{n+1}^{(k)}$  then go to 1.(a).
  4. End.
- 

Table 8. Algorithm for the thermomechanical coupled ZM model.

#### 4.4.1 Experimental validation

A superelastic NiTi cylinder, 1 mm in diameter and 100 mm in length, is clamped on one end and subject to controlled tensile displacement on the other end (*cf.* Fig. 36).

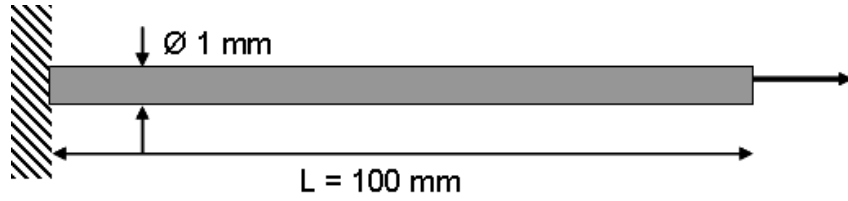


Figure 36. Geometry and boundary conditions of the specimen.

Four different loading rates are considered corresponding to strain rates of  $4 \cdot 10^{-5}$ ,  $4 \cdot 10^{-4}$ ,  $4 \cdot 10^{-3}$  and  $4 \cdot 10^{-2} \text{ s}^{-1}$  respectively. Experimental data from [Shaw and Kyriakides \[1995\]](#) are used to determine the parameters of the ZM model listed in Table 9.

Parameters values			
$E_A$	61500 MPa	$\alpha$	6.8920 MPa
$E_M$	24000 MPa	$b$	6.9091 MPa
$\nu$	0.3	$G$	4.6556 MPa
$\alpha$	2750 MPa	$\beta$	5500 MPa
$\gamma$	110 MPa	$A_f^0$	40 °C
$\xi$	0.2914 MPa/°C	$\kappa$	6.8920 MPa
$\gamma$	4.0 %	$k$	18 W.m <sup>-1</sup> .K <sup>-1</sup>
$C_p$	440 J.kg <sup>-1</sup> .K <sup>-1</sup>	$h_{\text{air}}$	50 W.m <sup>-2</sup> .K <sup>-1</sup>
$\rho$	6500 kg.m <sup>-3</sup>	$h_{\text{water}}$	800 W.m <sup>-2</sup> .K <sup>-1</sup>

Table 9. Model parameters

#### Presentation of the results

Figs. 37a, 38a, 39a and 40a show a comparison between experimental data taken from Shaw and Kyriakides and the simulations obtained using the model. In these figures, simulation results are shown in solid/dashed line and experimental data are shown using markers. The blue/red color indicates that the surrounding medium is water/air. Figs. 37b, 38b, 39b and 40b represent temperature-strain curves for the different strain rates.

In Fig. 41a, the maximum amplitude of temperature variation is plotted using simulation and experimental data. Error bars are used to indicate uncertainties on experimental measurements. The agreement between experimental and numerical results is measured using the ratio

$$\text{error} = \frac{|\text{ampl}_{\text{simul}} - \text{ampl}_{\text{exp}}|}{\text{ampl}_{\text{exp}}} \quad (4.32)$$

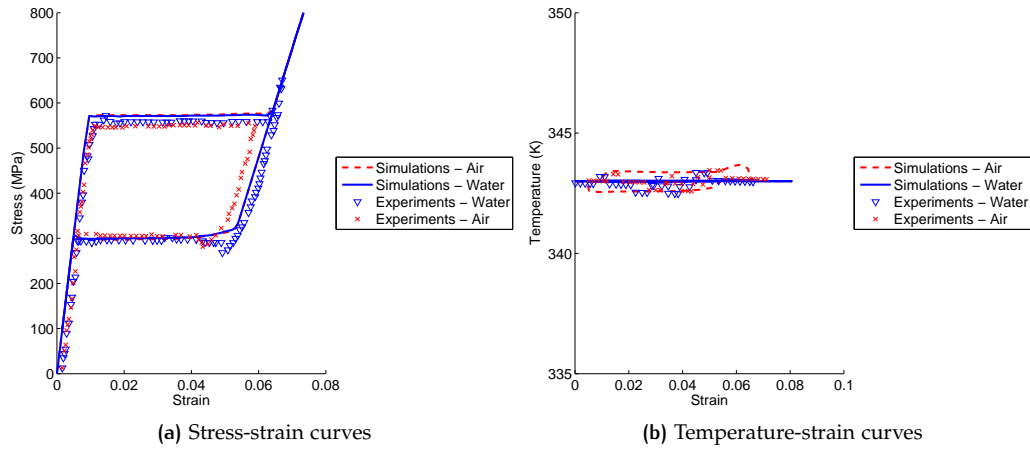


Figure 37. Experimental vs. numerical stress-strain and temperature-strain curves for a strain rate of  $4.10^{-5} \text{ s}^{-1}$ .

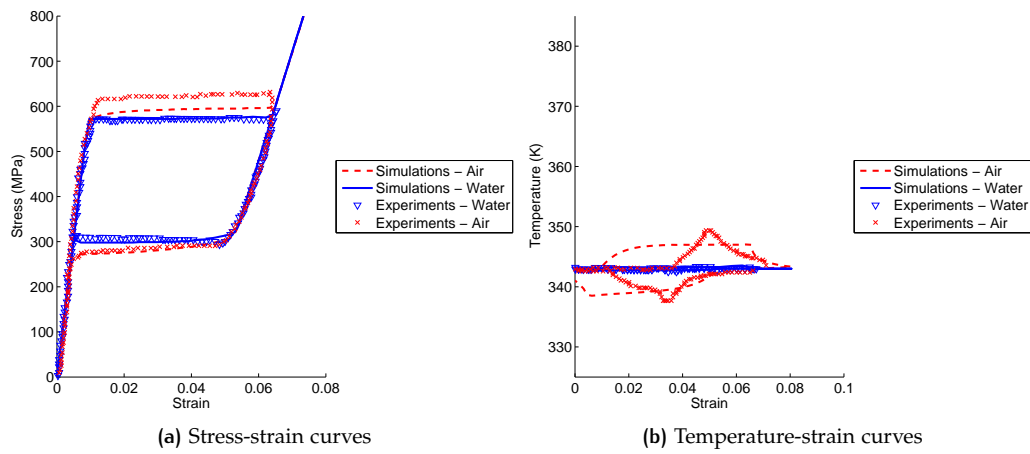


Figure 38. Experimental vs. numerical stress-strain and temperature-strain curves for a strain rate of  $4.10^{-4} \text{ s}^{-1}$ .

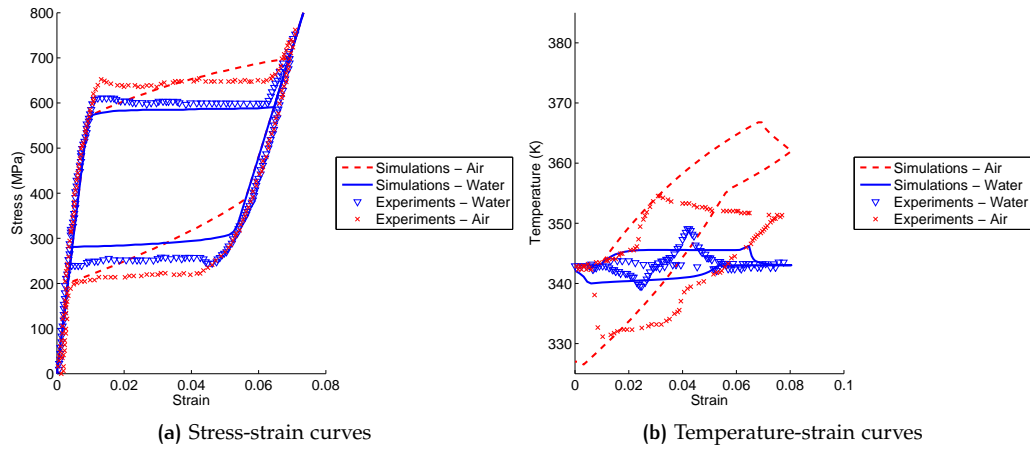


Figure 39. Experimental vs. numerical stress-strain and temperature-strain curves for a strain rate of  $4.10^{-3} \text{ s}^{-1}$ .

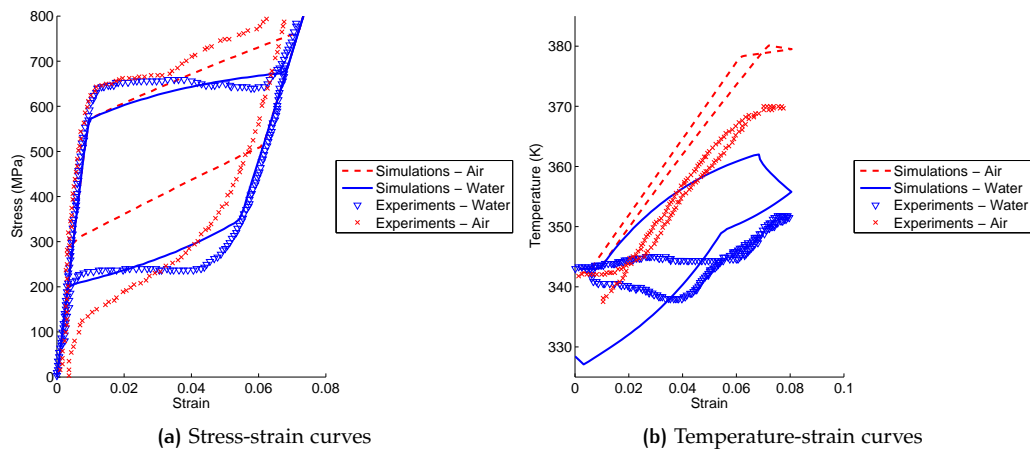
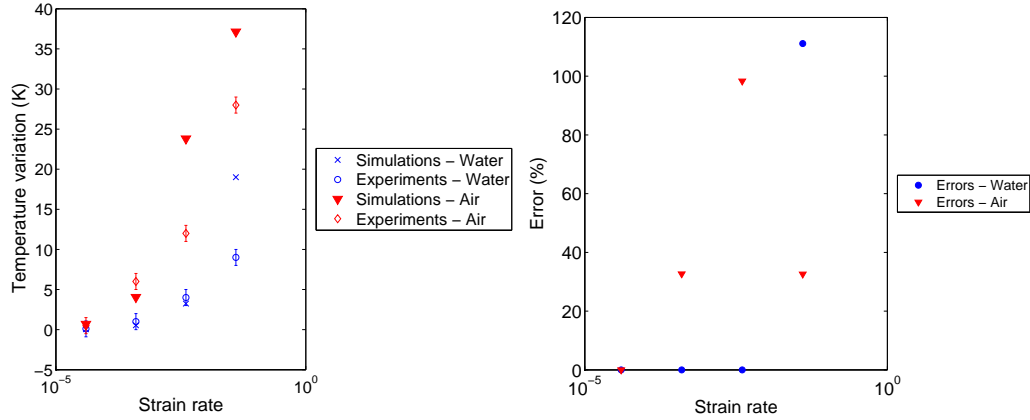


Figure 40. Experimental vs. numerical stress-strain and temperature-strain curves for a strain rate of  $4.10^{-2} \text{ s}^{-1}$ .

where  $\text{ampl}_{\text{simul}}$  and  $\text{ampl}_{\text{exp}}$  are the maximum amplitudes obtained respectively from simulation and from experimental data. The simulation error is considered to be zero if it is less than the uncertainty on experimental measurements. The errors are reported on Fig. 41b.



**Figure 41.** (a) Experimental and simulated maximum amplitudes of temperature variation during a loading cycle. The bars indicate uncertainties on experimental measurements. (b) Deviation from experimental measurements of temperature variation amplitudes calculated using the coupled ZM model.

### Discussion

The following is a discussion of the above results:

- At a very low strain rate of  $4 \cdot 10^{-5} \text{ s}^{-1}$ , Figs. 37a and 37b show excellent agreement between experiments and simulations both in water and in air. The behavior in this case is nearly isothermal because of the predominance of convective heat transfer.
- At a higher strain rate of  $4 \cdot 10^{-4} \text{ s}^{-1}$  (cf. Fig. 38a and 38b), good agreement is achieved with the tests carried in water. An error of about 30 % is observed, however, for tests carried in air. The error can be partly explained by the localization of phase change, which does not necessarily occur uniformly over the test sample. Indeed, it can be seen on Fig. 38b that the increase in temperature starts at 0.035 strain, suggesting that phase change at this point is occurring slightly after it has already begun elsewhere within the test sample. Moreover, the model does not correctly reproduce the increase of the direct phase transformation stress with the strain rate, even though the slopes of the phase change plateaus are correctly approximated.
- For the strain rate of  $4 \cdot 10^{-3} \text{ s}^{-1}$  (cf. Fig. 39a and 39b), the error is still negligible for the tests carried in water, but increases to about 100 % for tests carried in air. This large error can again be partly explained by the localization of phase change, which gives an abrupt increase of temperature toward the beginning of the transformation at the point where the temperature is measured, followed by a gradual decrease. The model, on the other hand, gives a more uniform temperature variation. Moreover, the reverse phase transformation stress is overestimated by the model, which is coherent with the calculated temperature being higher than the one measured at the onset of reverse phase change (cf. Fig. 39b).

- Similar observations can be made regarding the stress-strain and temperature-strain curves at  $4.10^{-2} \text{ s}^{-1}$ , where the error on the amplitude of temperature variation remains negligible in water but increases up to 100 % in air.

The reader's attention is brought to the fact that Shaw and Kyriakides [1995] performed displacement controlled experiments in which local strain rates are not constant [cf. Fig. 13 in Shaw and Kyriakides, 1995], since the deformation is not uniform in the structure. Furthermore, parameters such as the SMA specific heat capacity and the convective heat transfer coefficient of the test were not determined experimentally.

#### 4.4.2 Influence of the different heat sources

The relative importance of latent heat and intrinsic dissipation on the overall thermomechanical response of the material is now discussed. To this aim, the problem in section 4.3 is solved considering only one of these heat sources to be active at a time. The results are shown in Fig. 42. The following observations can be made:

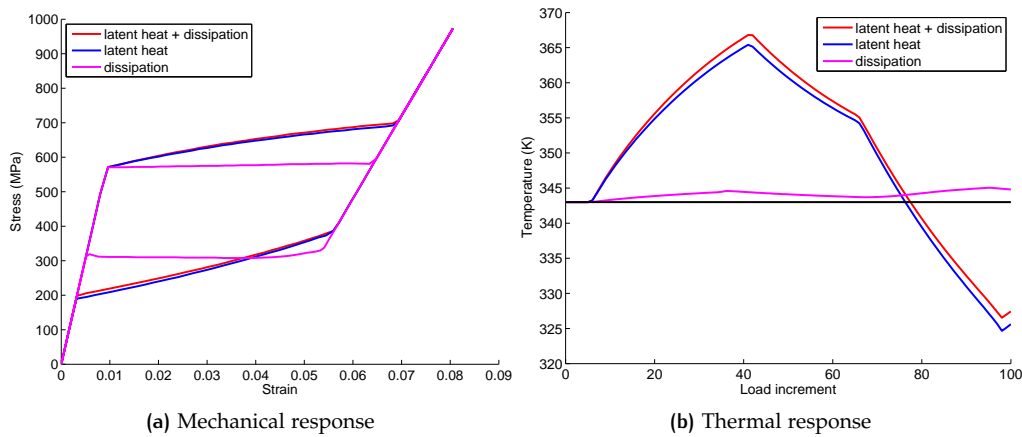


**Figure 42.** Evolution of the mechanical and thermal responses depending on whether only the latent heat or the intrinsic dissipation or both heat sources are considered in solving the heat equation.

- Latent heat seems to have predominant impact on temperature variation within the SMA (one order of magnitude higher than that of intrinsic dissipation).
- Latent heat can be either absorbed or released during phase change whereas intrinsic dissipation is always positive. The resulting temperature variation within the SMA can thus be either positive or negative.
- If only the intrinsic dissipation is considered, the mechanical response is nearly isothermal for the strain rates considered in this work.

#### 4.4.3 Influence of geometry and boundary conditions on hysteresis area

##### *Variation of the hysteresis area with the strain rate*

From the experiments of Shaw and Kyriakides (see Figs. 37a to 40a), it seems that the hysteresis area varies non monotonously with the strain rate. The same conclusion has already

been mentioned by Van Humbeeck [1991] and Auricchio and Sacco [2001]. The evolution of the hysteresis area with respect to the strain rate and obtained numerically is given in Fig. 43. At low strain rates, the hysteresis area is constant, then increases to reach a maximum and fi-

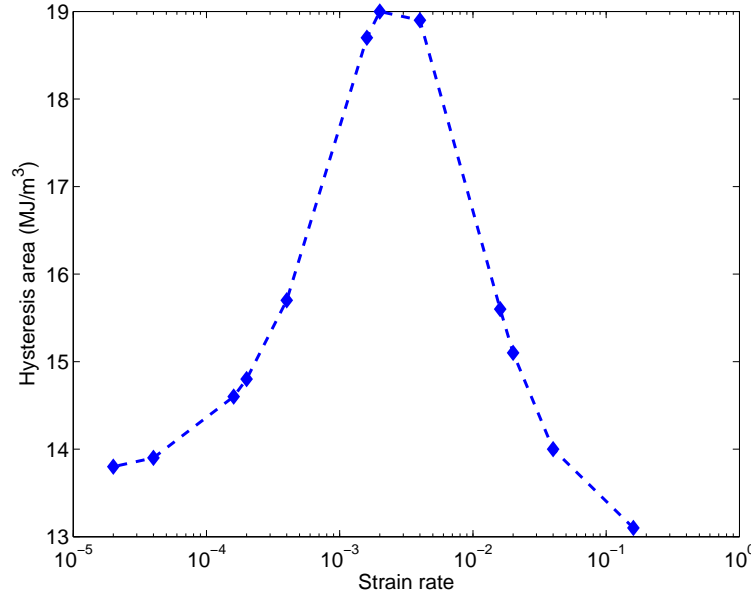


Figure 43. Evolution of the hysteresis area with the strain rate. In this simulation,  $h = 50 \text{ W.m}^{-2}.\text{K}^{-1}$ ,  $T_{\text{ext}} = 70 \text{ }^{\circ}\text{C}$ ,  $r = 1 \text{ mm}$ .

nally decreases. These observations may be explained by the relative evolution of the material temperature with respect to the external temperature:

- When the temperature of the SMA is higher than the external temperature  $T_{\text{ext}}$ , the yield stresses increase, leading to a greater slope of the stress-strain phase change plateau. The increase of the phase change stress onset is more pronounced at higher strain rates (cf. Fig. 44).
- During reverse phase change, the position of the stress-strain curve with respect to the quasi-static plateau depends on the evolution of the SMA temperature with respect to  $T_{\text{ext}}$ . Indeed, if phase change starts at a temperature higher than  $T_{\text{ext}}$ , the yield stress becomes higher than the isothermal yield stress at  $T_{\text{ext}}$ . In this case, the starting point of the reverse plateau is shifted upwards. When the temperature becomes lower than  $T_{\text{ext}}$ , the yield stress decreases and the reverse phase change plateau is shifted downwards (cf. Fig. 44).

It follows from the discussion above that for small strain rates, the area of the hysteresis loop is practically the same as in the quasistatic case because the temperature variation is small. For moderate strain rates, the material temperature oscillates around the external temperature, producing a stress-strain response partly above and partly below the quasistatic stress-strain curve. This can result in larger hysteresis. The above observations are qualitatively in agreement with the experimental data taken from Shaw and Kyriakides.

#### *Influence of geometry and boundary conditions*

The position of the maximum depends on the thermal boundary conditions and on the geometry of the specimen. For instance, if the convective heat transfer coefficient is increased, the

maximum of the curve moves towards higher strain rates (*cf.* Fig. 45a). If the radius of the specimen is increased, the maximum of the curve moves towards lower strain rates (*cf.* Fig. 45b). The evolution of the SMA's temperature is determined by a competition between two effects: heat conduction and convection. In the case of a larger radius, the former plays a major role, resulting in temperature increase at constant strain rate.

This ends up the extension of the ZM monocycle model. As our aim is the fatigue design, it is necessary to propose an extension of the cyclic model, so that to be able to determine a stabilized thermomechanical cycle with good accuracy. This is the aim of the next section.

## 4.5 EXTENSION TO THE CYCLIC BEHAVIOR

Unlike the different cyclic coupled models presented in the literature review, the ZM cyclic model aims at reproducing the structure degradation that takes place in the untrained structure. Thus, the stabilized response is influenced by two different phenomena occurring in the structure: thermomechanical coupling and microstructure degradation. After an experimental investigation, the ZM cyclic model is extended to account for thermomechanical coupling and is validated against experimental data.

### 4.5.1 Experimental investigation

The objective of this experimental investigation is to analyze thermomechanical coupling for superelastic SMA wires subjected to cyclic loading. This is achieved by studying the dependence of the mechanical response on strain rate and by interpreting it in terms of the variation of the specimen temperature. Section 4.5.1 presents the experimental facilities and procedures. The results are then presented and discussed.

#### *Experimental facilities and procedures*

**MATERIAL TESTED** The material used in the experiments was a polycrystalline Ni-Ti in the form of wires with a diameter of 2.0 mm and alloy composition of 56.1 wt% Ni obtained from AMF-France. The experiments were conducted on wires from the same batch in order to limit the influence of material composition on the mechanical response of the NiTi. The transformation temperatures were obtained using Differential Scanning Calorimetry (DSC). They were found to be as follows:  $M_s = 23\text{ }^{\circ}\text{C}$ ,  $M_f = 13\text{ }^{\circ}\text{C}$ ,  $A_s = 9\text{ }^{\circ}\text{C}$  and  $A_f = 24\text{ }^{\circ}\text{C}$ .

**EXPERIMENTAL SETUP** The experiments were carried using an MTS 810 universal testing machine with a maximum capacity of 100 kN. The strains were measured using an MTS extensometer (model 632.11C-20) with 50 mm gauge length and a precision of 0.01 %. Load and extensometer signals were captured using an MTS TestStar II data acquisition board connected to a personal computer. The external temperature was kept constant at  $50 \pm 1\text{ }^{\circ}\text{C}$ , using a Servathin hermetic enclosure, with temperature regulation. The material behaves heterogeneously and experiences local temperature variations. Local temperature measurements were obtained using three small thermocouples placed at different locations along the wire, in order to get an average temperature. The thermocouples were exposed junction type "K" made of 0.25 mm diameter wire. They were attached to the NiTi wires using 5 mm long heat shrink.

**EXPERIMENTAL PROCEDURE** The experiments were carried at a constant external temperature of  $50\text{ }^{\circ}\text{C}$ , which is higher than the transition temperature  $A_f^0$ . The NiTi wire was subject to 50

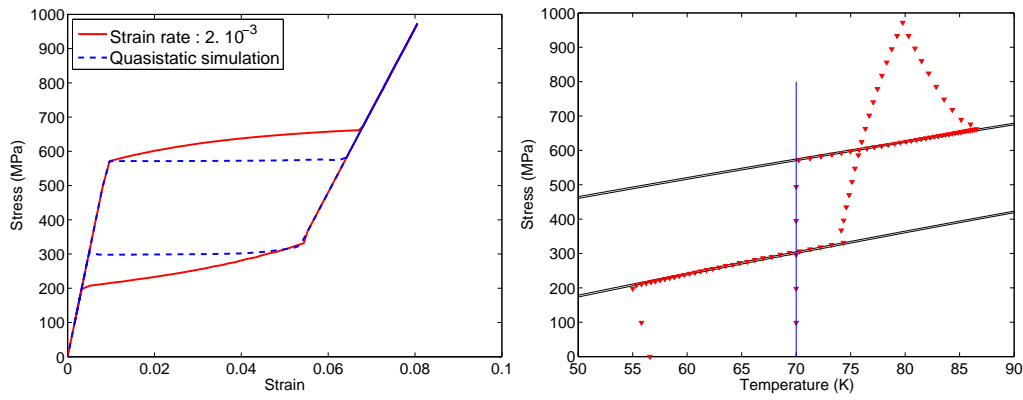


Figure 44. (a) Variation of the slopes of the phase change plateaus with respect to strain rate. (b) Evolution of the phase change yield stress with respect to the strain rate in the Clapeyron diagram. In both figures, the quasistatic curve is shown in blue, while the red curve corresponds to a strain rate of  $2 \cdot 10^{-3} \text{ s}^{-1}$ .

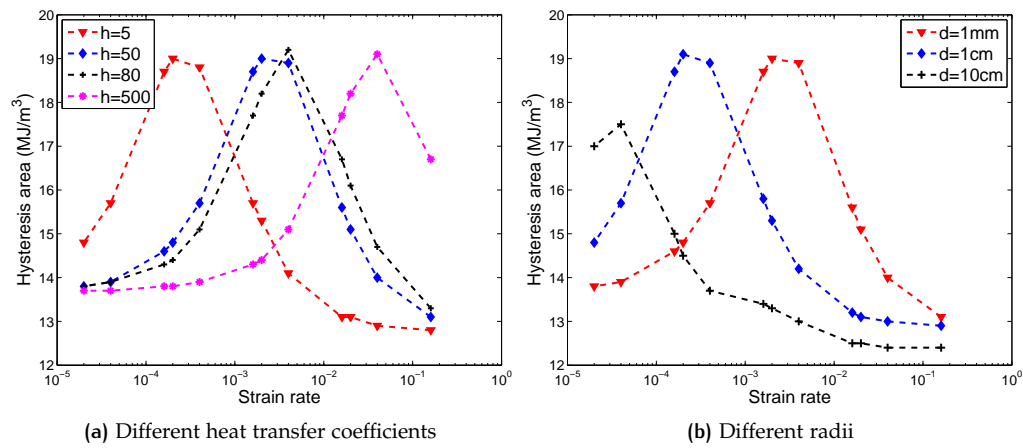


Figure 45. Evolution of the hysteresis area with the strain rate for (a) different convective heat transfer coefficients ( $r = 1 \text{ mm}$ ) and for (b) specimens with different radii ( $h = 50 \text{ W} \cdot \text{m}^{-2} \cdot \text{K}^{-1}$ ). In both simulations,  $T_{\text{ext}} = 70 \text{ }^{\circ}\text{C}$ .

cycles of quasistatic tensile loading at constant strain rates between  $1 \cdot 10^{-4}$  and  $5 \cdot 10^{-3} \text{ s}^{-1}$ . The maximum load (about 800 MPa) is chosen higher than the martensitic finish stress.

### Results

The reproducibility of the experimental results is first investigated. Then, the mechanical results are presented, followed by the thermal ones.

**REPRODUCIBILITY OF THE EXPERIMENTS** Each test at a prescribed strain rate was carried twice.

*Mechanical reproducibility:* Good reproducibility is obtained for all cycles (see Figs. 46-48): yield stresses, hysteresis areas and maximum strains are the same for both tests. There is some

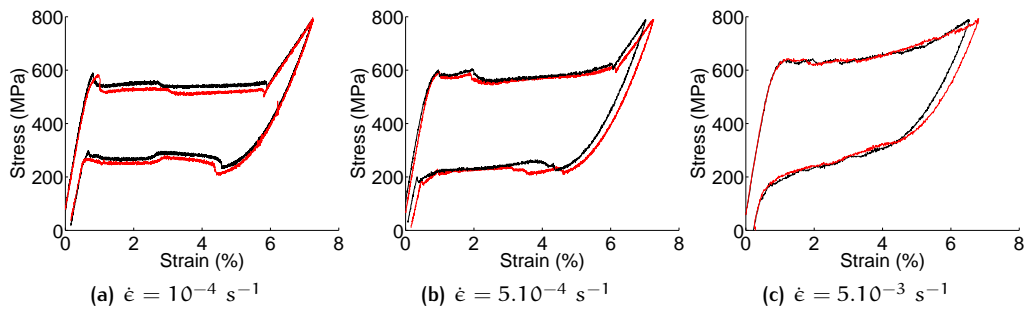


Figure 46. Reproducibility of the first stress-strain cycle at different strain rates.

difference, however, in the amount of the observed residual strain after the transient phase (see Fig. 47 for the 20th cycle and Fig. 48 for the 40th cycle). The overall reproducibility remains satisfactory in terms of phase transformation stresses and plateaus, and size of hysteresis.

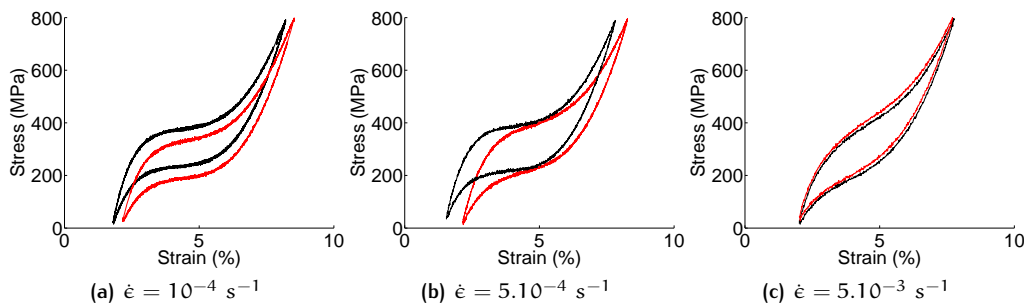


Figure 47. Reproducibility of the 20th stress-strain cycle at different strain rates.

*Thermal reproducibility* Figs. 49-51 show that the evolution of temperature during cycling is reproducible for different strain rates.

Overall, the thermomechanical response of the NiTi wires is reproducible for the loading conditions considered in this paper. The results can thus be used for analyzing the strongly coupled superelastic behavior of the material.

**EVOLUTION OF THE MECHANICAL RESPONSE WITH THE STRAIN RATE** In this section, the influence of strain rate on hysteresis is investigated for both transient and stabilized states.

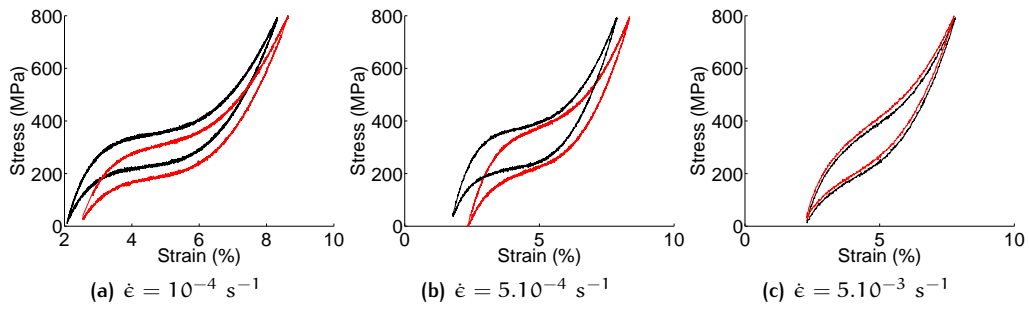


Figure 48. Reproducibility of the 40th stress-strain cycle at different strain rates.

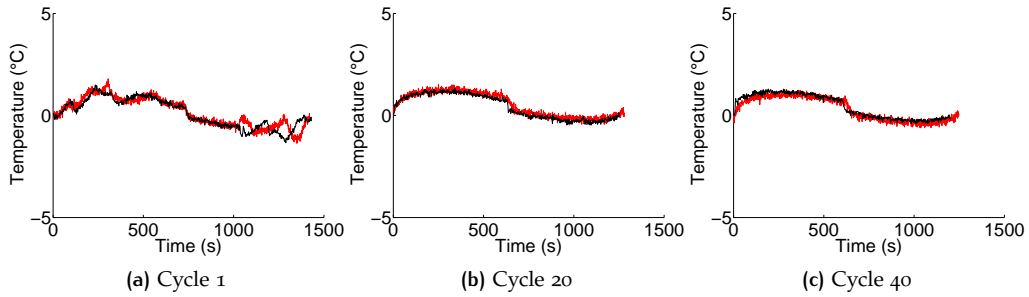


Figure 49. Evolution of the average temperature for cycles 1, 20 and 40 at  $\dot{\epsilon} = 1.10^{-4} \text{ s}^{-1}$ .

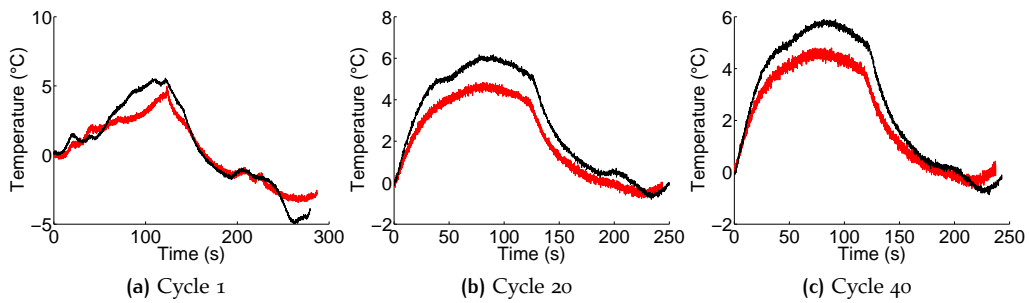


Figure 50. Evolution of the average temperature for cycles 1, 20 and 40 at  $\dot{\epsilon} = 5 \cdot 10^{-4} \text{ s}^{-1}$ .

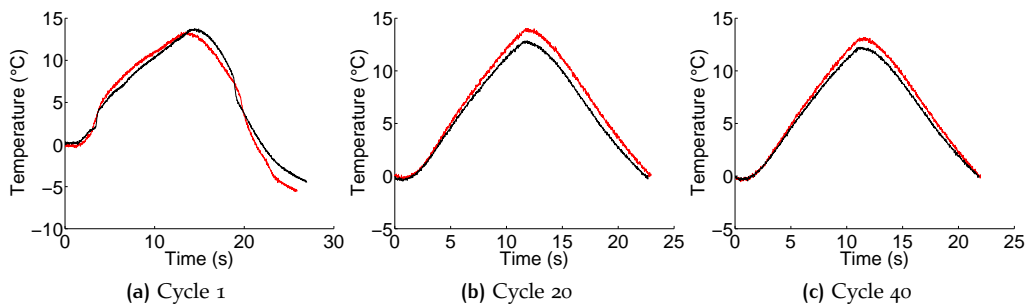


Figure 51. Evolution of the average temperature for cycles 1, 20 and 40 at  $\dot{\epsilon} = 5 \cdot 10^{-3} \text{ s}^{-1}$ .

In Fig. 52, stress-strain curves of the first cycles are given for all the strain rates considered for the tests. The martensite start yield stress is independent of the strain rate for the first cycle. However, a variation in the slopes of the phase change plateaus can be noticed. This variation is

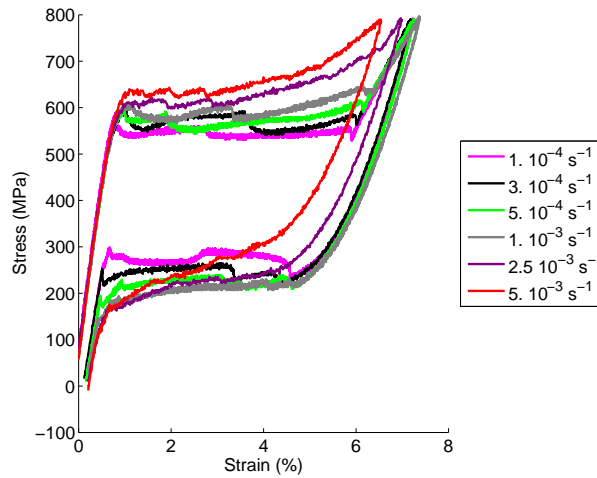


Figure 52. Stress-strain curves of the first cycles for all tested strain rates.

especially visible for the direct phase change plateau reported on Fig. 53a: the slope increases with increasing strain rate. The evolution of hysteresis is non monotonic with a maximum at

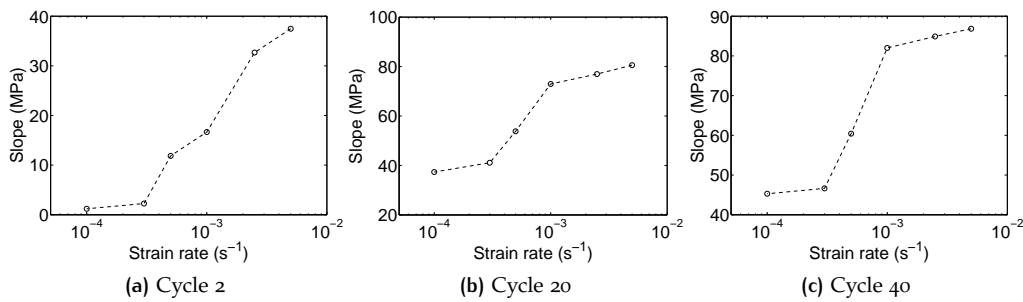


Figure 53. Evolution of the slopes of the direct phase change plateau with respect to the strain rate.

$10^{-3} \text{ s}^{-1}$  strain rate as shown in Fig. 54a.

Let us now recall the main characteristics of the stress strain response of an SMA subject to a pseudoelastic cyclic loading (*cf.* Fig. 55a, [Zaki and Moumni, 2007b], section 2.2.2):

- decrease of the martensite phase change yield stress,
- increase of the residual strain,
- decrease of the hysteresis area (*cf.* Fig. 55b).

All these properties stabilize after a few cycles (here, about 20 cycles). The evolution of these three main properties varies with the strain rate at the stabilized cycle. The slope of the direct phase change plateau still increases with the strain rate while cycling, and is bigger at the stabilized cycle than at the first one (*cf.* Fig. 53b-c). Concerning the evolution of the hysteresis

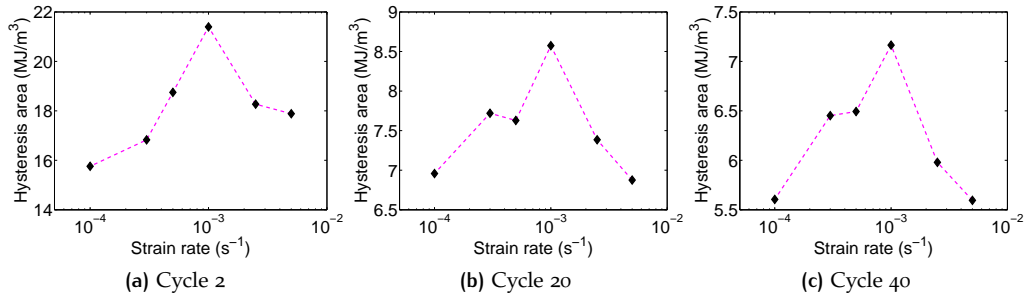


Figure 54. Evolution of the hysteresis area.

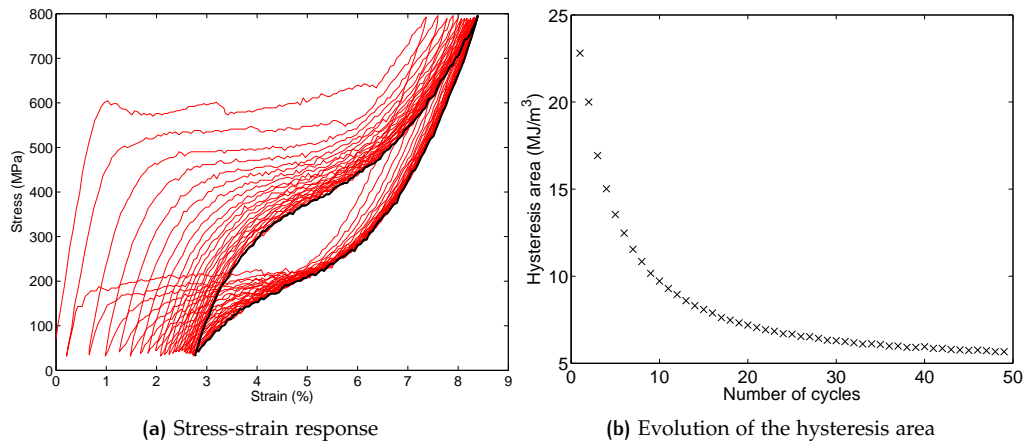


Figure 55. (a) Cyclic stress-strain response of an SMA wire subject to pseudoelastic cyclic loading. (b) Evolution of the hysteresis area with respect to the number of cycles. For both figures,  $\dot{\epsilon} = 10^{-3} \text{ s}^{-1}$ .

area, a non monotonic evolution is still observed during cycling, with a maximum at the same strain rate ( $1.10^{-3} \text{ s}^{-1}$ ) (cf. Fig. 54b-(c)). The martensite start yield stress tends to decrease with the strain rate at the stabilized cycle (cf. Fig. 56a). This is in agreement with the temperature evolutions on Fig. 56b.

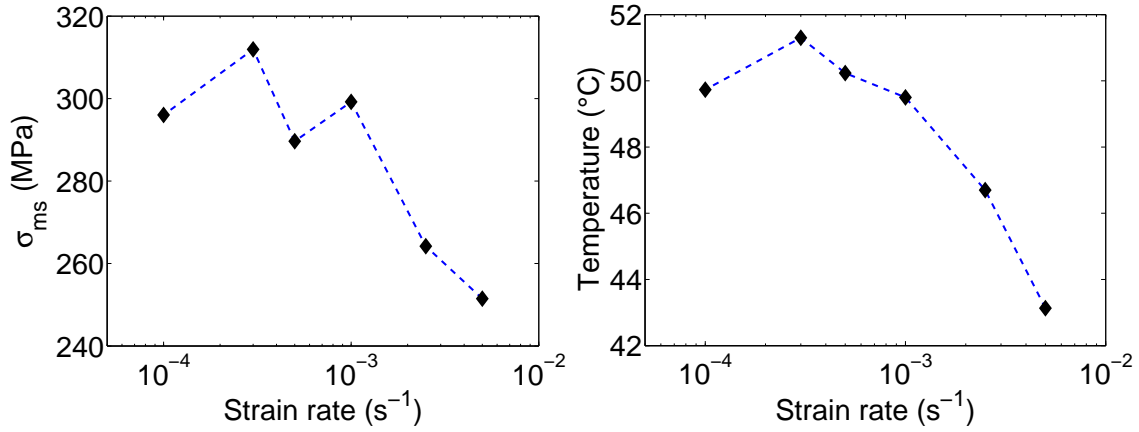


Figure 56. (a) Evolution of the martensite start yield stress with respect to the strain rate. (b) Evolution of the temperature at the phase change yield stress.

**EVOLUTION OF THE THERMAL RESPONSE** The temperature evolution during the first twenty cycles is given in Fig. 57 for different strain rates. For a given cycle, the temperature increases

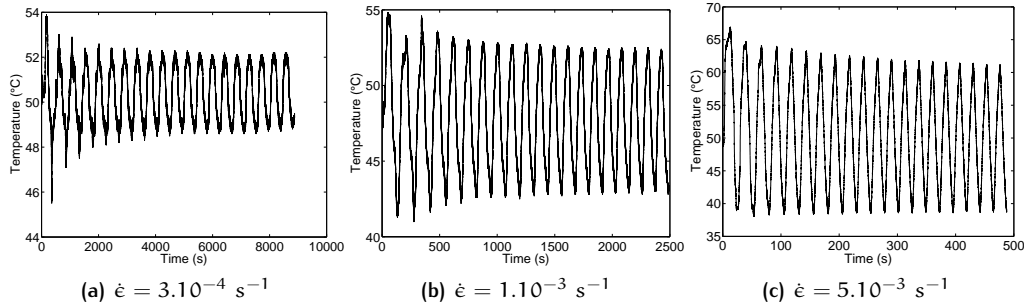


Figure 57. Stabilization of the temperature evolution during cycling for three different strain rates.

during forward phase change (exothermic transformation) and decreases during reverse phase change (endothermic transformation) (cf. e.g. Fig. 50). This is independent of the cycle and of the strain rate. However, the average temperature of the cycle as well as the temperature amplitude strongly depend on the strain rate. Maximum and minimum temperature values for the first and the 20th cycles with respect to the strain rate are reported on Fig. 58a and (c), and the amplitudes on Fig. 58b and (d).

### Discussion

At the first cycle, the martensite start yield stress does not depend on the strain rate. Indeed, during elastic loading, the variation in temperature is negligible because it can only come from

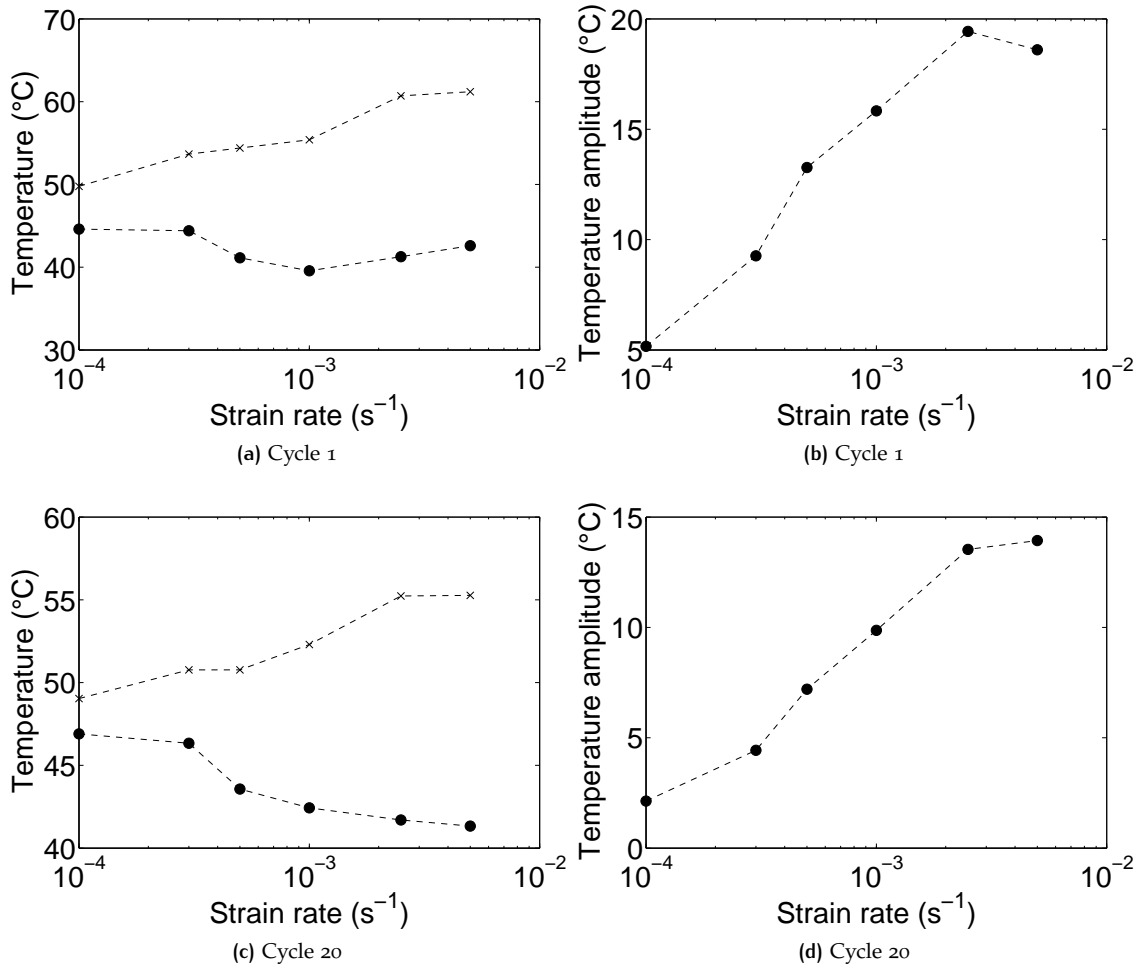


Figure 58. (a) and (c): Evolution of the minimum (circles) and maximum (crosses) temperatures with respect to the strain rate. (b) and (d): Evolution of the temperature amplitudes with respect to the strain rate.

thermoelastic effects. Therefore, the yield stress does not vary with the strain rate. However, a small decrease of the stress can be noticed after the yield stress, which can be explained by the localization of phase change (*cf.* Li and Sun [2002]). Moreover, the evolution of the slopes of the phase change plateaus as well as the evolution of the hysteresis area with respect to strain rate may be explained by the relative evolution of the material temperature with respect to the external temperature:

- When the temperature of the SMA is higher than the external temperature  $T_{ext}$ , the yield stresses increase, leading to a greater slope of the stress-strain phase change plateau. The increase of the phase change stress onset is more pronounced at higher strain rates (*cf.* Fig. 52).
- During reverse phase change, the position of the stress-strain curve with respect to the quasi-static plateau depends on the evolution of the SMA temperature with respect to  $T_{ext}$ . Indeed, if phase change starts at a temperature higher than  $T_{ext}$ , the yield stress becomes higher than the isothermal yield stress at  $T_{ext}$ . In this case, the starting point of the reverse plateau is shifted upwards. When the temperature becomes lower than  $T_{ext}$ , the yield stress decreases and the reverse phase change plateau is shifted downwards (*cf.* Fig. 52).

It follows from the discussion above that for small strain rates, the area of the hysteresis loop is practically the same as in the quasistatic case because the temperature variation is small (*cf.* Fig. 57a). For moderate strain rates, the material temperature oscillates around the external temperature, producing a stress-strain response partly above and partly below the quasistatic stress-strain curve (*cf.* Fig. 57b). This can result in larger hysteresis. The position of the maximum depends on the thermal boundary conditions and on the geometry of the specimen.

During cycling, the temperature evolution tends to stabilize (*cf.* Fig. 57). The stabilization depends on strain rate and influences the evolution of the yield stresses. Indeed, the higher the strain rate, the smaller the temperature at the beginning of a cycle (*cf.* Fig. 56b), and thus the smaller the direct phase change yield stress (*cf.* Fig. 56a). This also explains the higher increase of the plateaus (*cf.* Fig. 53): during the beginning of the direct phase change, both convection and latent heat contribute to increasing the temperature of the material, resulting in higher yield stress. It is worth noticing that the maximum of hysteresis area is always reached for the same strain rate: this could be explained by the thermomechanical coupling (*cf.* Fig. 54). For a given strain rate, the characteristic time related to heat production as well as the characteristic time related to propagation of heat by convection only depend on the geometry of the specimen and on the thermal boundary conditions, and are thus constant when the number of cycles increases. Those two characteristic times govern the evolution of temperature in the specimen during both direct and reverse phase change. Depending on these times, temperature remains above or becomes lower than the initial temperature. Thus, they govern the relative position of the phase change plateaus with respect to the isothermal ones, and consequently the size of the hysteresis loop.

#### 4.5.2 Modelling

The modelling of the coupled cyclic model follows the same ideas as for the monocycle model: a heat capacity is introduced into the free energy and the heat equation is derived.

### Heat equation and heat sources

Taking into account the thermomechanical coupling requires the derivation of the heat equation. The entropy  $s$  is obtained from the expression of the Lagrangian (2.22), to which a heat capacity is added, by:

$$s = -\frac{\partial \mathcal{L}}{\partial T} = \rho C_p \ln \left( \frac{T}{T_0} \right) - \xi z. \quad (4.33)$$

The combination of first and second laws of thermodynamics leads to the expression of the heat equation:

$$\rho C_p \dot{T} - \text{div}(\mathbf{k} \nabla T) = r + \mathcal{D}_1 - T \frac{\partial s}{\partial z} \dot{z}, \quad (4.34)$$

where the Fourier's law for heat conduction with a constant thermal conductivity  $k$  has been assumed :  $\mathbf{q} = -k \nabla T$ . The density of internal heat generation  $r$  is equal to zero. Besides, the intrinsic dissipation is:

$$\mathcal{D}_1 = \mathcal{A}_z \dot{z} + \mathcal{A}_{\text{ori}} : \dot{\epsilon}_{\text{ori}} + \mathcal{A}_B : \dot{\mathbf{B}} + \mathcal{A}_r : \dot{\epsilon}_r + \mathcal{A}_e \dot{z}_e, \quad (4.35)$$

For physical reasons, the term  $\mathcal{A}_e \dot{z}_e$ , related to the evolution of the cumulative fraction of martensite, is neglected, since the dissipative phenomenon is the formation of martensite, governed by the term  $\mathcal{A}_z \dot{z}$ . The term related to the orientation of martensite  $\mathcal{A}_{\text{ori}} : \dot{\epsilon}_{\text{ori}}$  is also neglected, because the orientation of  $\epsilon_{\text{ori}}$  is taken to be constant. Thus, the heat equation becomes:

$$\rho C_p \dot{T} - k \Delta T = \mathcal{A}_z \dot{z} + \mathcal{A}_B : \dot{\mathbf{B}} + \mathcal{A}_r : \dot{\epsilon}_r + T \xi \dot{z} \quad (4.36)$$

### Coupled problem

The coupled problem is composed of the same set of equations as previously:

- equilibrium equations (Eq. (4.12)-(4.14)) and strain compatibility (Eq. (4.15)),
- constitutive equations (Eq. (2.24) and complementary laws),
- heat equation (Eq. (4.36)) and boundary conditions (Eqs. (4.18)-(4.19)).

The coupled algorithm can be easily adapted from Table 8 as:

- the discretization of the mechanical problem has already been detailed in section 2.4.2 (return mapping algorithm in Table 4);
- The discretization of the heat equation is similar to the one of section 4.3.2.

### 4.5.3 Validation of the coupled model

The experiments carried in section 4.5.1 are simulated using the cyclic model. The structure, an SMA wire, is subject to a mechanical pseudoelastic loading, with a constant external temperature. Thus, temperature variations only come from dissipation, latent heat or convection.

### Numerical considerations

We consider a superelastic SMA wire, with a diameter of 2 mm and a length of 100 mm. It is clamped on one end and subjected to prescribed tensile displacement on the other end (*cf.* Fig. 59). Maximum and minimum stresses to be reached are fixed. Six different loading rates are considered:  $1.10^{-4}$ ,  $3.10^{-4}$ ,  $5.10^{-4}$ ,  $1.10^{-3}$ ,  $2.510^{-3}$  and  $5.10^{-3} \text{ s}^{-1}$  respectively. The parameters of the model are determined with the procedure described in Zaki and Moumni [2007b] using the lowest strain rate experiment. They are listed in Table 10. The response of the SMA is plotted for a point situated on the external surface of the wire. 20 cycles have been computed for all strain rates.

Parameters values			
$E_A$	69708 MPa	$E_M$	33029 MPa
$\nu$	0.3	$\tau$	21
$a^{(0)}$	7.2205 MPa	$a^{(sat)}$	2.2464 MPa
$b^{(0)}$	7.5122 MPa	$b^{(sat)}$	2.7739 MPa
$G^{(0)}$	6.3795 MPa	$G^{(sat)}$	8.8736 MPa
$\alpha^{(0)}$	1956.5 MPa	$\alpha^{(sat)}$	2689.5 MPa
$\beta^{(0)}$	4103.1 MPa	$\beta^{(sat)}$	5640.4 MPa
$\xi^{(0)}$	0.4 MPa/°C	$\xi^{(sat)}$	0.15 MPa/°C
$\kappa^{(0)}$	16.6805 MPa	$\kappa^{(sat)}$	13.0546 MPa
$\gamma^{(0)}$	5.0 %	$\gamma^{(sat)}$	3.71 %
$\epsilon_r^{(sat)}$	2.17 %	$B^{(sat)}$	209 MPa
$Y$	107.3 MPa	$T^0$	50 °C
$C_p$	440 J.kg <sup>-1</sup> .K <sup>-1</sup>	$h_{air}$	110 W.m <sup>-2</sup> .K <sup>-1</sup>
$\rho$	6500 kg.m <sup>-3</sup>	$k$	18 W.m <sup>-1</sup> .K <sup>-1</sup>

Table 10. Model parameters

### Experimental comparison for the first loading cycle

In Fig. 60, the simulated stress-strain response for the SMA wires is shown to closely fit the experimental tensile curves for different strain rates. However, in experiments, instabilities appear during the starting of phase transformation due to the propagation of the phase transformation front [*cf.* Li and Sun, 2002]. This phenomenon is not reproduced by the simulations since our model does not account for localization phenomena. Fig. 61 presents the comparison of the hysteresis areas. As expected, the evolution of the hysteresis area with respect to the strain rate has a non monotonic evolution (*cf.* Fig. 61a). Good agreement is achieved since the maximum error is 8.6 % (*cf.* Fig. 61b). Finally, Fig. 62 is a comparison between experimental and simulated maximum and minimum temperatures. Good agreement is achieved at low and moderate strain rates. At high strain rates, the reduced accuracy could be explained by the accentuation of the localization phenomenon with the strain rate.

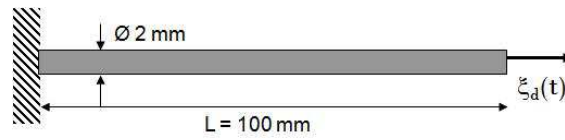


Figure 59. Geometry of the specimen used for the numerical simulations

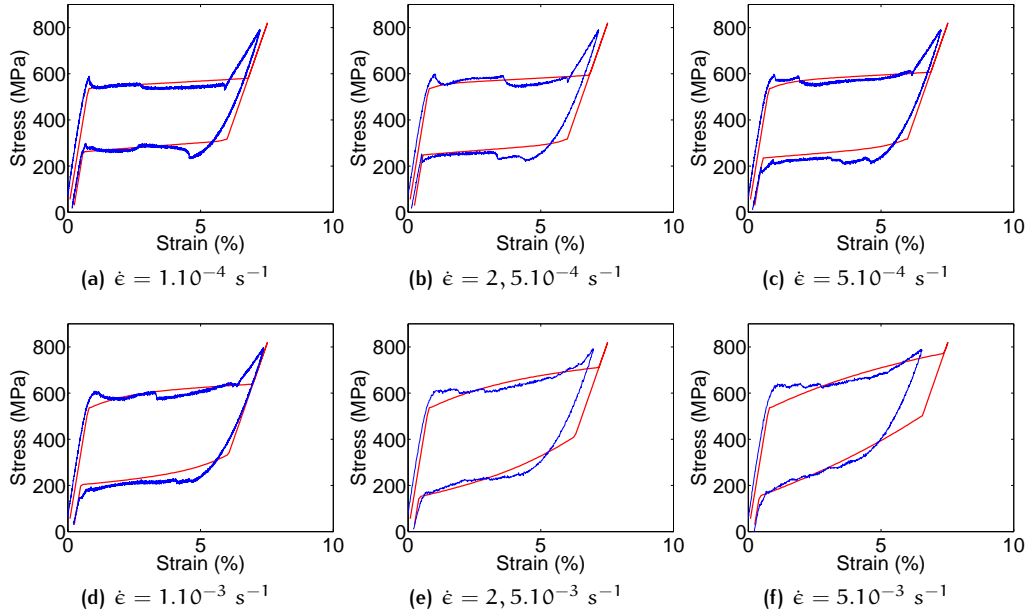


Figure 60. Comparison of the first cycle obtained by the experiments (blue) and the simulation (red) for the different strain rates.

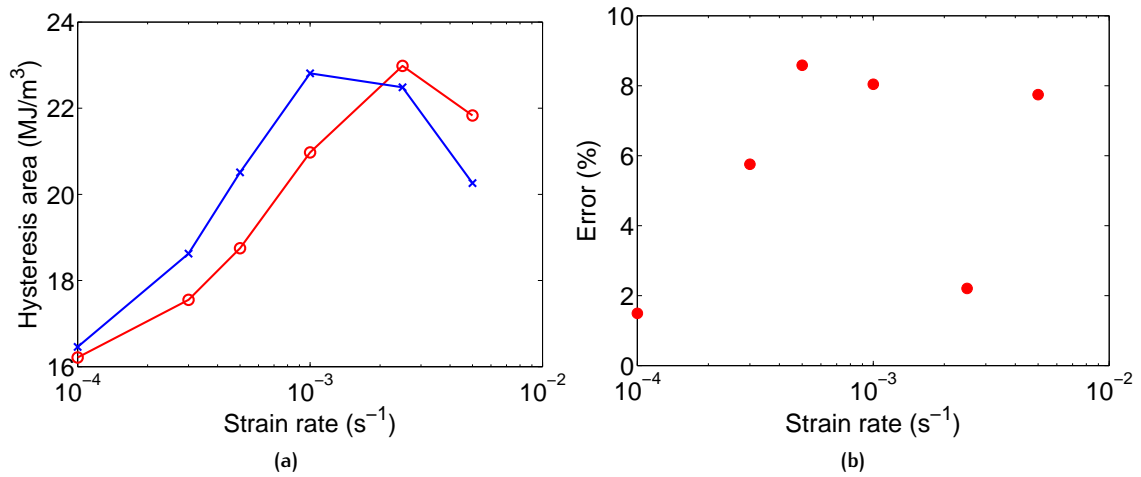


Figure 61. (a) Comparison of the evolution of the hysteresis areas obtained by the experiments (blue) and by the simulations (red). (b) Error on the numerical estimation of the area by comparison with the experimental area.

### *Cyclic evolution*

In this section, a comparison of one intermediate cycle is presented. Fig. 63 is a comparison of the mechanical response at the 10th cycle. Good qualitative agreement is achieved, although the model predicts higher hysteresis area than experimentally observed (*cf.* Fig. 64a). However, temperature predictions are satisfactory (*cf.* Fig. 64b), especially at low and moderate strain rates. The error can be explained by the evolution of some parameters of the model, which might not be represented by the same exponential function as the others. It is interesting to note that the model correctly predicts the strain rate at which maximum hysteresis area is achieved.

### *Stabilized cycle*

According to the results presented in Section 4.5.1, the 20th cycle is considered as the stabilized cycle. Fig. 65 reports the comparison between the experimental and the simulated values at all strain rates. Good agreement is achieved for low and moderate strain rates. However, at high strain rates, a small error is observed when comparing the slopes of the phase transformation plateaus. Nevertheless, the error made on the calculation of the hysteresis area is less than 10 % (*cf.* Fig. 66b), which is acceptable since we are mainly interested by the size of the hysteresis area at the stabilized cycle to evaluate the fatigue lifetime of the SMA. Moreover, the simulations reproduce well the maximum value of the hysteresis area at the same strain rate given by the experiments (namely  $10^{-3} \text{ s}^{-1}$ ) (*cf.* Fig. 66a). Finally, Fig. 67a shows that the evolution of temperature is well captured for all strain rates. In fact, the maximum error is less than 9 % as given in Fig. 67b.

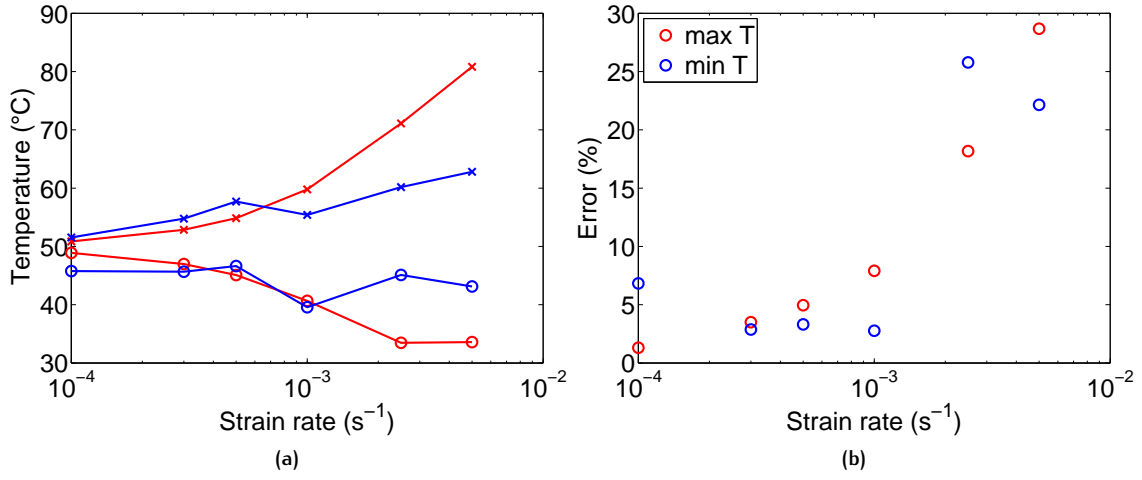


Figure 62. (a) Comparison of the minimum (circles) and maximum (crosses) temperatures over the first cycle obtained by the experiments (blue) and by the simulations (red). (b) Error on the numerical estimation of these temperatures by comparison with the experimental values.

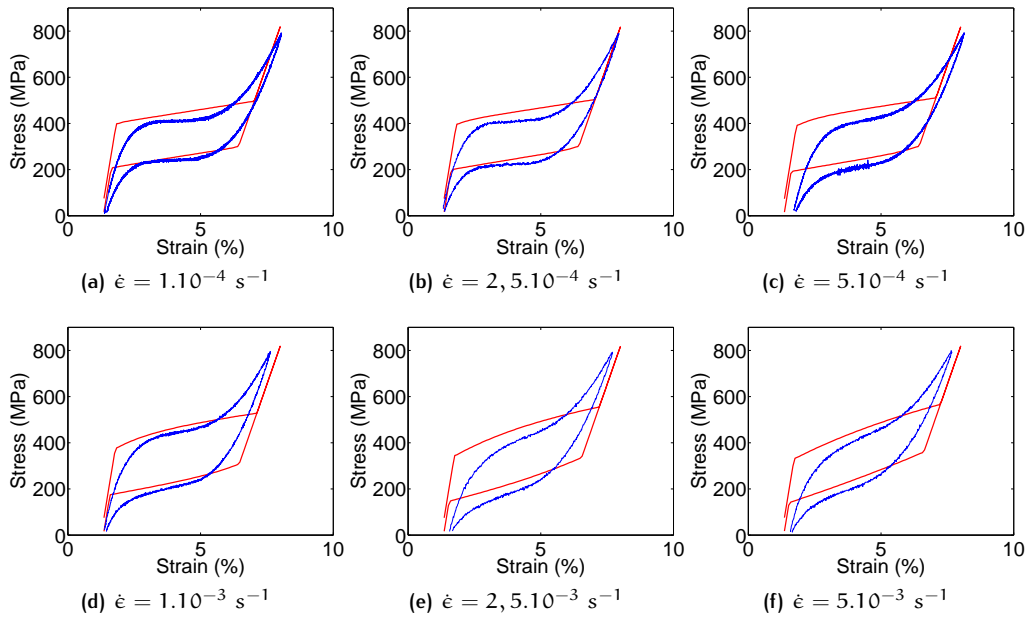


Figure 63. Comparison of the 10th cycle obtained by the experiments (blue) and the simulation (red) for the different strain rates.

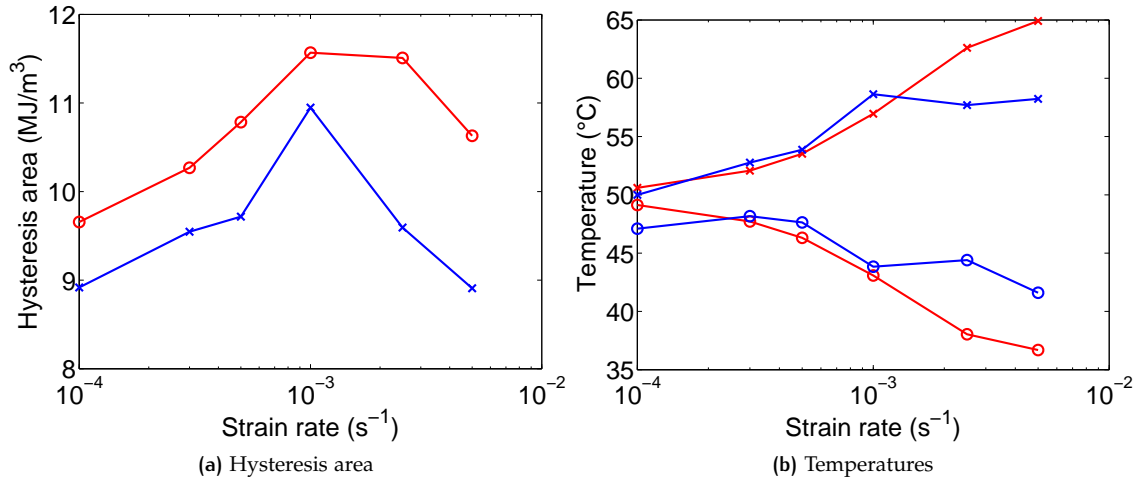


Figure 64. (a): Comparison of the hysteresis areas obtained from the experiments (blue) and from the simulations (red) for the 10th cycle (transient response). (b): Comparison of the maximum (crosses) and minimum (circles) temperature values over the 10th cycle obtained by the experiments (blue) or by the simulations (red).

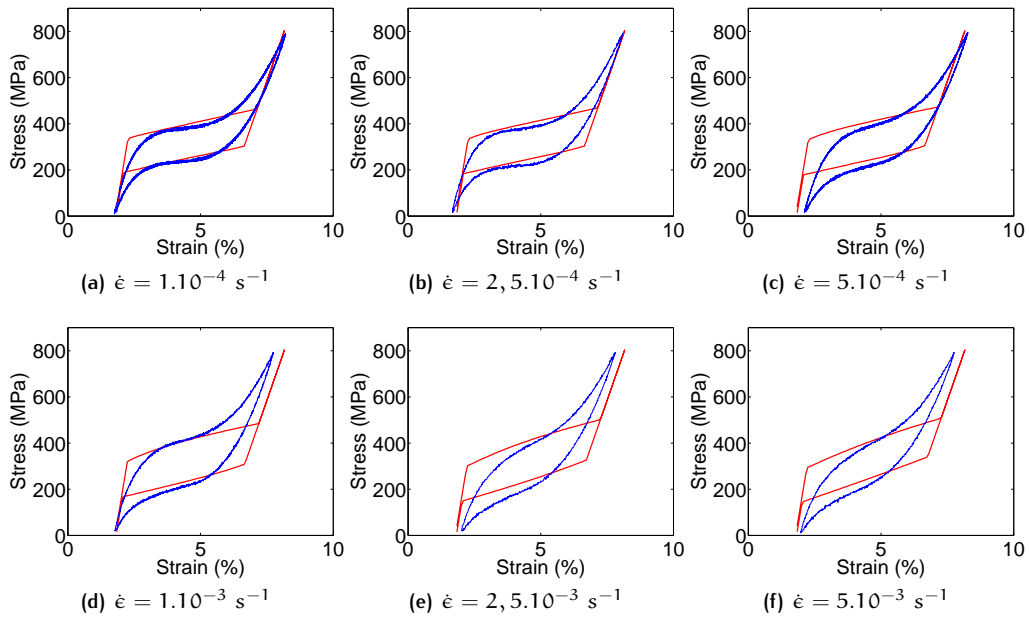


Figure 65. Comparison of the stabilized cycle obtained by the experiments (blue) and the simulation (red) for the different strain rates.

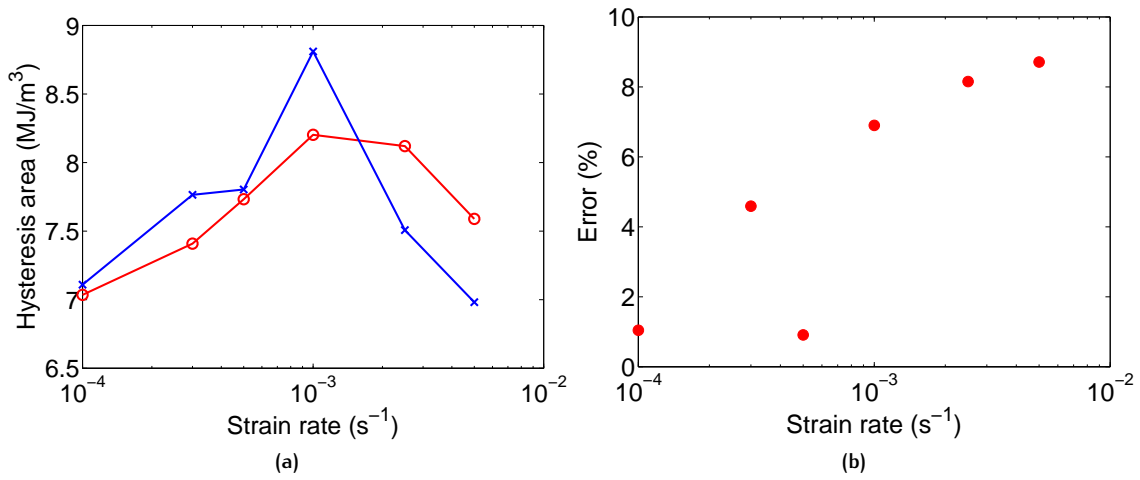


Figure 66. (a) Comparison of the evolution of the hysteresis areas obtained by the experiments (blue) and by the simulations (red) for the stabilized cycle. (b) Error on the numerical estimation of the area by comparison with the experimental one.

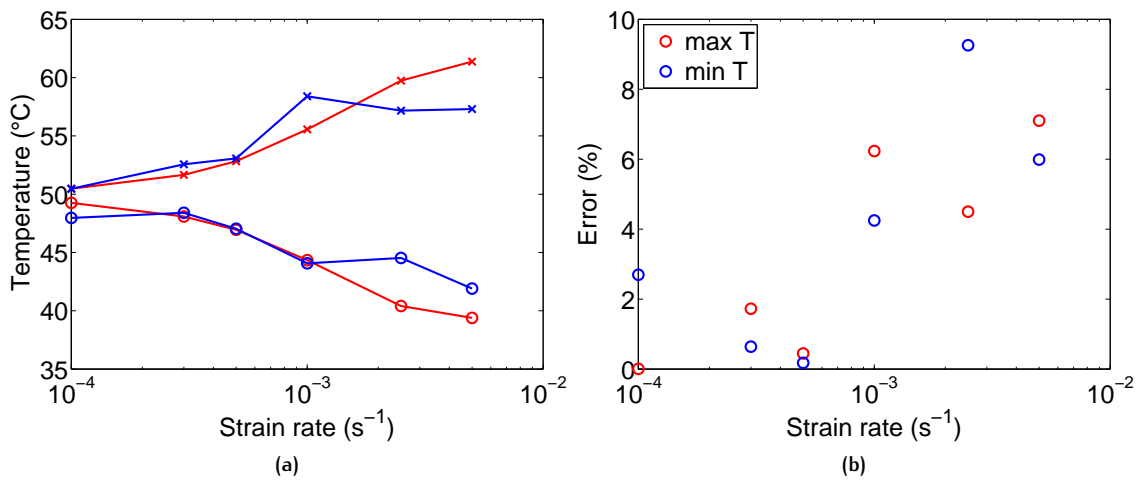


Figure 67. (a) Comparison of the minimum (circles) and maximum (crosses) temperatures over the stabilized cycle obtained by the experiments (blue) and by the simulations (red). (b) Error on the numerical estimation of these temperatures by comparison with the experimental values.

## 4.6 CONCLUSION

The monocycle ZM model for SMA is extended to account for thermomechanical coupling. It is implemented into the finite element code Cast3m, considering strong coupling between mechanical and thermal equations. Quantitative and qualitative comparisons between experiments and simulations at low strain rates show good agreement for both thermal and mechanical responses. However, for high strain rates the agreement is achieved only qualitatively. This discrepancy may be explained by the occurrence of the localization of the martensitic transformation which is not considered in our model. The model accounts for intrinsic dissipation, which explains the formation of the hysteresis loop even for quasistatic loading conditions, and latent heat, which was found to be predominant when solving the heat equation. The limited influence of dissipation on the temperature of the material should not be interpreted as a complete absence of intrinsic dissipation. Then, an experimental and theoretical study of the thermomechanical coupling in SMAs in the cyclic pseudoelastic regime has been provided. First, an experimental analysis has been performed using superelastic NiTi wires subjected to cyclic loadings. The obtained results give an explanation of the evolution of the mechanical response with the strain rate. Namely, the analysis of the thermal results allow to associate this dependence to the thermomechanical coupling. For example, the stabilized cycle is greatly influenced by the thermomechanical coupling, because phase transformation yield stresses and slopes as well as hysteresis area change with strain rate. In addition, it is shown that the hysteresis area follows a non-monotonic evolution with the strain rate for both the transient and the stabilized responses and that the maximum is reached for a strain rate of  $1.10^{-3} \text{ s}^{-1}$ . Second, in order to account for the cyclic thermomechanical coupling, a model was developed and validated against experimental data. A good correlation is achieved for both the transient and the stabilized mechanical responses for all strain rates. The thermal response is also reproduced, but with lower accuracy especially at high strain rates. The simulation reproduces the non monotonic evolution of the hysteresis area at the stabilized cycle, with a maximum error of 8 %.

The next step is to correlate these observations with the fatigue lifetime of SMA structure. Indeed, following [Moumni et al. \[2005\]](#), the number of cycles to failure  $N_f$  is related to the hysteresis area  $W$  at the stabilized cycle through a power law:

$$W = mN_f^p,$$

where  $m$  and  $p$  are material constants. Since the evolution of the hysteresis area is non monotonic with respect to the strain rate, a non monotonic evolution of the fatigue lifetime can be expected, with a minimum corresponding to maximum hysteresis, since the fatigue of SMA structures depends on the loading frequency. This will be discussed in Chapter 6, dealing with fatigue.

Before dealing with the fatigue criterion, we propose to develop a numerical method to reduce the computation time that can be prohibitive as soon as an important number of cycles has to be computed on a structure with a large number of degrees of freedom.

# 5 | NUMERICAL COMPUTATION OF THE STABILIZED CYCLE

---

5.1	Literature review on the numerical methods	93
5.1.1	Shakedown	94
5.1.2	Direct methods	94
5.2	The Direct Cyclic Method for SMA behavior	95
5.2.1	Main ideas	95
5.2.2	Numerical algorithm	96
5.2.3	Results	99
5.3	Conclusion	103

---

The determination of the number of cycles to failure of complex superelastic structures requires

- a reliable constitutive law,
- the computation of the asymptotic state of the structure,
- a proper fatigue criterion.

The previous chapters developed extensions of the ZM models to allow precise prediction of the asymptotic state. Indeed, the fatigue criterion uses the asymptotic state of the structure as an input parameter, assuming that the structure spends the larger part of its life in this asymptotic state<sup>1</sup>. It becomes then theoretically possible to determine the number of cycles to failure of complex superelastic structures [see [Moumni et al., 2009](#)].

The time required to compute the stabilized response of a structure subject to cyclic mechanical loading can be prohibitive, due to the tens of cycles that have to be computed to reach the asymptotic state. The reduction of this computation time is of prime importance for industrial applications. To this aim, different approaches have been proposed in literature, mainly for elasto-plastic constitutive laws and are presented below.

This chapter aims at extending one of these numerical methods allowing a reduction in computation time for the determination of the stabilized state of an SMA structure subject to cyclic loadings. Among the different existing methods, we choose the Direct Cyclic Method. After a brief literature review on the shakedown theory and on direct methods, the Direct Cyclic Method is extended to SMA behavior and its efficiency is tested on three loading paths.

## 5.1 LITERATURE REVIEW ON THE NUMERICAL METHODS

The development of direct cyclic methods is based on the assumption that the structure under cyclic mechanical loading reaches a stabilized state. The stabilization of the mechanical

---

<sup>1</sup> This is experimentally verified for Shape Memory Alloys, when looking, for instance, at the evolution of the hysteresis area with the number of cycles.

response is the purpose of several works that give conditions for the occurrence of stabilization, independently from initial state and loading path.

#### 5.1.1 Shakedown

Three different asymptotic states are usually defined for a structure subject to cyclic mechanical loadings:

- The elastic shakedown corresponds to an elastic asymptotic state. Inelastic deformations reach constant values, and the total dissipated energy remains bounded with respect to time. This leads to high cycle fatigue.
- The plastic shakedown. In this case, inelastic deformations occur during each cycle but become periodic: they have the same value at the beginning and at the end of the cycle. The dissipated energy reaches a constant value, but the cumulated dissipated energy goes to infinity when time goes to infinity. This leads to low cycle fatigue.
- Ratchetting. It may be possible that the structure never reaches an asymptotic state; the response always evolves between two consecutive cycles. The collapse of the structure occurs in a very low number of cycles.

Different theoretical studies have been performed for elasto-plastic materials to give conditions for the occurrence of one asymptotic state. The first ones are the successive works of [Melan \[1936\]](#) and [Koiter \[1960\]](#), who gave a theorem with sufficient conditions for elastic shakedown of an elastic perfectly plastic material. This condition is path independent, and independent of the initial state of the structure. This work has been successfully extended to other elasto-plastic constitutive laws (see [\[Nguyen, 2003\]](#) and references therein). Three contributions have been published for Shape Memory Alloys. [Feng and Sun \[2007\]](#) use the constitutive law from [Raniecki and Lexcellent \[1998\]](#) and deal with plastic shakedown, in the sense that phase transformation deformation occurs at each cycle. However, [Pham \[2008\]](#) shows that their approach is for different reasons not path independent. [Wu et al. \[1999\]](#) give some results on the shakedown in SMAs but it remains a local approach. Recently, [Peigney \[2010\]](#) states some sufficient conditions for the energy dissipation to remain bounded, independently of the initial state.

In our case, we did not verify that the conditions given by [Peigney \[2010\]](#) are verified, but we assume that the structure reaches an asymptotic state.

#### 5.1.2 Direct methods

The different methods proposed to reduce computation time aim at determining the asymptotic material state directly, without going through the whole loading history (unlike the incremental method, in which the loading history is divided into increments to ensure convergence).

Among these approaches, [Peigney and Stolz \[2003\]](#) propose a method based on the optimal control theory. The asymptotic state is calculated as the solution of a minimization problem. The minimized function represents the elastic energy of a generalized stress field associated to the distance to periodicity (the function is equal to zero when the solution is periodic). A finite-element simulation is developed, introducing the adjoint state of the function.

[Zarka et al. \[1998\]](#) proposed a simplified method, which allows a direct computation of the stabilized cycle based on the introduction of a transformed parameter linked to both the local behavior and to the structural coupling.

A Direct Cyclic Method was developed by [Maitournam et al. \[2002\]](#) based on a method proposed by [Akel and Nguyen \[1989\]](#) to directly calculate the stabilized state and on the Large Time

Increment Method developed by Ladevèze [cf. Boisse et al., 1990]. The LATIN Method separates the equations into the equations for the static and kinematic admissibility (global equations) and the constitutive law, giving the evolution of the internal variables (local equations). The problem is directly solved on the whole loading time, solving iteratively each set of equations until the solution verifies simultaneously both sets. Two time scales are introduced: a large one to capture slow evolutions between cycles, and a small one to capture rapid variations inside a cycle. This allows faster determination of the solution.

In other studies, modified alternative finite elements methods are proposed to allow faster computation of the mechanical response. Namely, Masud and Xia [2006] developed a variational multiscale method following the work of Hughes [1995], in which the displacement field is decomposed into coarse and fine scales, allowing arbitrary combinations of interpolation functions. It has been applied to an SMA constitutive law and leads to interesting gain of computation time. Following the same idea of Hughes [1995], another finite element method have been developed for elastoplasticity by Commend et al. [2004] employing Petrov-Galerkin method.

## 5.2 THE DIRECT CYCLIC METHOD FOR SMA BEHAVIOR

In this section, the Direct Cyclic Method (DCM) is extended to the SMA pseudoelastic behavior: the numerical algorithm is detailed and results in tension, torsion and bending are presented, exhibiting the gain of time allowed by this method.

### 5.2.1 Main ideas

DCM allows accelerated computation, under certain conditions, of the stabilized response of an elastoplastic structure subjected to cyclic thermomechanical loading. This is achieved using a Large Time Increment Method [cf. Boisse et al., 1990] in which periodicity is enforced on the state variables [cf. Maitournam et al., 2002]. The stabilized response is determined without considering the complete loading history and is typically used as an input for fatigue criteria like Moumni's [cf. Moumni et al., 2005]. Compared to the classical incremental technique, DCM was shown to be very time-efficient.

In the case of the cyclic ZM model for shape memory alloys, only approximate periodicity can be achieved in a finite number of cycles. Indeed, the model incorporates a number of parameters and state variables that reach asymptotic values only for infinite cumulated martensite volume fraction (cf. Eq. (2.20)). DCM can still be used, nonetheless, to determine an approximate stabilized state within some predefined tolerance from the exact asymptotic state.

In practice, the Direct Cyclic Method is built around two major concepts:

1. The first is the separation of the global and local simulation stages. The global stage requires the inversion of a linear but usually large system of equilibrium equations over a complete loading cycle, while the local stage typically involves solving nonlinear complementary equations over the same cycle.
2. The second is the explicit enforcement of periodicity on the state variables, since the stabilized solution will necessarily be periodic.

Convergence is achieved once a periodic solution is reached that satisfies the global and local equations simultaneously over a complete cycle.

In the original DCM proposed by Maitournam et al. [2002], a Fourier transform was used to accelerate the computation of the global stage. However, this requires a constant stiffness, to

avoid complex inversion of the stiffness matrix, which can not be assured for the ZM constitutive law.

### 5.2.2 Numerical algorithm

The loading cycle is divided into  $N$  intervals. At each time step  $n = 1 \dots N$ , let  $\mathbf{f}_n$ ,  $\mathbf{T}_n^d$ ,  $\xi_n^d$  be the external body force, the contact forces and the imposed displacement applied. The superscript  $(k)$  denotes the iteration number, one iteration consisting of global and local and periodicity stages.

#### Initialization

An initial estimate of the solution ( $k = 0$ ) is classically determined by solving an elastic problem over the cycle, assuming that the dissipated variables are equal to zero:

$$\forall n = 1 \dots N, z_n^{(k=0)} = z_{e,n}^{(k=0)} = 0 \quad \text{and} \quad \mathbf{B}_n^{(k=0)} = \epsilon_{\text{ori},n}^{(k=0)} = \epsilon_{r,n}^{(k=0)} = 0. \quad (5.1)$$

#### Global stage

The global stage aims to calculate stress and strain fields that are kinematically and statically admissible throughout the loading cycle by solving at the  $k$ -th iteration:

$$\begin{aligned} \forall n = 1 \dots N, \operatorname{div} \left( \sigma_n^{(k)} \right) + \mathbf{f}_n &= 0 \quad \text{in } \Omega \\ \xi_n^{(k)} &= \xi_n^d \quad \text{in } \partial\Omega_\xi \\ \sigma_n^{(k)} \cdot \mathbf{n} &= \mathbf{T}_n^d \quad \text{in } \partial\Omega_\Gamma \end{aligned} \quad (5.2)$$

The internal variables are assumed to be known from a previous iteration ( $k - 1$ ) or from initial conditions ( $k = 0$ ) and are kept constant during this stage:

$$\forall n = 1 \dots N, z_n^{(k)} = z_n^{(k-1)}, z_{e,n}^{(k)} = z_{e,n}^{(k-1)}, \mathbf{B}_n^{(k)} = \mathbf{B}_n^{(k-1)}, \epsilon_{\text{ori},n}^{(k)} = \epsilon_{\text{ori},n}^{(k-1)}, \epsilon_{r,n}^{(k)} = \epsilon_{r,n}^{(k-1)}. \quad (5.3)$$

For instance, the global stage for  $k = 0$  is the resolution of elastic problems over the whole cycle, because the dissipative variables are equal to zero (cf. Eq. (5.1)). A weak form of the equilibrium equations (5.2) is given by:

$$\forall \mathbf{w} \in C, \int_{\Omega} \sigma_n^{(k)} : \epsilon[\mathbf{w}] \, dV = \int_{\Omega} \rho \mathbf{f}_n \cdot \mathbf{w} \, dV + \int_{\partial\Omega_\xi} \mathbf{T}_n^{(k)} \cdot \mathbf{w} \, dS + \int_{\partial\Omega_\Gamma} \mathbf{T}_n^d \cdot \mathbf{w} \, dS. \quad (5.4)$$

where  $\mathbf{w}$  is a test function belonging to  $C$ , group of displacement fields which are continuous and regular over  $\Omega$ , and  $\mathbf{T}_n^{(k)}$  is the reaction associated with the prescribed displacement  $\xi_n^d$  on the part of the boundary  $\partial\Omega_\xi$  where prescribed displacements are imposed. Introducing the constitutive law (2.74) in this weak form gives:

$$\begin{aligned} \forall \mathbf{w} \in C, \int_{\Omega} \epsilon_n^{(k)} \left[ \xi_n^{(k)} \right] : \mathbf{K}_n^{(k)} : \epsilon[\mathbf{w}] \, dV &= \int_{\Omega} \rho \mathbf{f}_n \cdot \mathbf{w} \, dV + \int_{\partial\Omega_\xi} \mathbf{T}_n^{(k)} \cdot \mathbf{w} \, dS \\ &+ \int_{\partial\Omega_\Gamma} \mathbf{T}_n^d \cdot \mathbf{w} \, dS + \int_{\Omega} \left( \epsilon_{r,n}^{(k)} + z_n^{(k)} \epsilon_{\text{ori},n}^{(k)} \right) : \mathbf{K}_n^{(k)} : \epsilon[\mathbf{w}] \, dV. \end{aligned} \quad (5.5)$$

where  $\xi_n^{(k)}$  is the displacement field solution of the problem (5.2). As the dissipative variables are assumed to be constant during this stage, they are in the right part of the equation. This leads to the classical Galerkin formulation of the problem:

$$[\mathbf{K}]\{\mathbf{U}\} = \{\mathbf{F}\}, \quad (5.6)$$

where  $\{\mathbf{U}\}$  is the generalized displacement vector,  $[\mathbf{K}]$  is the stiffness matrix which depends on the martensite volume fraction  $z$  in the case of the ZM model (cf. Eq. (2.11)), and  $\{\mathbf{F}\}$  is the generalized force vector, in which the inelastic strains are taken into account as nodal forces as long as they are constant during this stage. Inverting this equation allows to obtain the displacement field kinematically admissible. The strain and stress fields are obtained respectively using Eqs. (2.60) and (2.74).

After the global stage, the solution calculated over the whole cycle is checked for periodicity and admissibility with the constitutive laws:

- *Periodicity*: This has sense only until the second iteration, since the test for periodicity is done at the end of the local stage. If the test (5.8) is satisfied, then the periodicity condition is reached.
- *Admissibility* with the constitutive laws:

$$\forall n = 1 \dots N, \mathcal{F}_z^1 \left( \sigma_n^{(k)}, z_n^{(k)}, \mathbf{B}_n^{(k)}, z_{e,n}^{(k)} \right) \stackrel{?}{\leq} 0 \text{ and } \mathcal{F}_z^2 \left( \sigma_n^{(k)}, z_n^{(k)}, \mathbf{B}_n^{(k)}, z_{e,n}^{(k)} \right) \stackrel{?}{\leq} 0 \quad (5.7)$$

If these two conditions are fulfilled, the solution, which is also kinematically and statically admissible with the input data, is the stabilized response of the material. If the admissibility and periodicity requirements are not met, local and periodicity stages are computed, and then another iteration is carried. This process stops when the difference between the periodic quantities kinematically and statically admissible and the quantities admissible with the constitutive laws is small.

#### Local stage

The local stage modifies the internal variables and the stress field over the whole cycle in order that the constitutive law (Eqs. (2.74), (2.28), (2.29), (2.30)) is verified at each load increment. The increments of the internal variables are determined using the return mapping algorithm described in Table 4.

After the local stage, the solution is checked for periodicity and the result of this test is saved until the end of the next global stage:

$$\text{for } f = \{\mathbf{B}, \epsilon_r, \gamma\}, \left| f_N^{(k)} - f_0^{(k)} \right| \stackrel{?}{\leq} \text{tolerance} \quad (5.8)$$

where  $f_0$  and  $f_N$  are the values of the field at the initial and final time of the loading cycle respectively.

#### Periodicity

The periodicity condition is then enforced on variables  $\mathbf{B}$ ,  $\epsilon_r$  and  $z_e$ :

$$\text{for } f = \{\mathbf{B}, \epsilon_r, \gamma\}, f_0^{(k+1)} = f_N^{(k)}. \quad (5.9)$$

This guarantees the periodicity of the other variables, namely the stress  $\sigma$ , and the material parameters that depend on  $z_e$  (i.e.  $a, b, G, \alpha, \beta, \gamma, \xi, \kappa$ ).

The algorithm for the Direct Cyclic Method adapted for use with the ZM model is given in Table 11.

---

Input: model parameters, loading cycle discretized into  $N$  intervals, initial and boundary conditions.

Output: stabilized stress, strain and internal variables fields over the loading cycle.

1. Initialization: Set  $k = 0$  and set the dissipative variables equal to zero for each load increment (Eqs. (5.1))
  2. Global stage: For each load increment  $n = 1 \dots N$ :
    - Set the dissipative variables to their values at the end of the previous iteration using Eq. (5.3).
    - Calculate the parameters ( $a, b, G, \alpha, \beta, \gamma, \xi, \kappa$ ) that depend on  $z_e$  with Eq. (2.20),
    - Update the stiffness matrix according to Eq. (2.11) and compute the generalized forces from the right-hand part of Eq. (5.5),
    - Calculate the displacement increments by solving Eq. (5.6),
    - Calculate the strain and stress fields (cf. Eqs. (2.60) and (2.74)).
  3. End test: If conditions (5.8) (periodicity of the variables) and (5.7) (admissibility with the constitutive law) are fulfilled throughout the loading cycle, then the solution is the stabilized cycle: exit. Else, continue with local stage.
  4. Local stage: For each load increment  $n = 1 \dots N$ , if condition (5.7) is not met, compute the increments of internal variables using the return mapping algorithm (cf. Table 4).
  5. Periodicity condition: For  $f = \{\mathbf{B}, \epsilon_r, \gamma\}$ , set  $f_0 = f_N$  (Eq. (5.9)).
  6. Set  $k = k + 1$  and go to 2.
- 

Table 11. Algorithm for the Direct Cyclic Method.

### 5.2.3 Results

In order to evaluate the efficiency of the Direct Cyclic Method in determining the asymptotic response of a superelastic shape memory structure, three finite element analyses are performed using the finite element code Cast3M. For all simulations, the material parameters used in the analysis are listed in Table 12. The temperature is taken as 50 °C, which is greater than the reverse transformation finish temperature  $A_f^0$ .

Parameters values			
$E_A$	70000 MPa	$E_M$	45000 MPa
$a^{(0)}$	1.3043 MPa	$a^{(sat)}$	0.42184 MPa
$b^{(0)}$	0.47845 MPa	$b^{(sat)}$	0.21504 MPa
$G^{(0)}$	2.8826 MPa	$G^{(sat)}$	1.3236 MPa
$\gamma^{(0)}$	0.96 %	$\gamma^{(sat)}$	0.37 %
$\alpha^{(0)}$	8333.3 MPa	$\alpha^{(sat)}$	21622 MPa
$\beta^{(0)}$	16667 MPa	$\beta^{(sat)}$	43243 MPa
$\xi^{(0)}$	0.09497 MPa/°C	$\xi^{(sat)}$	0.05631 MPa/°C
$\kappa^{(0)}$	0.7314 MPa	$\kappa^{(sat)}$	0.71784 MPa
$(A_f^0)^{(0)}$	42 °C	$(A_f^0)^{(sat)}$	42 °C
$\nu$	0.3	$\epsilon_r^{sat}$	0.5914 %
$\tau$	8.64	$Y$	80 MPa
$B^{sat}$	160 MPa		

Table 12. Model parameters

#### Tensile test

The first simulation is related to the behavior of an SMA cylinder of 100 mm in length and 5 mm in diameter subjected to cyclic tensile loading. One end of the cylinder is cantilevered and the other is subject to pressure that increases monotonically from 0 to 500 MPa in equal steps of 5 MPa. The remaining part of the boundary is free. The system has a total of 2142 degrees of freedom. DCM is used to determine the asymptotic state of the structure and the result is compared to the one obtained by incremental calculation over the first 20 loading cycles. Fig. 68a shows a comparison of the stress-strain curves obtained using both methods at the center of the cylinder's midsection. Only the last cycle obtained using DCM is physically relevant whereas all 20 cycles determined using the classical method are. The stress-strain curves for the last cycle are similar for both methods (see Fig. 68b) with DCM being 4.6 times faster (20 times 8364 sec. for the classical method versus 36067 sec. total for DCM). The efficiency of DCM is expected to increase with increasing complexity of the system to be solved.

#### Torsion test

The second simulation is done on the same cylinder (length of 100 mm and radius of 5 mm) subjected to torsion loading. The simulation is performed imposing the torque on one end of

the cylinder, while the other end is cantilevered. The maximum torque is 78 Nm, in equal steps of 1.5 Nm. The results are plotted on Figure 69a and 69b. Even in this case, comparison with the incremental method shows that DCM gives an accurate simulation of the stabilized cycle. The gain of computing time reaches a ratio of 4.

#### *Bending test*

The third simulation is performed on a beam with a square section subject to bending loading. The beam is 50 mm long and its section has an area of 25 mm<sup>2</sup>. One end of the beam is cantilevered, while the other one is subject to a bending force of 12 N in equal steps of 0.3 N. The comparison between the incremental method and the DCM is shown on Figs. 70a to 71b. The stress-strain curves are plotted for two points near the cantilevered section, and symmetric with respect to the neutral plane. In this simulation, DCM is very efficient, because it leads to a gain of time of 7.5.

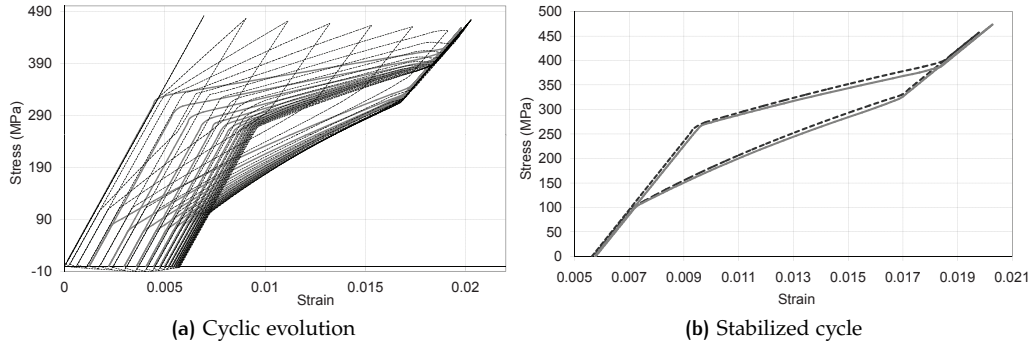


Figure 68. Comparison of the stress-strain curves (a) and of the stabilized cycles (b) obtained using the incremental method (solid line) and the Direct Cyclic Method (dotted line) for a tensile cyclic loading.

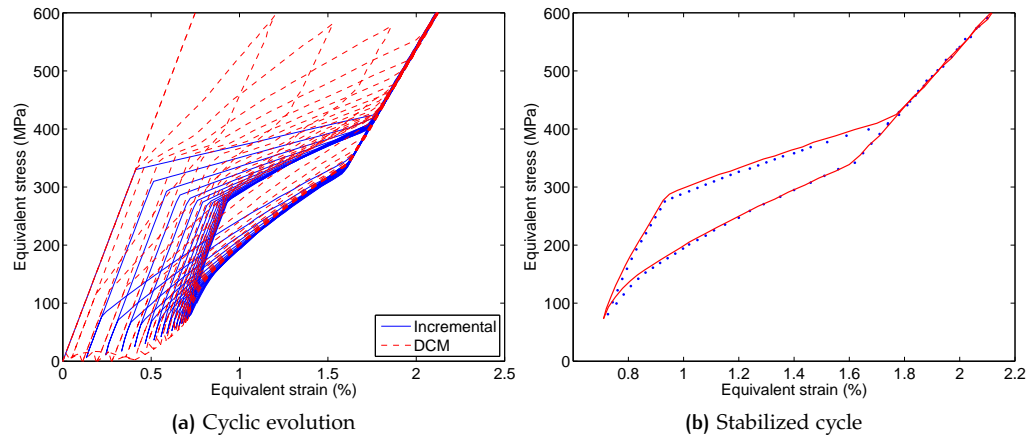


Figure 69. Comparison of the stress-strain curves (a) and of the stabilized cycles (b) obtained using the incremental method (blue curves) and the Direct Cyclic Method (red curves) for a point situated on the external radius of the cylinder which is subject to a torsion loading.

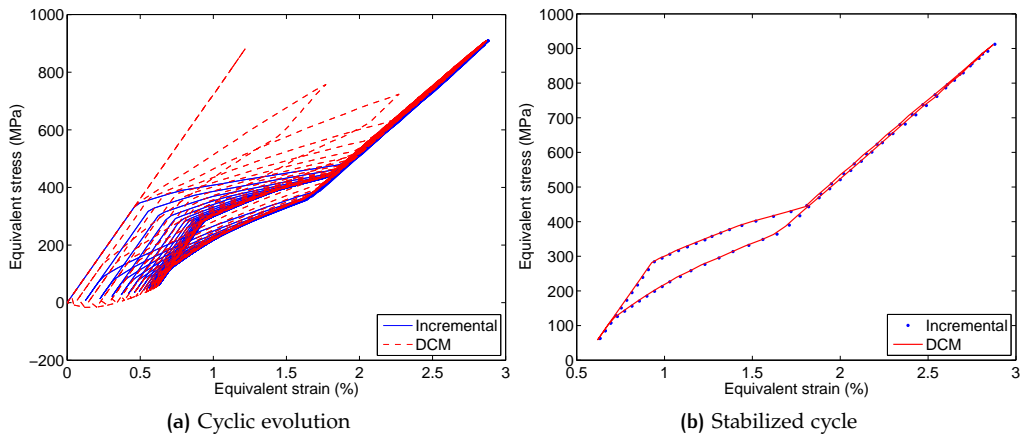


Figure 70. Comparison of the stress-strain curves (a) and of the stabilized cycles (b) obtained using the incremental method (blue curves) and the Direct Cyclic Method (red curves) for a point situated on the upper face in tension, near the cantilevered section. The beam is subject to a bending loading.

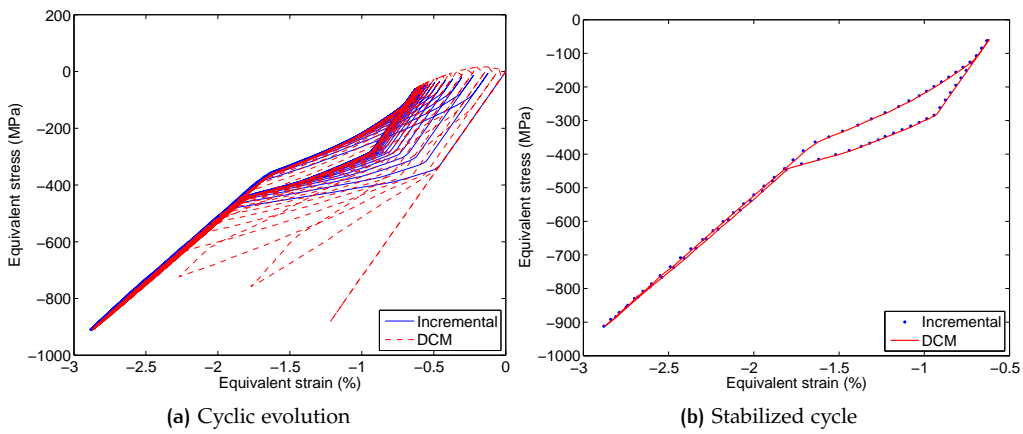


Figure 71. Comparison of the stress-strain curves (a) and of the stabilized cycles (b) obtained using the incremental method (blue curves) and the Direct Cyclic Method (red curves) for a point situated on the lower face in compression, near the cantilevered section. The beam is subject to a bending loading.

## 5.3 CONCLUSION

Numerical computation of the stabilized cycle is of prime importance for the determination of the fatigue lifetime of a structure. However, incremental algorithm such as the one developed in section 2.4.2 leads to high computation time. In order to accelerate convergence, the Direct Cyclic Method, initially developed for elastoplastic materials, was adapted for use with the ZM model. Through a finite element analysis of simple SMA structures subject to tension, torsion and bending, the method was shown to be very efficient as it allowed considerably faster calculation of the asymptotic state of the SMA structure compared to a classical approach that accounts for the complete loading history.

With this chapter, the first and second steps of the global approach for fatigue design of SMAs are completed. Indeed,

- the second chapter explained the choice of the ZM models for this approach and developed the suitable return mapping algorithms required for numerical simulations.
- Chapters 3 and 4 developed important extensions of these models for providing a more accurate prediction of the stabilized cycle.
- Finally, this chapter provides a numerical method for fasten the determination of the stabilized cycle.

Of course, some works remain to unify all these extensions... but this work is intended as a first step for giving to an engineer suitable tools for fatigue design.

The last chapter deals with the third step of the global approach for fatigue design: the determination of the number of cycles to failure of the structure, thanks to a fatigue criterion.

# 6 | FATIGUE

---

6.1	Literature review on the fatigue of SMAs	104
6.1.1	Metallurgical aspects	105
6.1.2	Fatigue criteria	106
6.1.3	Influence of thermomechanical coupling on the fatigue behavior of SMAs	106
6.2	Modified energy-based criterion	108
6.2.1	Tensile-compressive fatigue results from Mounni et al. [2005]	108
6.2.2	Accounting for the role of the hydrostatic pressure in the fatigue criterion	108
6.2.3	Extension to torsion experiments	110
6.3	Prospects	113
6.3.1	Accounting for the influence of thermomechanical coupling	113
6.3.2	Detection of the crack initiation	114
6.4	Conclusion	118

---

This chapter introduces the third step of the comprehensive approach for fatigue analysis. The chapter deals with the development of a low-cycle fatigue criterion capable of predicting the number of cycles to failure of an SMA structure subjected cyclic loadings.

Thermomechanical fatigue of Shape Memory Alloys originates in irreversible modifications of the microstructure of the material, which accumulate while cycling, leading to the failure of the structure. Literature [cf. e.g. Van Humbeeck, 1991; Wagner et al., 2004; Eggeler et al., 2004; Mounni et al., 2005] usually distinguish between two kinds of fatigue for Shape Memory Alloys.

1. *Mechanical fatigue* occurs in a structure subjected to cyclic mechanical loading at imposed strain or load amplitude under constant external temperature. The material may be either martensitic, austenitic or undergo phase change during the loading cycle. Classically, the phenomena associated with mechanical fatigue are a cyclic hardening of the stress-strain plateaus, the appearance of persistent slip bands, and the initiation and propagation of cracks, ultimately leading to the failure of the structure.
2. *Thermal fatigue or amnesia* is the degradation of the material characteristics (physical, mechanical or functional properties), such as the transformation temperatures, the size of the hysteresis loop, the degradation of the two-way shape memory effect. This type of fatigue occurs after thermal or thermomechanical cycling, when the loading path repeatedly crosses the transformation zones.

This chapter focuses the mechanical fatigue.

## 6.1 LITERATURE REVIEW ON THE FATIGUE OF SMAS

The available research on the fatigue behavior of Shape Memory Alloys can be classified into the following groups:

- *Metallurgical investigations* which aim at explaining the cyclic stabilization of the thermomechanical properties of SMAs by the creation of defects, the presence of residual martensite, the creation of persistent slip bands, etc.
- *Development of fatigue criteria.* Tests are performed on different geometries of specimens with different chemical compositions, for different loading cases (rotative bending, tension-compression, torsion...). These tests lead to the establishment of Wöhler curves (also called SN curves) which link the number of cycles to failure to the imposed strain or stress amplitude. Manson-Coffin laws are generally proposed for low-cycle fatigue.
- *Analysis of failure surfaces* to understand crack propagation.

The literature review focuses on the two first points.

#### 6.1.1 Metallurgical aspects

In conventional materials as well as in Shape Memory Materials, surface quality has a detrimental effect on fatigue resistance (especially the surface roughness), by the presence of inclusions, and by the grain size... For Shape Memory Alloys, phase change also participates to the creation of defects.

Melton and Mercier [1979] seem to have pioneered research on fatigue of SMAs. They performed tensile tests on NiTi cylindrical specimens. They showed that the martensite start temperature  $M_s$  does not impact the rate of crack growth in martensite. However, the Paris law they proposed to describe crack growth rate turns out to be dependent on the specimen geometry.

Miyazaki et al. [1986] studied the influence of inclusions on crack initiation. Inclusions act as preferential locations for crack initiation, because they generate geometric incompatibilities and stress concentrations. They showed that similar incompatibilities exist at grain boundaries but, that stress concentration is more important around inclusions. It is thus important to avoid inclusions by specific heat treatment. Moreover, they demonstrated that cracks always initiate at 10 % of the fatigue life. Concerning the influence of temperature on crack growth, they showed that for martensitic materials, a low propagation rate is obtained, because the deformation is due to the movement of intervariant interfaces. Propagation rate increases with temperature: martensite nucleates at crack tip to decrease stress concentration; for increasing temperatures, martensite nucleation becomes more and more difficult as long as austenite becomes more stable, leading to the increase of the crack propagation rate. For high temperature, the material is totally austenitic, the propagation rate is independent of temperature and follows a classical Paris law.

Siredey et al. [2005] performed bending tests on CuAlBe specimens. They showed that one main martensitic variant is induced by bending loading; this leads to an homogeneous stress state in the structure. During cyclic loading, an increasing number of striation patterns is formed in the structure; furthermore, the highest the strain amplitude, the higher the number of striations, and the higher the strain rate, the smaller the spacing of the striations. Siredey et al. [2005] ascribed these patterns to the formation of martensite bands, as they correspond to zones where residual martensite exists. Moreover, they showed that microcracks appear inside the striations. Besides, they demonstrated that a low roughness leads to a higher lifetime, and that single crystals have higher fatigue lifetime than polycrystals.

Nayan et al. [2008] performed tensile fatigue tests on cylindrical specimens, and studied the evolution of phase change yield stress, of the hysteresis area and of the Young modulus.

### 6.1.2 Fatigue criteria

#### 1D criteria

In literature, the fatigue behavior of SMAs is usually analyzed through one-dimensional tests, either tensile-compressive tests or rotating bending experiments on wires or to a less extent torsion tests. The results are usually interpreted in terms of Wöhler curves (SN curves) and different Manson-Coffin laws are proposed. The Manson-Coffin laws that account for thermomechanical coupling will be presented in a later section.

Following [Wagner et al. \[2004\]](#), three types of fatigue can be defined in terms of the number of cycles to failure:

- High-cycle fatigue typically occurs for small strain amplitudes, the response of the material remains elastic in this case and the number of cycles to failure is higher than one million.
- For intermediate strain amplitudes, there is still no stress-induced martensite; however some martensite plates exist locally due to fatigue microcrack initiation.
- For high strain amplitudes, most of the structure undergoes stress-induced martensitic transformation. The number of cycles to failure highly depends on the strain amplitude. This is the domain of low-cycle fatigue.

[Melton and Mercier \[1979\]](#) proposed a Manson-Coffin law to model their fatigue results. It links the plastic strain amplitude to the number of cycles to failure. They also showed that the fatigue limit at room temperature decreases for increasing  $M_s$  temperature. This may be explained by the fact that the more martensite variants are created, the higher number of crack initiation zones.

[Siredey et al. \[2005\]](#) also proposed a Manson-Coffin law to describe the low-cycle fatigue of Shape Memory Alloys under pseudoelastic cyclic loading. The total strain amplitude is linked to the number of cycles to failure for strain amplitude lower than 10 %. For strain amplitudes higher than 10 %, a bigger dispersion of the experimental results is noticed. This can be due to the higher number of martensitic variants as well as to their orientation.

#### 3D criteria

To our knowledge, the only 3D criterion for SMAs was proposed by [Moumni et al. \[2005\]](#). They took advantage of the similarities between low-cycle fatigue of metals and SMAs to propose a criterion based on the hysteresis area at the stabilized cycle. Indeed, pseudoelastic cyclic responses exhibit first a transient response which stabilizes after a few number of cycles (*cf.* Figs. 5 and 72). Assuming that the material spends most of its lifetime in the stabilized response, this fatigue criterion links the hysteresis area at the stabilized cycle to the number of cycles to failure. The criterion is validated for tensile-compressive experiments, but has to be validated for other solicitations. So far, the criterion was validated for uniaxial tensile-compressive loading cases.

### 6.1.3 Influence of thermomechanical coupling on the fatigue behavior of SMAs

It was shown in Chapter 4 that thermomechanical coupling is responsible for important changes in the stress-strain response of SMAs. The following literature review presents the influence of thermomechanical coupling on the fatigue lifetime of SMA structures focusing on loading frequency, temperature, geometry of the specimen, and surrounding medium.

[Matsui et al. \[2004\]](#) and [Tobushi et al. \[1997\]](#) performed rotating-bending experiments on both NiTi wires and cylindrical specimens, and showed that the geometry of the test sample as well as the temperature and the rotation speed influence fatigue resistance. The extent of this influence

depends on whether the tests are carried in the air or in water. More precisely, at constant rotating speed, the water temperature impacts the fatigue lifetime; the rotating speed changes the fatigue lifetime in air but not in water. Matsui et al. [2004] proposed a Manson-Coffin criterion that links the strain amplitude to the number of cycles to failure, in which the exponent of the power law depends on temperature.

Miyazaki et al. [1999] obtained similar results by showing that the fatigue behavior depends on the liquid bath temperature: the higher the temperature, the smaller the lifetime at fixed strain amplitude.

Wagner et al. [2004] performed rotating-bending experiments and considered the influences of the wire diameter and of the rotation speed on the fatigue lifetime of the wires. They showed that, because of the strong thermomechanical coupling existing in SMAs, the influences of wire diameters or rotation speed disappear when the tests are performed in a liquid bath with high convective heat transfer coefficient. In air, the influence of the rotation speed is noticeable for speeds lower than 400 rpm (rotations per minute). The existing dependencies are related to the possibility of the specimen temperature to vary during the test because of thermomechanical coupling: at high rotation speed, the specimen temperature is increased, leading to an increase of the stress level and thus a decrease of the fatigue lifetime. The tensile tests and rotative bending tests performed in a liquid bath by Eggeler et al. [2004] show either pure elastic response or pseudoelastic behavior. The dependence of the fatigue lifetime on temperature and on loading frequency is also investigated. Furthermore, the evolution of the residual strain with respect to these parameters is investigated. These two studies follow on the work of Sawaguchi et al. [2003], who showed that for tests in air, there was a limited influence of wire diameter and rotation speed on fatigue resistance.

Predki et al. [2006] performed torsion experiments on cylindrical and tubular specimens at ambient temperature, without control of the specimen temperature, for frequencies varying between 0.1 and 1 Hz. The authors first studied the evolution of different characteristics of the response (namely maximum shear stress, shear modulus and damping capacity) with the number of cycles and the frequency, underlining the thermomechanical coupling. They also find that the fatigue lifetime changes with the geometry of the specimen, the type of sollicitation (repeated or alternated load) but not as much with the loading frequency.

Paradis et al. [2008] investigated the effect of pausing the loading cycle on the cyclic behavior of SMAs and on their fatigue lifetime: this so-called "pause effect" is a thermal effect, arising from the fact that SMAs under cyclic loading are not in thermal equilibrium with the surroundings; thus, during interruption, the specimen temperature returns to the ambient temperature, and another transient phase occurs when the test is restarted. Likewise, part of the residual strain is recovered during an interruption of the test. They showed that the fatigue lifetime is dependent on whether there is interruptions or not, as the dissipated energy is not the same in both cases.

Figueiredo et al. [2009] obtained unusual results for rotating bending tests on different wires (either martensitic, or austenitic or pseudoelastic); indeed for pseudoelastic tests, a Wöhler curve with a "Z-shape" (high dispersion) was obtained, which was not reported anywhere else in available literature.

To summarize,

- The higher the temperature of the structure, the lower the number of cycles to failure. The temperature may be increased either by performing the experiments in a liquid bath at high temperature, or at high loading rate for experiments performed in air.
- Loading rate changes the fatigue lifetime mainly for experiments in air. This dependence seems to be restricted to a certain range of frequencies.

- Geometry of the specimen also influences the fatigue lifetime for experiments in air, because of thermomechanical coupling.
- Most of the results are given in terms of strain amplitude, which does not give any information on the maximum stress encountered by the structure nor on the hysteresis area.

An energy-based criterion should be able to account for all these dependencies in a unified way.

The next section proposes an extension of the energy criterion developed by [Moumni et al. \[2005\]](#) in order to account for the influence of the hydrostatic pressure.

## 6.2 MODIFIED ENERGY-BASED CRITERION

### 6.2.1 Tensile-compressive fatigue results from [Moumni et al. \[2005\]](#)

We are mainly interested in the low-cycle fatigue of SMAs, for pseudoelastic loading paths, which are characterized by an energy dissipation at each loading cycle. In the literature, the most common low-cycle fatigue criterion is the Manson-Coffin law, linking the number of cycles to failure to the inelastic strain amplitude. However, this criterion is not suitable for non isothermal loading cases, as shown by [Constantinescu et al. \[2004\]](#) for thermal fatigue of elastoplastic metals.

Following [Skelton et al. \[1998\]](#) and [Constantinescu et al. \[2004\]](#), [Moumni et al. \[2005\]](#) proposed an energy-based criterion for pseudoelastic SMAs. After a short transient phase, the pseudoelastic response of the SMA stabilizes, and settles into a closed stress-strain loop. The most important part of the specimen lifetime is spent in the stabilized state. This allows the use of the stabilized response as an indicator of the fatigue lifetime of the specimen. Plotting the hysteresis area as a function of the number of cycles shows that these two quantities are related through a power law (*cf.* Fig. 73). Thus, the proposed criterion is:

$$W_d = m N_f^p, \quad (6.1)$$

where  $W_d$  is the hysteresis area at the stabilized cycle,  $N_f$  the number of cycles to failure, and  $m$  and  $p$  two material parameters. For the tensile-compressive results from [Moumni et al. \[2005\]](#),  $m = 4.92 \text{ MJ/m}^3$  and  $p = -0.3019$ .

In order to estimate the ability of the criterion to predict the lifetime of a structure, it is interesting to plot the number of cycles estimated by the criterion with respect to the number of cycles determined experimentally. This is done in Fig. 74. The more points are located near the first bisector of the plane, the better is the criterion. The dispersion of the experimental results is quantified by two parallel lines: the upper line stands for experimental lifetime three times larger than the estimation, while the lower line stands for estimated lifetime three times larger than experimentally observed. Consequently, points situated above the upper line lead to unsafe situations.

In the next section, we show that the number of these points can be reduced by taking into account the influence of hydrostatic pressure.

### 6.2.2 Accounting for the role of the hydrostatic pressure in the fatigue criterion

Experiments on metals show the importance of accounting for the triaxiality of stress [see, e.g. [Amiable et al., 2006](#)]. Besides, most of the high-cycle fatigue criteria introduce an effect of the hydrostatic pressure on the lifetime.

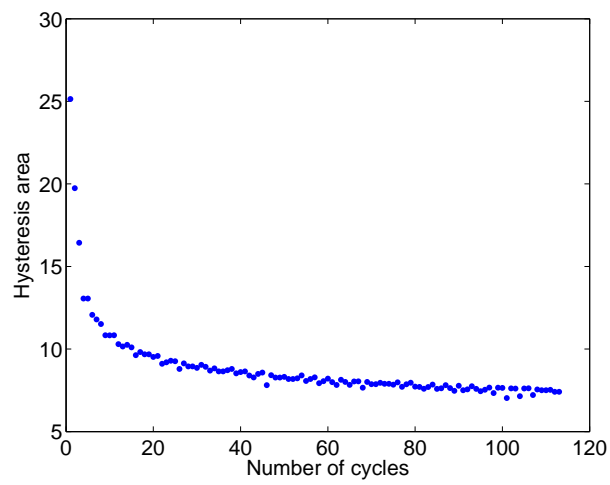


Figure 72. Evolution of the hysteresis area vs. the number of cycles.

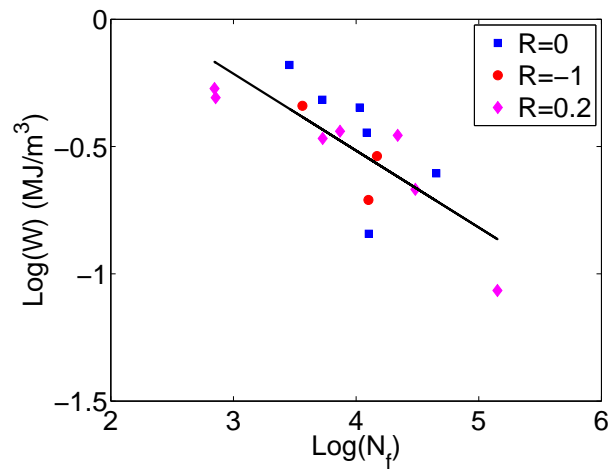


Figure 73. Evolution of the hysteresis area at the stabilized cycle with respect to the number of cycles to failure for the initial energy-based criterion.

We choose to introduce the hydrostatic pressure in the fatigue criterion linearly:

$$W_d + a P_{\max} = m N_f^p \quad (6.2)$$

where  $a$  is a new material parameter. For  $a = 0.0025$ , the results are reported on Fig. 75 ( $m = 5.19 \text{ MJ/m}^3$  and  $p = -0.2196$ ).

It is clear from Fig. 75 that the experimental points are now less scattered. This is confirmed by Fig. 76, which shows the estimated vs. experimental lifetime for the modified criterion (6.2). Like in the previous case, the three black lines stand for one third, one and three times the experimental lifetime. Only one point is situated above three times the experimental lifetime and remains non conservative, but no point is under one third the experimental lifetime. This exhibits the role of the hydrostatic pressure on the fatigue lifetime of SMAs.

### 6.2.3 Extension to torsion experiments

Two series of torsion experiments under imposed torque were performed on cylindrical tubes: alternating torsion ( $R = -1$ ) and pulsating torsion ( $R = 0$ ). The results of the experiments are the torque-angle curves, which stabilize after a few number of cycles. However, the computation of the hysteresis area requires the evaluation of the integral:

$$W = \int_{\text{cycle}} \sigma : \dot{\epsilon} dt. \quad (6.3)$$

A precise computation of the hysteresis area requires finite-element calculations because stress and strain are not uniform in the section. However, assuming thin-wall tubes allows the following simplifications:

- The Navier-Bernoulli assumption allows to neglect the warping function, and to assume that only one component of the stress tensor ( $\sigma_{\theta z}$ ) is not vanishing.
- The thin wall of the cylinder allows to assume that the stress state is uniform in the thickness: thus torque and stress are proportional. Besides, the analytical solution in torsion showed that angle and strain are also proportional.

$$\begin{aligned} \sigma_{\theta z} &= \frac{1}{R_e^3 - R_i^3} \frac{3C}{2\pi}, \\ \epsilon_{\theta z} &= \frac{\phi}{2h} R_e, \end{aligned} \quad (6.4)$$

where  $C$  is the torque,  $R_i$  and  $R_e$  are the internal and external radii of the cylinder,  $h$  the height, and  $\phi$  the measured angle. This gives:

$$W = \int_{\text{cycle}} \sigma_{\theta z} \dot{\epsilon}_{\theta z} dt = \frac{1}{R_e^3 - R_i^3} \frac{3}{4\pi} \frac{1}{h} R_e \int_{\text{cycle}} C \dot{\theta} dt. \quad (6.5)$$

The multiplying constant is function of the geometric parameters of the tube.

The quantity  $W + aP_{\max}$  vs. the number of cycles to failure for both tension-compression and torsion experiments is plotted in a log-log graph on Fig. 77. The values of the criterion parameters are:  $a = 0.0058$ ,  $m = 12.084 \text{ MJ/m}^3$  and  $p = -0.3151$ . The corresponding graph plotting the number of cycles estimated by the criterion vs. number of cycles experimentally observed is given in Fig. 78. On Fig. 78, some points remain above three times the experimental lifetimes. They all correspond to repeated torsion ( $R = 0$ ), with imposed torque. However,

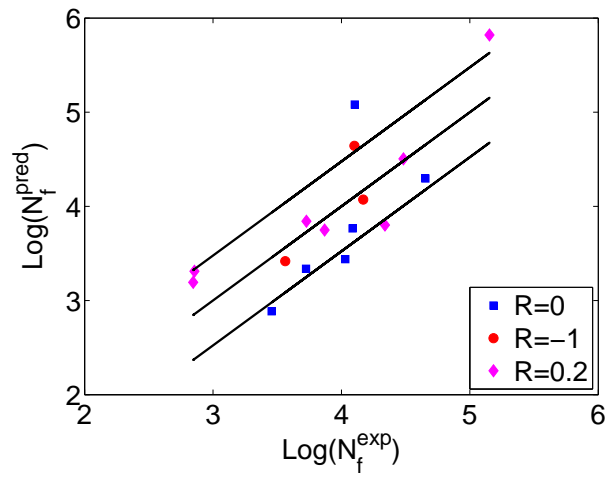


Figure 74. Estimated vs. experimental lifetime for the experiments at different R ratios for the energy-based criterion.

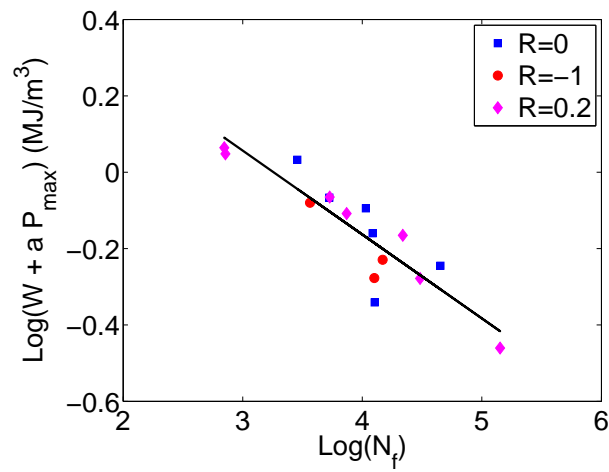


Figure 75. Modified energy-based criterion

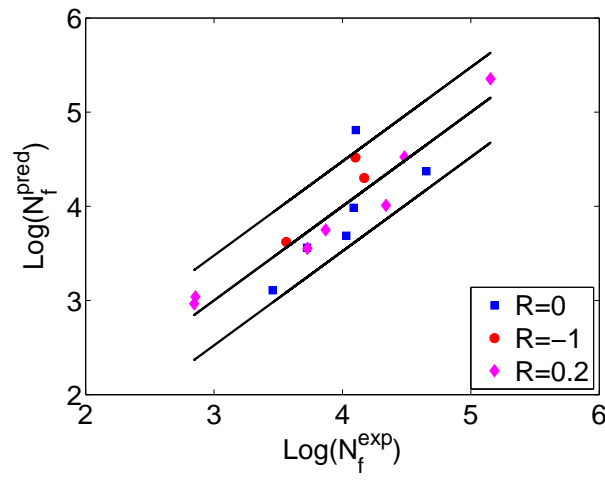


Figure 76. Estimated vs. experimental lifetime for the modified energy-based criterion.

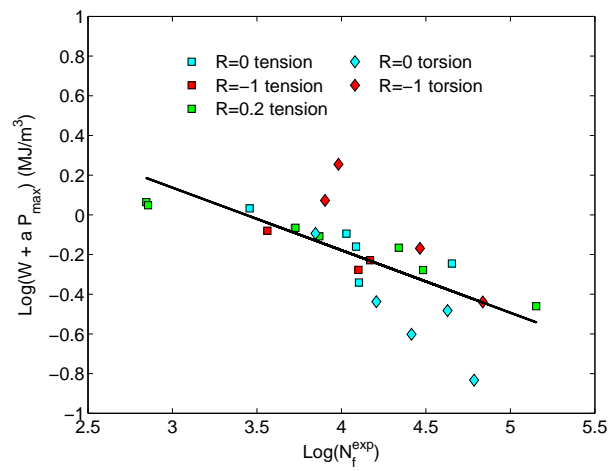


Figure 77. Modified energy-based criterion for tension and torsion experiments.

points associated with alternated torsion are located between the two lines, and the criterion seems to apply. We do not have a physical explanation for the points that do not verify the criterion, except to check the reproducibility of the tests. The validation of the modified energy-based criterion for torsion experiments has to be performed with more precision, by submitting all specimens to the same thermomechanical treatment before testing, and by ensuring uniform thermal boundary conditions. Furthermore, the hysteresis area is very small for these specimens.

## 6.3 PROSPECTS

The following section presents prospective works, dealing with the influence of the thermomechanical coupling on the fatigue lifetime.

### 6.3.1 Accounting for the influence of thermomechanical coupling

The literature review in section 6.1.3 underlined the importance of thermomechanical coupling for the determination of the fatigue lifetime of the SMA. The modified energy-based criterion may be able to account for the observed dependencies.

Most of the tests presented in the review were rotating bending experiments. In these tests, the strain amplitude is imposed by the curvature of the wire, but the maximum stress is determined by the constitutive law. It follows that the higher the temperature, the higher the stress, because of higher phase change yield stress at higher temperature. It is thus possible that the presence of the maximum hydrostatic pressure in the fatigue criterion accounts for the dependence on temperature. It is also established that temperature has little influence on the hysteresis area.

Concerning the dependence on the loading frequency, this seems to happen only for tests performed in air and in a certain range of frequency. For the different series of tests, we tried to compare the frequency for which the maximum of hysteresis area is obtained with the tested frequencies. Indeed, [He and Sun \[2010\]](#) showed that the maximum of hysteresis area is reached for a frequency such that the characteristic loading time  $t_T$  (equal to the time of heat generation) is equal to the characteristic time of heat transfer  $t_h$ , defined by:

$$\begin{aligned} t_T &= \frac{\gamma}{\dot{\epsilon}}, \\ t_h &= \frac{\rho C_p R}{2h}. \end{aligned} \tag{6.6}$$

where  $\rho$  is the density,  $C_p$  the specific heat capacity,  $R$  the radius of the wire,  $h$  the convective heat transfer coefficient,  $\gamma$  the size of the phase change plateau, and  $\dot{\epsilon}$  the strain rate. It seems that the maximum of influence is observed for frequencies near the peak of the hysteresis area curve (*cf.* Fig. 43). For example, for the experiments performed by [Predki et al. \[2006\]](#), and according to [He and Sun \[2010\]](#), the maximum of hysteresis area should be located at a frequency of 0.01 Hz which is far smaller than the tested frequencies: this can explain that no dependence was found. Besides, for strain rates larger than the peak, the maximum temperature of the specimen reaches an upper limit (as the specimen cannot dissipate more energy than the latent heat, temperature cannot increase indefinitely, [\[He and Sun, 2010\]](#)), and thus the maximum hydrostatic pressure should be constant with the frequency.

Furthermore, when the frequency is increased, the specimen temperature increases because of thermomechanical coupling, leading to an increase of the slope of the phase change plateaus, and thus of the maximum hydrostatic pressure at fixed strain amplitude (*cf.* e.g. Fig. 52). Both quantities (hysteresis area and hydrostatic pressure) change with varying frequencies, allowing the modified energy-based criterion to account for the influence of frequency.

Accounting for the hysteresis area in the fatigue criterion should be able to reproduce the dependence on geometry, and more precisely on the radius (cf. e.g. Fig. 45b).

From the above discussion, it seems interesting to conduct the same tests with precise measurements of the hysteresis area and of the maximum hydrostatic pressure to validate the modified energy-based criterion. This would validate the hysteresis area as a relevant parameter for fatigue life prediction. We tried to postprocess fatigue data from literature, to evaluate the relevance of these ideas. We used the rotative-bending experiments from Matsui et al. [2004] and evaluated the quantities of the fatigue criterion as follows:

- the maximum hydrostatic pressure is evaluated for each strain amplitude with the quasi-static curves at the three temperatures of the tests. No change due to thermomechanical coupling is accounted for;
- the hysteresis area is equal to zero if the strain amplitude leads to an elastic response, and is equal to a fraction of the total area proportional to the strain amplitude if phase change occurs.

The values are reported in Fig. 79, where the influence of the hydrostatic pressure is accounted for with a coefficient  $\alpha$  of 0.003. Then, estimated vs. experimental lifetimes are reported on Fig. 80 and are compared to the Manson-Coffin temperature-dependent criterion of Matsui et al. [2004]:

$$\epsilon_a N_f^\beta = \alpha_s 10^{-\alpha(T-M_s)}, \quad (6.7)$$

with  $\beta = 0.28$ ,  $\alpha_s = 0.248$  and  $\alpha = 0.0032 \text{ K}^{-1}$ . The results seem quite satisfactory as the determination of the modified energy is not precise. Indeed, five points are situated above the upper line of our criterion, and four points for the Manson Coffin law from Matsui et al..

Similar rotating-bending experiments have been undertaken in the laboratory. For the moment, three temperatures were tested at two different strain amplitudes. The first results are given on Figs. 81 and 82. Our experimental setup generates high stress concentrations near the attachments, which change the lifetime. Further investigation has to be done to give final conclusions.

### 6.3.2 Detection of the crack initiation

We aim at designing the SMA's structure resistant to crack initiation as a way to increase fatigue resistance. This requires a tool to detect crack initiation. A previous work [Gloanec et al., 2010] leads us to the idea that the hysteresis area would change near the crack initiation, because of the energy dissipated by the crack. This was observed during one interrupted fatigue test, and microscopic simultaneous observations allowed to link the peak of hysteresis area to crack initiation. However, for the eight fatigue experiments we performed on NiTi cylindrical specimens, no peak of hysteresis area was observed. It is possible to use acoustic emission techniques in order to predict the initiation of cracks (crack initiation is interpreted in terms of self-organized criticality), but this is beyond the scope of the present thesis.

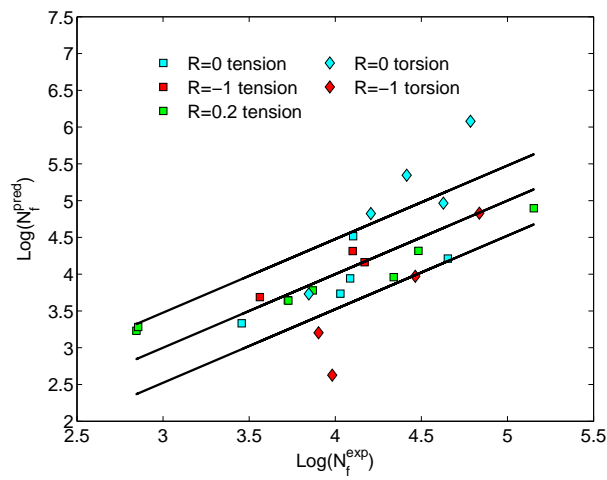


Figure 78. Estimated vs. experimental lifetimes for the modified energy-based criterion for both tension and torsion tests.

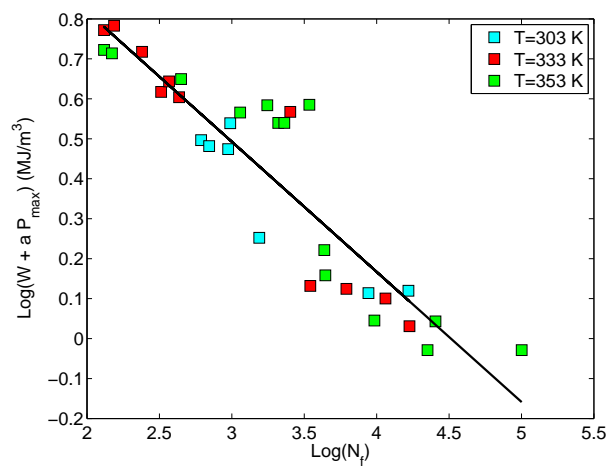


Figure 79. Modified energy-based criterion for the rotating-bending experiments performed by Matsui et al. [2004].

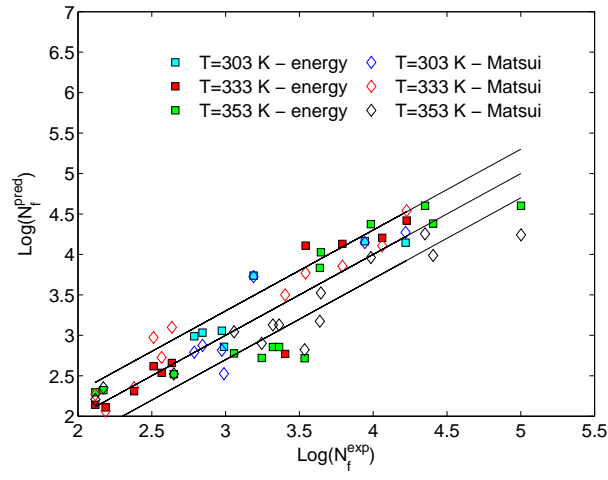


Figure 80. Estimated vs. experimental lifetime given by the modified energy-based criterion (squares) and by the Manson-Coffin criterion from Matsui et al. [2004] (diamonds).

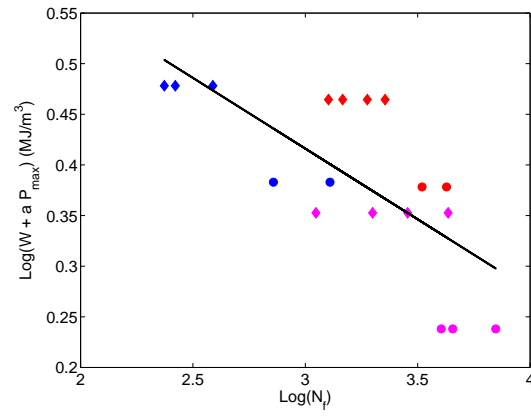
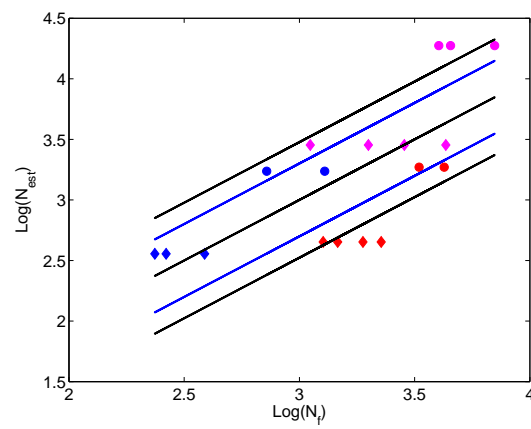


Figure 81. Modified energy-based criterion for our rotating-bending experiments. Diamonds (resp. circles) stand for strain amplitude of 2.5 % (resp. 2 %). Red (resp. blue and magenta) points stand for experiments performed at 50 °C (resp. 70 °C and 35 °C).



**Figure 82.** Estimated vs. experimental lifetime for the modified energy-based criterion. Diamonds (resp. circles) stand for strain amplitude of 2.5 % (resp. 2 %). Red (resp. blue and magenta) points represent experiments performed at 50 °C (resp. 70 °C and 35 °C). The blue lines stand for two and half the experimental lifetime, while the external black lines represent three and third the experimental lifetime.

## 6.4 CONCLUSION

This chapter is an attempt towards the validation of the energy-based fatigue criterion, first proposed by [Moumni et al. \[2005\]](#) for low-cycle fatigue of SMAs. The criterion was extended to take into account the influence of the maximum hydrostatic pressure. The modified energy-based criterion is shown to better predict the fatigue lifetime of SMAs. An attempt to validate the criterion for torsion experiments was presented; the results can be improved by performing all tests under the same experimental conditions. Finally, preliminary results regarding the influence of the thermomechanical coupling on the fatigue lifetime of SMAs have been given: it was shown that the modified energy-based criterion could suitably account for this influence. However, many experiments are required in order to validate the energy criterion for general loading conditions.

This chapter constitutes the third important step of the global method for fatigue design: the prediction of the fatigue lifetime of SMA structure from the knowledge of the stabilized thermomechanical state of the structure.

## 7 | CONCLUSION

We proposed a comprehensive approach for fatigue analysis of Shape Memory Alloys. Shape Memory Alloys are mainly subject to cyclic loadings and thus have to be designed against fatigue. Assuming that the fatigue properties must be deduced from the characteristics of the stabilized cycle, our approach proposed three main steps.

The first step, developed in Chapters 2, 3, 4, is the determination of a cyclic constitutive law, able to reproduce the main features of the SMA behavior. These features were identified as the modification of the stress-strain response due to microstructure degradation occurring during cyclic loadings, the tensile-compressive asymmetry and the thermomechanical coupling due to the strong dependence of yield stresses on temperature and to the presence of a latent heat. The first property was already accounted for in the ZM cyclic model. Tensile-compressive asymmetry has been added by making the yield criterion depend on both second and third invariants of quantities of interest. The extension of the model was shown to quantitatively reproduce both experimental pseudoelasticity and martensite orientation in tension and compression, as well as direct phase change yield stresses in tension, compression and shear over a large range of temperature. Thermomechanical coupling was introduced in both monocytle and cyclic models by coupling mechanical equations (equilibrium and constitutive equations) and heat equation. The main tendencies of the thermal response were correctly reproduced, and the evolution of the mechanical response (especially the hysteresis area and the maximum hydrostatic pressure) was quantitatively captured. For cyclic loadings, our constitutive law now accounts for both microstructure degradation and thermomechanical coupling.

The second step, detailed in Chapter 5, is the development of an original numerical method for the computation of the stabilized cycle. Indeed, incremental resolution is very time consuming. The Direct Cyclic Method, extended to SMA constitutive laws, allows interesting gain of computation time. It is however limited to the isothermal case.

Finally, the third step, developed in Chapter 6, deals with fatigue. The fatigue criterion is based on the characteristics of the stabilized cycle, and links the number of cycles to failure to an energetic quantity, defined as a linear combination between the hysteresis area and the maximum hydrostatic pressure. Results from literature show that this kind of modified energy criterion should be able to account for dependencies of the fatigue lifetime on temperature and frequency in a unified way.

To summarize, our approach can be used as follows: knowing the geometry of the structure and the thermomechanical loading path, the cyclic constitutive law allows the determination of its asymptotic thermomechanical state by incremental resolution. If the structure is thin enough or if the convective heat transfer is sufficiently important, the assumption of isothermal response can be made and the Direct Cyclic Method can be used to fasten the determination of the stabilized state. Then, the fatigue criterion can be computed at each point of the structure. The critical point, at which microcrack will initiate, is determined as the point where the energetical quantity is maximum. The lifetime of the structure is determined at this point.

Main prospects concern non proportional loadings and fatigue.

The major part of this work assumed proportional loadings: the constitutive law has been validated only for such kind of loadings; experiments will be performed to validate the model

for non proportional loadings. This work is of prime importance, as industrial structures generally involve complex geometries and complex thermomechanical loading paths, which imply simultaneous occurrence of martensite reorientation and phase change. The fatigue criterion will be validated for larger range of solicitations, including in-phase and out-of-phase loading paths, under different thermal conditions. Both works will be undertaken in collaboration with Henri Tudor Institut at Luxembourg, in a common research project on fatigue design of stents, which are submitted to complex thermomechanical solicitations. Furthermore, collaboration with university of Hong Kong is underway for research on fatigue (influence of grain size, ...).

This work will also be continued with the study of fracture mechanics for shape memory alloys. In fact, experimental and numerical determination of fracture parameters of SMA ( $J$  integral, stress intensity factors, energy release  $G$ , and fracture toughness) seem to be new issues which can help designing SMA structures. This work is undertaken in collaboration with the department of Mechanical Engineering of Bogazici University at Istanbul.

# A | THERMODYNAMICS OF IRREVERSIBLE PROCESSES

---

A.1	First law of thermodynamics: energy balance	121
A.2	Kinetic energy theorem	122
A.3	Second law of thermodynamics	122
A.4	Clausius-Duhem inequality	122

---

## A.1 FIRST LAW OF THERMODYNAMICS: ENERGY BALANCE

Let us consider a system  $\mathcal{S}$  occupying a volume  $\Omega$  (boundary surface  $\partial\Omega$ ). Its thermodynamic state is defined by the values of a finite number of fields defined for each configuration. Let  $\mathbf{U}$  be a velocity field.

The first law of thermodynamics states that there is a function of the thermodynamic state of the system, called "internal energy"  $\mathcal{E}$ , verifying at each time the equality:

$$\dot{\mathcal{E}} + \mathcal{K} = \mathcal{P}_e + Q, \quad (\text{A.1})$$

where the dot stands for the material derivative of the field,  $\mathcal{K}$  is the kinetic energy of the system,  $\mathcal{P}_e$  is the power of external forces exerted on the system, and  $Q$  is the amount of heat received by the system.

The classical assumption of absence of forces acting at distance is made. If  $\mathbf{F}$  are the body force densities and  $\mathbf{T}$  the surface forces exerted on the system (both quantities may depend on the point  $\mathbf{x}$  and on the time  $t$ ):

$$\mathcal{P}_e = \int_{\Omega} \rho \mathbf{F} \cdot \mathbf{U} d\Omega + \int_{\partial\Omega} \mathbf{T} \cdot \mathbf{U} da, \quad (\text{A.2})$$

$$\mathcal{K} = \int_{\Omega} \frac{1}{2} \rho \mathbf{U}^2 d\Omega. \quad (\text{A.3})$$

The amount of heat received by the system results from a volume contribution  $r$  and a surface contribution  $q_s$ , which may also depend on the point  $\mathbf{x}$  and on the time  $t$ :

$$Q = \int_{\partial\Omega} q_s da + \int_{\Omega} r d\Omega. \quad (\text{A.4})$$

The heat density  $r$  is assumed to be identical for the whole system  $\mathcal{S}$ . Finally, we assume that the internal energy is an extensive function, thus:

$$\mathcal{E} = \int_{\Omega} \rho e d\Omega. \quad (\text{A.5})$$

Eq. (A.1) becomes:

$$\int_{\Omega} \frac{d}{dt} \left( \rho e + \rho \frac{\mathbf{u}^2}{2} \right) = \int_{\Omega} (\rho \mathbf{F} \cdot \mathbf{u} + r) d\Omega + \int_{\partial\Omega} (\mathbf{T} \cdot \mathbf{u} + q_s) d\alpha. \quad (\text{A.6})$$

## A.2 KINETIC ENERGY THEOREM

This theorem is a specific case of the virtual work principle for real motion. It states that, in a Galilean reference frame:

$$\mathcal{P}_e + \mathcal{P}_i = \dot{\mathcal{K}} \quad (\text{A.7})$$

where  $\mathcal{P}_i$  is the power of internal forces expressed by<sup>1</sup>:

$$\mathcal{P}_i = - \int_{\Omega} \boldsymbol{\sigma} : \dot{\boldsymbol{\epsilon}} d\Omega, \quad (\text{A.8})$$

where  $\boldsymbol{\sigma}$  is the Cauchy stress tensor, and  $\boldsymbol{\epsilon}$  the strain tensor associated with the displacement  $\mathbf{u}$ .

Thus, the first law of thermodynamics becomes by application of the Ostrogradsky's theorem,<sup>2</sup>:

$$\rho \dot{e} = \boldsymbol{\sigma} : \dot{\boldsymbol{\epsilon}} + r - \text{div } \mathbf{q}, \quad (\text{A.9})$$

## A.3 SECOND LAW OF THERMODYNAMICS

The second law states the existence of an absolute temperature  $T$  and of an extensive function of the thermodynamic state called entropy, such that:

$$\forall t, \int_{\Omega} \rho \dot{s} d\Omega \geq \int_{\Omega} \frac{r}{T} d\Omega - \int_{\partial\Omega} \frac{\mathbf{q} \cdot \mathbf{n}}{T} d\alpha. \quad (\text{A.10})$$

The local form is:

$$\forall t, \rho \dot{s} - \frac{r}{T} + \text{div} \left( \frac{\mathbf{q}}{T} \right) \geq 0. \quad (\text{A.11})$$

## A.4 CLAUSIUS-DUHEM INEQUALITY

Gathering the expression of the internal energy (A.9) and the inequality of entropy (A.11), we get:

$$\boldsymbol{\sigma} : \dot{\boldsymbol{\epsilon}} + \rho (T \dot{s} - \dot{e}) - \frac{\mathbf{q}}{T} \cdot \nabla T \geq 0. \quad (\text{A.12})$$

A partial Legendre-Fenchel transformation on the internal energy gives the Helmholtz free energy:

$$\mathcal{W} = e - Ts. \quad (\text{A.13})$$

<sup>1</sup> assumption of small perturbations

<sup>2</sup>  $q_s = -\mathbf{q} \cdot \mathbf{n}$  with  $\mathbf{q}$  flow heat through the surface and  $\mathbf{n}$  the outer normal vector of the surface.

Eq. (A.12) becomes:

$$\mathcal{D} = \boldsymbol{\sigma} : \dot{\boldsymbol{\epsilon}} - \rho (\dot{\mathcal{W}} + s\dot{T}) - \frac{\mathbf{q}}{T} \cdot \nabla T \geq 0. \quad (\text{A.14})$$

This is the Clausius-Duhem inequality.  $\mathcal{D}$  is the dissipation, usually split into:  $\mathcal{D} = \mathcal{D}_1 + \mathcal{D}_2$ , where:

$$\mathcal{D}_1 = \boldsymbol{\sigma} : \dot{\boldsymbol{\epsilon}} - \rho (\dot{\mathcal{W}} + s\dot{T}), \quad (\text{A.15})$$

$$\mathcal{D}_2 = -\frac{\mathbf{q}}{T} \cdot \nabla T. \quad (\text{A.16})$$

$\mathcal{D}_1$  is the intrinsic dissipation and  $\mathcal{D}_2$  is the thermal dissipation. Both dissipations are assumed to be separately positive.

# B | GENERALIZED STANDARD MATERIALS WITH INTERNAL CONSTRAINTS

---

B.1	Normal state variables	124
B.2	Method of two potentials	125
B.3	Case of dependent state variables	126

---

The ZM model is developed within the framework of Generalized Standard Materials with internal constraints [Halphen and Nguyen, 1975; Moumni et al., 2008] in order to guarantee thermodynamic consistency. An overview of this framework is provided in this section.

## B.1 NORMAL STATE VARIABLES

The thermodynamic framework is the Thermodynamics of Irreversible Process [*cf.* Germain et al., 1983].

The axiom of local state suggests that the state of a thermodynamic system is entirely determined by a finite number of variables that are defined at each point and at each instant: the state variables. Helmholtz (1883) introduced the concept of normal state variables, assuming that for each thermodynamic system, at least one set of normal state variables may be introduced. A set of state variables is normal if [*cf.* Duhem, 1997]:

- the temperature is one of the variables, and no internal constraint exists between temperature and the other state variables;
- the other variables  $\chi_i$  are such that an arbitrary variation of temperature may be imposed, maintaining the other state variables constant and without any power of internal forces  $\mathcal{P}_i$  developed:

$$\forall \dot{T}, \dot{\chi}_i = 0 \Rightarrow \mathcal{P}_i = 0. \quad (\text{B.1})$$

The power of internal forces is given by:

$$\mathcal{P}_i = - \int_{\Omega} \boldsymbol{\sigma} : \dot{\mathbf{e}} d\Omega. \quad (\text{B.2})$$

Thus, the macroscopic strain is one of the state variables. The internal variables can be classified into the following categories:

- the dissipative variables,  $\alpha$ ,
- the non dissipative variables,  $\beta$ .

## B.2 METHOD OF TWO POTENTIALS

The constitutive laws are derived from two thermodynamic potentials:

- the Helmholtz free energy  $\mathcal{W}$  which is a function of the state variables only:

$$\mathcal{W} = \mathcal{W}(\epsilon, T, \alpha, \beta); \quad (\text{B.3})$$

The other potentials are obtained from the Helmholtz free energy by a partial Legendre-Fenchel transformation. For stability requirements, the potential must be a convex, lower semi-continuous function of its arguments [cf. Germain et al., 1983].

- a pseudo-potential of dissipation  $\Psi$ , which is function of the dissipative variables  $\alpha$  as parameters and of their fluxes  $\dot{\alpha}$ :

$$\Psi = \Psi(\alpha, \dot{\alpha}). \quad (\text{B.4})$$

The state laws are defined as follows (this choice is a consequence of the choice of normal state variables) [cf. Germain et al., 1983]:

$$\sigma = \rho \frac{\partial \mathcal{W}}{\partial \epsilon}, \quad \mathcal{A}_\alpha = -\rho \frac{\partial \mathcal{W}}{\partial \alpha}, \quad 0 = \rho \frac{\partial \mathcal{W}}{\partial \beta}, \quad (\text{B.5})$$

where  $\sigma$  is the stress (the macroscopic strain is assumed to be a non dissipative variable),  $\mathcal{A}_\alpha$  is the thermodynamic force associated with the variable  $\alpha$ , and where the thermodynamic force associated with the non-dissipative variable  $\beta$  is equal to zero.

The state law related to temperature is obtained from the Clausius-Duhem inequality. This inequality is derived from the first and second laws of thermodynamics and gives the expression of the dissipation  $\mathcal{D}$  (cf. Appendix A):

$$\mathcal{D} = \sigma : \dot{\epsilon} - \rho (\dot{\mathcal{W}} + s\dot{T}) - \frac{\mathbf{q} \cdot \nabla T}{T} \geq 0, \quad (\text{B.6})$$

where  $s$  is the specific entropy and  $\mathbf{q}$  is the heat influx vector. With (B.5), the following expression of the dissipation is obtained:

$$\mathcal{D} = \mathcal{A}_\alpha \dot{\alpha} - \rho \left( \frac{\partial \mathcal{W}}{\partial T} + s \right) \dot{T} - \frac{\mathbf{q} \cdot \nabla T}{T} \geq 0. \quad (\text{B.7})$$

The total dissipation  $\mathcal{D}$  is usually divided into two parts:

- the intrinsic dissipation  $\mathcal{D}_1$ ,

$$\mathcal{D}_1 = \mathcal{A}_\alpha \dot{\alpha} - \rho \left( \frac{\partial \mathcal{W}}{\partial T} + s \right) \dot{T}; \quad (\text{B.8})$$

- the thermal dissipation  $\mathcal{D}_2$ ,

$$\mathcal{D}_2 = -\frac{\mathbf{q} \cdot \nabla T}{T}. \quad (\text{B.9})$$

These two dissipations are assumed to be separately positive. The assumption of normal state variables together with the positivity of the intrinsic dissipation give:

$$\dot{\epsilon} = 0, \dot{\alpha} = 0, \forall \dot{T}, \mathcal{D}_1 \geq 0 \Rightarrow s = -\frac{\partial \mathcal{W}}{\partial T}. \quad (\text{B.10})$$

Finally,

$$\mathcal{D}_1 = \mathcal{A}_\alpha \dot{\alpha}. \quad (\text{B.11})$$

To obtain a complete determination of the thermodynamic state, complementary laws need to be defined, which link the fluxes of dissipative variables  $\dot{\alpha}$  to the thermodynamic forces  $\mathcal{A}_\alpha$ . The framework of Generalized Standard Materials, developed by Halphen and Nguyen, introduces a normal mechanism of dissipation: the thermodynamic forces associated with the dissipative variables  $\mathcal{A}_\alpha$  are sub-gradients of the pseudo-potential of dissipation:

$$\mathcal{A}_\alpha \in \partial \Psi(\dot{\alpha}). \quad (\text{B.12})$$

The pseudo-potential  $\Psi$  is required to have the following properties:

- non negative,
- convex with respect to the fluxes of dissipative variables  $\dot{\alpha}$ ,
- lower semi-continuous,
- equal to zero for  $\dot{\alpha} = 0$ .

This ensures the positivity of the intrinsic dissipation.

### B.3 CASE OF DEPENDENT STATE VARIABLES

This method of getting thermodynamically admissible constitutive laws has been extended to the case where internal constraints exist between state variables [cf. e.g. [Moumni and Nguyen, 1996](#); [Moumni et al., 2008](#)]. The state variables may be subject to two kinds of constraints:

- unilateral constraints:

$$h = \hat{h}(\epsilon, \alpha, \beta) \geq 0; \quad (\text{B.13})$$

- bilateral constraints:

$$g = \hat{g}(\epsilon, \alpha, \beta) = 0. \quad (\text{B.14})$$

Following [Moumni and Nguyen \[1996\]](#), it is assumed that all constraints are perfect and that all generalized reactions are associated with the potential:

$$\mathcal{W}_l = -\lambda g - \mu h, \text{ with } \mu h = 0 \text{ and } \mu \geq 0, \quad (\text{B.15})$$

where  $\lambda$  and  $\mu$  are Lagrange multipliers. The potential to be considered for the derivation of the state laws is the Lagrangian, sum of the Helmholtz free energy and of the potential associated to the constraints:

$$\mathcal{L} = \mathcal{W} + \mathcal{W}_l. \quad (\text{B.16})$$

[Moumni and Nguyen \[1996\]](#) showed that generalized reactions never work in the actual evolution. Consequently, as first introduced in [[Moumni, 1995](#)] and shown in [[Zaki, 2006](#)], it is not necessary to consider the constraints in the expression of the thermodynamic forces if these variables are scalar and if the constraints are differentiable.

## BIBLIOGRAPHY

- R. Abeyaratne and S.J. Kim. Cyclic effects in shape-memory alloys: a one-dimensional continuum model. *International Journal of Solids and Structures*, 34:3273–3289, 1997.
- R. Abeyaratne, S.J. Kim, and J. Knowles. A one-dimensional continuum model for shape-memory alloys. *International Journal of Solids and Structures*, 31:2229–2249, 1994.
- M. Achenbach and I. Müller. A model for shape memory. *Journal De Physique*, 43(NC-4):163–167, 1982.
- S. Akel and Q.S. Nguyen. Determination of the limit response in cyclic plasticity. In E. Hinton D.R.J. Owen and Editors E. Onate, editors, *Proceedings 2nd International Conference on Computational Plasticity: Models, Software and Applications*, page 639–650. Pineridge Press, Swansea, 1989.
- S. Amiable, S. Chapuliot, A. Constantinescu, and A. Fissolo. A comparison of lifetime prediction methods for a thermal fatigue experiment. *International Journal of Fatigue*, 28(7):692–706, 2006. doi: 10.1016/j.ijfatigue.2005.09.002.
- L. Anand and M. E. Gurtin. Thermal effects in the superelasticity of crystalline shape-memory materials. *Journal of the Mechanics and Physics of Solids*, 51(6):1015–1058, 2003. doi: 10.1016/S0022-5096(03)00017-6.
- F. Auricchio and L. Petrini. Improvements and algorithmical considerations on a recent three-dimensional model describing stress-induced solid phase transformations. *International Journal For Numerical Methods In Engineering*, 55(11):1255–1284, 2002. doi: 10.1002/nme.619.
- F. Auricchio and E. Sacco. Thermo-mechanical modelling of a superelastic shape-memory wire under cyclic stretching-bending loadings. *International Journal of Solids and Structures*, 38(34-35): 6123–6145, 2001.
- F. Auricchio, A. Reali, and U. Stefanelli. A macroscopic 1D model for shape memory alloys including asymmetric behaviors and transformation-dependent elastic properties. *Computer Methods In Applied Mechanics and Engineering*, 198(17-20):1631–1637, 2009. doi: 10.1016/j.cma.2009.01.019.
- J.M. Ball and R.D. James. Fine phase mixtures as minimizers of energy. *Archive for Rational Mechanics and Analysis*, 100:13–52, 1987.
- A. Bekker and L. Brinson. Temperature-induced phase transformation in a shape memory alloy: phase diagram based kinetics approach. *Journal of the Mechanics and Physics of Solids*, 45(6): 949–988, 1997.
- A. Bekker and L. Brinson. Phase diagram based description of the hysteresis behavior of shape memory alloys. *Acta Materialia*, 46:3649–3665, 1998.
- Z. Bo and D. Lagoudas. Thermomechanical modeling of polycrystalline SMAs under cyclic loading, Part I: theoretical derivations. *International Journal of Engineering Science*, 37:1089–1140, 1999a.

- Z. Bo and D. Lagoudas. Thermomechanical modeling of polycrystalline SMAs under cyclic loading, Part III: evolution of plastic strains and two-way shape memory effect. *International Journal of Engineering Science*, 37:1175–1203, 1999b.
- P. Boisse, P. Bussy, and P. Ladeveze. A new approach in nonlinear mechanics - the large time increment method. *International Journal For Numerical Methods In Engineering*, 29(3):647–663, 1990.
- Marc Bonnet and Attilio Frangi. *Analyse des solides déformables par la méthode des éléments finis*. -, 2006.
- J. Bowles and J. Mackenzie. The crystallography of martensitic transformations. *Acta Metallurgica*, 2:129–147, 1954.
- L. C. Brinson and M. S. Huang. Simplifications and comparisons of shape memory alloy constitutive models. *Journal of Intelligent Material Systems and Structures*, 7(1):108–114, 1996.
- L.C. Brinson. One-dimensional constitutive behavior of shape memory alloys: Thermomechanical derivation with non-constant material functions and redefined martensite internal variable. *Journal of Intelligent Material Systems and Structures*, 4:229–242, April 1993. doi: doi:10.1177/1045389X9300400213.
- M. Brocca, L. C. Brinson, and Z. Bazant. Three-dimensional constitutive model for shape memory alloys based on microplane model. *Journal of the Mechanics and Physics of Solids*, 50(5):1051–1077, 2002.
- T. E. Buchheit and J. A. Wert. Predicting the orientation-dependent stress-induced transformation and detwinning response of shape memory alloy single crystals. *Metallurgical and Materials Transactions A-physical Metallurgy and Materials Science*, 27(2):269–279, 1996.
- T. E. Buchheit, S. L. Kumpf, and J. A. Wert. Modeling the stress-induced transformation behavior of shape-memory alloy single-crystals. *Acta Metallurgica Et Materialia*, 43(11):4189–4199, 1995.
- S. Commend, A. Truty, and T. Zimmermann. Stabilized finite elements applied to elastoplasticity: I. mixed displacement-pressure formulation. *Computer Methods In Applied Mechanics and Engineering*, 193(33-35):3559–3586, 2004. doi: 10.1016/j.cma.2004.01.007.
- A. Constantinescu, E. Charkaluk, G. Lederer, and L. Verger. A computational approach to thermomechanical fatigue. *International Journal of Fatigue*, 26(8):805–818, 2004. doi: 10.1016/j.ijfatigue.2004.01.006.
- Pierre Duhem. *Traité d'énergétique ou de thermodynamique générale*. Collection: Les Grands classiques Gauthier-Villars, 1997.
- G. Eggeler, E. Hornbogen, A. Yawny, A. Heckmann, and M. Wagner. Structural and functional fatigue of NiTi shape memory alloys. *Materials Science and Engineering A*, 378(1-2):24 – 33, 2004. ISSN 0921-5093. doi: DOI:10.1016/j.msea.2003.10.327. European Symposium on Martensitic Transformation and Shape-Memory.
- D. Entemeyer, E. Patoor, E. Eberhardt, and M. Berveiller. Strain rate sensitivity in superelasticity. *International Journal of Plasticity*, 17(2):273–274, 2001.
- F. Falk. Model free energy, mechanics, and thermodynamics of shape memory alloys. *Acta Metallurgica*, 28(12):1773 – 1780, 1980. ISSN 0001-6160. doi: DOI:10.1016/0001-6160(80)90030-9.

- X.Q. Feng and Q.P. Sun. Shakedown analysis of shape memory alloy structures. *International Journal of Plasticity*, 23(2):183 – 206, 2007. ISSN 0749-6419. doi: DOI:10.1016/j.ijplas.2006.04.001.
- A.M. Figueiredo, P. Modenesi, and V. Buono. Low-cycle fatigue life of superelastic NiTi wires. *International Journal of Fatigue*, 31(4):751 – 758, 2009. ISSN 0142-1123. doi: DOI:10.1016/j.ijfatigue.2008.03.014.
- F.D. Fischer and K. Tanaka. A micromechanical model for the kinetics of martensitic transformation. *International Journal of Solids and Structures*, 29(14-15):1723 – 1728, 1992. ISSN 0020-7683. doi: DOI:10.1016/0020-7683(92)90165-P.
- M. Frémond. *Non-smooth thermomechanics*. Springer, 2001.
- K. Gall and H. Sehitoglu. The role of texture in tension-compression asymmetry in polycrystalline NiTi. *International Journal of Plasticity*, 15(1):69–92, 1999.
- K. Gall, H. Sehitoglu, R. Anderson, I. Karaman, Y. I. Chumlyakov, and I. V. Kireeva. On the mechanical behavior of single crystal NiTi shape memory alloys and related polycrystalline phenomenon. *Materials Science and Engineering A-structural Materials Properties Microstructure and Processing*, 317(1-2):85–92, 2001.
- P. Germain, Q. S. Nguyen, and P. Suquet. Continuum thermodynamics. *Journal of Applied Mechanics*, 50(4b):1010–1020, 1983. doi: 10.1115/1.3167184.
- A. L. Gloanec, P. Cerracchio, B. Reynier, A. Van Herpen, and P. Riberty. Fatigue crack initiation and propagation of a TiNi shape memory alloy. *Scripta Materialia*, 62(10):786–789, 2010. doi: 10.1016/j.scriptamat.2010.02.001.
- C. Grabe and O. T. Bruhns. On the viscous and strain rate dependent behavior of polycrystalline NiTi. *International Journal of Solids and Structures*, 45(7-8):1876–1895, 2008. doi: 10.1016/j.ijsolstr.2007.10.029.
- B. Halphen and Q. S. Nguyen. Sur les matériaux standards généralisés. *Journal de Mécanique*, 14: 39–63, 1975.
- Y J He and Q P Sun. Frequency-dependent temperature evolution in NiTi shape memory alloy under cyclic loading. *Smart Materials and Structures*, 19(11):115014, 2010.
- Y. J. He, H. Yin, R. H. Zhou, and Q. P. Sun. Ambient effect on damping peak of NiTi shape memory alloy. *Materials Letters*, 64(13):1483–1486, 2010. doi: 10.1016/j.matlet.2010.03.068.
- L. Heller, P. Sittner, J. Pilch, and M. Landa. Factors controlling superelastic damping capacity of SMAs. *Journal of Materials Engineering and Performance*, 18(5-6):603–611, 2009. doi: 10.1007/s11665-009-9358-1.
- T. J. R. Hughes. Multiscale phenomena - greens-functions, the dirichlet-to-neumann formulation, subgrid scale models, bubbles and the origins of stabilized methods. *Computer Methods In Applied Mechanics and Engineering*, 127(1-4):387–401, 1995.
- Y. Ivshin and T. Pence. A thermomechanical model for a one variant shape memory material. *Journal of Intelligent Material Systems and Structures*, 5:455–473, 1994.
- M. Kadkhodaei, R. K. N. D. Rajapakse, M. Mahzoon, and M. Salimi. Modeling of the cyclic thermomechanical of response of SMA wires at different strain rates. *Smart Materials and Structures*, 16(6):2091–2101, 2007. doi: 10.1088/0964-1726/16/6/012.

- W.T. Koiter. *Progress in Solid Mechanics*, chapter General problems for elastic-plastic solids, pages 165–221. North Holland, Amsterdam, 1960.
- D. Lagoudas and Z. Bo. Thermomechanical modeling of polycrystalline SMAs under cyclic loading, part ii: material characterization and experimental results for a stable transformation cycle. *International Journal of Engineering Science*, 37:1141–1173, 1999a.
- D. Lagoudas and Z. Bo. Thermomechanical modeling of polycrystalline SMAs under cyclic loading, part iv: modeling of minor hysteresis loops. *International Journal of Engineering Science*, 37:1205–1249, 1999b.
- D. Lagoudas and P. Entchev. Modeling of transformation-induced plasticity and its effects on the behavior of porous shape memory alloys. part I: constitutive model for fully dense SMAs. *Mechanics of Materials*, 36:865–892, 2004.
- P. H. Leo, T. W. Shield, and O. P. Bruno. Transient heat-transfer effects on the pseudoelastic behavior of shape-memory wires. *Acta Metallurgica Et Materialia*, 41(8):2477–2485, 1993.
- C. LExcellent and P. Blanc. Phase transformation yield surface determination for some shape memory alloys. *Acta Materialia*, 52(8):2317–2324, 2004. doi: 10.1016/j.actamat.2004.01.022.
- C. LExcellent and G. Bourbon. Thermodynamical model of cyclic behaviour of Ti–Ni and Cu–Zn–Al shape memory alloys under isothermal undulated tensile tests. *Mechanics of Materials*, 24:59–73, 1996.
- Z. Li and Q. Sun. The initiation and growth of macroscopic martensite band in nanograined NiTi microtube under tension. *International Journal of Plasticity*, 18:1481–1498, 2002.
- C. Liang and C. Rogers. One-dimensional thermomechanical constitutive relations for shape memory materials. *Journal of Intelligent Material Systems and Structures*, 1:207–234, 1990.
- T. J. Lim and D. L. McDowell. Cyclic thermomechanical behavior of a polycrystalline pseudoelastic shape memory alloy. *Journal of the Mechanics and Physics of Solids*, 50(3):651–676, 2002.
- Y. Liu, Z. Xie, J. Van Humbeeck, and L. Delaey. Asymmetry of stress-strain curves under tension and compression for NiTi shape memory alloys. *Acta Materialia*, 46(12):4325–4338, 1998.
- J.H. Mabe, F.T. Calkins, and G.W. Butler. Boeing’s variable geometry chevron, morphing aerostructure for jet noise reduction. In *47th AIAA/ASME/ASCE/AHS/ASC Structures, Structural Dynamics, and Materials Conference*, 2006.
- M. H. Maitournam, B. Pommier, and J. J. Thomas. Determination of the asymptotic response of a structure under cyclic thermomechanical loading. *Comptes Rendus Mecanique*, 330(10):703–708, 2002.
- A. Masud and K. M. Xia. A variational multiscale method for inelasticity: Application to superelasticity in shape memory alloys. *Computer Methods In Applied Mechanics and Engineering*, 195(33-36):4512–4531, 2006. doi: 10.1016/j.cma.2005.09.014.
- R. Matsui, H. Tobushi, Y. Furuichi, and H. Horikawa. Tensile deformation and rotating-bending fatigue properties of a highelastic thin wire, a superelastic thin wire, and a superelastic thin tube of NiTi alloys. *Journal of Engineering Materials and Technology*, 126(4):384–391, 2004. doi: 10.1115/1.1789952.
- P. G. McCormick, Y. Liu, and S. Miyazaki. Intrinsic thermal-mechanical behavior associated with the stress-induced martensitic-transformation in NiTi. *Materials Science and Engineering A-structural Materials Properties Microstructure and Processing*, 167(1-2):51–56, 1993.

- E. Melan. Theorie statisch unbestimmter systeme aus ideal-plastischen baustoff. *Sitzungsberichte Akademie der Wissenschaften, Wien*, 1:145–195, 1936.
- K. N. Melton and O. Mercier. Fatigue of niti thermoelastic martensites. *Acta Metallurgica*, 27(1): 137–144, 1979.
- S. Miyazaki, T. Imai, Y. Igo, and K. Otsuka. Effect of cyclic deformation on the pseudoelasticity characteristics of Ti-Ni alloys. *Metallurgical Transactions A-physical Metallurgy and Materials Science*, 17(1):115–120, 1986.
- S. Miyazaki, K. Mizukoshi, T. Ueki, T. Sakuma, and Yinong Liu. Fatigue life of Ti-50 at.memory alloy wires. *Materials Science and Engineering A*, 273-275:658 – 663, 1999. ISSN 0921-5093. doi: DOI:10.1016/S0921-5093(99)00344-5.
- Z. Moumni. *Sur la modélisation du changement de phase à l'état solide*. PhD thesis, Ecole Nationale des Ponts et Chaussées, 1995.
- Z. Moumni and Q. Nguyen. A Model of Material with Phase Change and Applications. *Journal de Physique IV*, 06(C1):C1-335–C1-345, 1996. doi: 10.1051/jp4:1996132.
- Z. Moumni, A. Van Herpen, and P. Riberty. Fatigue analysis of shape memory alloys: energy approach. *Smart Materials & Structures*, 14(5):S287–S292, 2005. doi: 10.1088/0964-1726/14/5/017.
- Z. Moumni, W. Zaki, and Q. S. Nguyen. Theoretical and numerical modeling of solid-solid phase change: Application to the description of the thermomechanical behavior of shape memory alloys. *International Journal of Plasticity*, 24(4):614–645, 2008. doi: 10.1016/j.ijplas.2007.07.007.
- Z. Moumni, W. Zaki, and H. Maitournam. Cyclic behavior and energy approach to the fatigue of shape memory alloys. *Journal of Mechanics of Materials and Structures*, 4(2):395–411, 2009.
- K. Mukherjee, S. Sircar, and N. B. Dahotre. Thermal effects associated with stress-induced martensitic-transformation in a Ti-Ni alloy. *Materials Science and Engineering*, 74(1):75–84, 1985.
- I. Muller and S. Seelecke. Thermodynamic aspects of shape memory alloys. *Mathematical and Computer Modelling*, 34:1307–1355, 2001.
- N. Nayan, D. Roy, V. Buravalla, and U. Ramamurty. Unnotched fatigue behavior of an austenitic NiTi shape memory alloy. *Materials Science and Engineering A-structural Materials Properties Microstructure and Processing*, 497(1-2):333–340, 2008. doi: 10.1016/j.msea.2008.07.025.
- Q.S. Nguyen. On shakedown analysis in hardening plasticity. *Journal of the Mechanics and Physics of Solids*, 51(1):101 – 125, 2003. ISSN 0022-5096. doi: DOI:10.1016/S0022-5096(02)00058-3.
- N. Ono and H. Shimanuki. Shear deformation by the stress-induced martensitic-transformation in shape memory alloys under the polycrystalline constraint. *Scripta Metallurgica Et Materialia*, 24(12):2269–2272, 1990.
- L. Orgeas and D. Favier. Stress-induced martensitic transformation of a NiTi alloy in isothermal shear, tension and compression. *Acta Materialia*, 46(15):5579–5591, 1998.
- J. Ortin and A. Planes. Thermodynamics of thermoelastic martensitic transformations. *Acta Metallurgica*, 37(5):1433–1441, 1989.
- K. Otsuka and C.M. Wayman. *Shape Memory Materials*. Cambridge University Press, 1999.

- A. Paiva, M. A. Savi, A. M. B. Braga, and P. M. C. L. Pacheco. A constitutive model for shape memory alloys considering tensile-compressive asymmetry and plasticity. *International Journal of Solids and Structures*, 42(11-12):3439–3457, 2005. doi: 10.1016/j.ijsolstr.2004.11.006.
- A. Paradis, P. Terriault, V. Brailovski, and V. Torra. On the partial recovery of residual strain accumulated during an interrupted cyclic loading of NiTi shape memory alloys. *Smart Materials & Structures*, 17(6):065027, 2008. doi: 10.1088/0964-1726/17/6/065027.
- E. Patoor, A. Eberhardt, and M. Berveiller. Thermomechanical behavior of shape memory alloys. *Archives of Mechanics*, 40:775–794, 1988.
- E. Patoor, M. Elamrani, A. Eberhardt, and M. Berveiller. Determination of the origin for the dissymmetry observed between tensile and compression tests on shape-memory alloys. *Journal De Physique Iv*, 5(C2):495–500, 1995.
- E. Patoor, D.C. Lagoudas, P.B. Entchev, C. Brinson, and X. Gao. Shape memory alloys, part I: General properties and modeling of single crystals. *Mechanics of Materials*, 38(5-6):391 – 429, 2006. ISSN 0167-6636. doi: DOI:10.1016/j.mechmat.2005.05.027. Shape Memory Alloys.
- M. Peigney. Shakedown theorems and asymptotic behaviour of solids in non-smooth mechanics. *European Journal of Mechanics - A/Solids*, 29(5):784 – 793, 2010. ISSN 0997-7538. doi: DOI: 10.1016/j.euromechsol.2010.03.011.
- M. Peigney and C. Stolz. An optimal control approach to the analysis of inelastic structures under cyclic loading. *Journal of the Mechanics and Physics of Solids*, 51(4):575–605, 2003.
- J. Perkins. Residual-stresses and origin of reversible (2-way) shape memory effects. *Scripta Metallurgica*, 8(12):1469–1475, 1974.
- R. Peyroux, A. Chrysochoos, C. Licht, and M. Lobel. Thermomechanical couplings and pseudoelasticty of shape memory alloys. *International Journal of Engineering Science*, 36(4):489–509, 1998.
- D.C. Pham. On shakedown theory for elastic-plastic materials and extensions. *Journal of the Mechanics and Physics of Solids*, 56(5):1905 – 1915, 2008. ISSN 0022-5096. doi: DOI:10.1016/j.jmps.2007.11.005.
- M. C. Piedboeuf, R. Gauvin, and M. Thomas. Damping behaviour of shape memory alloys: Strain amplitude, frequency and temperature effects. *Journal of Sound and Vibration*, 214(5): 885–901, 1998.
- W. Predki, M. Klönne, and A. Knopik. Cyclic torsional loading of pseudoelastic NiTi shape memory alloys: Damping and fatigue failure. *Materials Science and Engineering: A*, 417(1-2):182 – 189, 2006. ISSN 0921-5093. doi: DOI:10.1016/j.msea.2005.10.037.
- M. A. Qidwai and D. C. Lagoudas. On thermomechanics and transformation surfaces of polycrystalline NiTi shape memory alloy material. *International Journal of Plasticity*, 16(10-11):1309–1343, 2000.
- B. Raniecki and C. Lexcellent. Thermodynamics of isotropic pseudoelasticty in shape memory alloys. *European Journal of Mechanics A-solids*, 17:185–205, 1998.
- B. Raniecki and Z. Mroz. Yield or martensitic phase transformation conditions and dissipation functions for isotropic, pressure-insensitive alloys exhibiting SD effect. *Acta Mechanica*, 195 (1-4):81–102, 2008. doi: 10.1007/s00707-007-0544-7.

- T. Sawaguchi, G. Kaustrater, A. Yawny, M. Wagner, and G. Eggeler. Crack initiation and propagation in 50.9 at. pct NiTi pseudoelastic shape-memory wires in bending-rotation fatigue. *Metallurgical and Materials Transactions A-physical Metallurgy and Materials Science*, 34A(12):2847–2860, 2003.
- J. A. Shaw and S. Kyriakides. Thermomechanical aspects of NiTi. *Journal of the Mechanics and Physics of Solids*, 43(8):1243–1281, 1995.
- N. Siredey, A. Hautcoeur, and A. Eberhardt. Lifetime of superelastic Cu-Al-Be single crystal wires under bending fatigue. *Materials Science and Engineering A*, 396(1-2):296 – 301, 2005. ISSN 0921-5093. doi: DOI:10.1016/j.msea.2005.01.021.
- P. Sittner and V. Novak. Anisotropy of martensitic transformations in modeling of shape memory alloy polycrystals. *International Journal of Plasticity*, 16(10-11):1243–1268, 2000.
- R. P. Skelton, T. Vilhelmsen, and G. A. Webster. Energy criteria and cumulative damage during fatigue crack growth. *International Journal of Fatigue*, 20(9):641 – 649, 1998. ISSN 0142-1123. doi: DOI:10.1016/S0142-1123(98)00027-9.
- Q.P. Sun and K.C. Hwang. Micromechanics modelling for the constitutive behavior of polycrystalline shape memory alloys–I. derivation of general relations. *Journal of the Mechanics and Physics of Solids*, 41(1):1 – 17, 1993. ISSN 0022-5096. doi: DOI:10.1016/0022-5096(93)90060-S.
- P. Suquet. *Rupture et Plasticité*. Cours de l'Ecole Polytechnique, 2008.
- K. Tanaka. A thermomechanical sketch of shape memory effect: one-dimensional tensile behavior. *Res Mechanica*, 18:251–263, 1986.
- K. Tanaka, S. Kobayashi, and Y. Sato. Thermomechanics of transformation pseudoelasticity and shape memory effect in alloys. *International Journal of Plasticity*, 2(1):59–72, 1986.
- K. Tanaka, F. Nishimura, T. Hayashi, and C. Tobushi, H.and L. excellent. Phenomenological analysis on subloops and cyclic behavior in shape memory alloys under mechanical and/or thermal loads. *Mechanics of Materials*, 19:281–292, 1995.
- H. Tobushi, T. Hachisuka, S. Yamada, and P. H. Lin. Rotating-bending fatigue of a TiNi shape-memory alloy wire. *Mechanics of Materials*, 26(1):35–42, 1997.
- J. Van Humbeeck. Cycling effects, fatigue and degradation of shape memory alloys. *Journal De Physique Iv*, 1(C4):189–197, 1991.
- J. Van Humbeeck and L. Delaey. The influence of strain-rate, amplitude and temperature on the hysteresis of a pseudoelastic Cu-Zn-Al single-crystal. *Journal De Physique*, 42(NC5):1007–1011, 1981.
- A. Vitiello, G. Giorleo, and R. E. Morace. Analysis of thermomechanical behaviour of nitinol wires with high strain rates. *Smart Materials & Structures*, 14(1):215–221, 2005. doi: 10.1088/0964-1726/14/1/021.
- M. Wagner, T. Sawaguchi, G. Kausträter, D. Höffken, and G. Eggeler. Structural fatigue of pseudoelastic NiTi shape memory wires. *Materials Science and Engineering A*, 378(1-2):105 – 109, 2004. ISSN 0921-5093. doi: DOI:10.1016/j.msea.2003.11.058. European Symposium on Martensitic Transformation and Shape-Memory.
- R.J. Wasilewski. Effects of applied stress on martensitic transformation in TiNi. *Metallurgical Transactions*, 2(11):2973–2981, 1971.

- C. M. Wayman. The phenomenological theory of martensite crystallography - interrelationships. *Metallurgical and Materials Transactions A-physical Metallurgy and Materials Science*, 25(9):1787–1795, 1994.
- M. Wechsler, D. Lieberman, and T. Read. On the theory of the formation of martensite. *Transactions of AIME*, 197:1503–1515, 1953.
- X.C. Wu, D.S. Grummon, and T.J. Pence. Modeling phase fraction shakedown during thermomechanical cycling of shape memory materials. *Materials Science and Engineering A*, 273-275:245 – 250, 1999. ISSN 0921-5093. doi: DOI:10.1016/S0921-5093(99)00380-9.
- W. Zaki. *Comportement thermo-mécanique des matériaux à mémoire de forme: modélisation macroscopique, chargement cyclique et fatigue*. PhD thesis, Ecole Polytechnique, 2006.
- W. Zaki. An approach to modeling tensile-compressive asymmetry for martensitic shape memory alloys. *Smart Materials & Structures*, 19(2):025009, 2010. doi: 10.1088/0964-1726/19/2/025009.
- W. Zaki and Z. Moumni. A three-dimensional model of the thermomechanical behavior of shape memory alloys. *Journal of the Mechanics and Physics of Solids*, 55:2455–2490, 2007a. doi: 10.1016/j.jmps.2007.03.012.
- W. Zaki and Z. Moumni. A 3D model of the cyclic thermomechanical behavior of shape memory alloys. *Journal of the Mechanics and Physics of Solids*, 55:2427–2454, 2007b. doi: 10.1016/j.jmps.2007.03.011.
- W. Zaki, S. Zamfir, and Z. Moumni. An extension of the ZM model for shape memory alloys accounting for plastic deformation. *Mechanics of Materials*, 42(3):266–274, 2010. doi: 10.1016/j.mechmat.2009.11.013.
- J. Zarka, J. Frelat, G. Inglebert, and P. Kasmai-Navidi. *A new approach to inelastic analyses of structures*. M. Nijhoff, Dordrecht, PAYS-BAS, 1998.
- S. Y. Zhu and Y. F. Zhang. A thermomechanical constitutive model for superelastic SMA wire with strain-rate dependence. *Smart Materials & Structures*, 16:1696–1707, 2007. doi: 10.1088/0964-1726/16/5/023.